UNIVERSIDAD DE CHILE
FACULTAD DE CIENCIAS FÍSICAS Y MATEMÁTICAS
DEPARTAMENTO DE FÍSICA
DEPARTAMENTO DE INGENIERÍA MATÉMATICA

VORTICES INDUCED BY TOPOLOGICAL FORCING IN NEMATIC LIQUID CRYSTAL LAYERS

TESIS PARA OPTAR AL GRADO DE MAGÍSTER EN CIENCIAS, MENCIÓN FÍSICA
MEMORIA PARA OPTAR AL TÍTULO DE INGENIERO CIVIL MATEMÁTICO

ENRIQUE AUGUSTO CALISTO LEIVA

PROFESOR GUÍA:
MARCEL CLERC GÁVILAN

PROFESOR CO-GUÍA:
MICHAŁKOWALCZYK

MIEMBROS DE LA COMISIÓN:
LUIS FOÀ TORRES
CLAUDIO MUÑOZ CERÓN
SERGIO RICA MERY

Este trabajo ha sido parcialmente financiado por CONICYT-PFCHA/Magister Nacional/2017-22171924

SANTIAGO DE CHILE
2019

RESUMEN DE LA MEMORIA PARA OPTAR
AL TÍTULO DE INGENIERO CIVIL MATEMÁTICO
TESIS PARA OPTAR
AL GRADO DE MAGÍSTER EN CIENCIAS, MENCIÓN FÍSICA
POR: ENRIQUE AUGUSTO CALISTO LEIVA
FECHA: 2019
PROF. GUÍA: MARCEL CLERC GÁVILAN

VORTICES INDUCED BY TOPOLOGICAL FORCING IN NEMATIC LIQUID CRYSTAL LAYERS

In two-dimensional systems, dissipative vortices are described by a complex Ginzburg-Landau equation (CGLE) which has a universal character and describes such different systems as fluids, superfluids, superconductors, liquid crystals, granular media, magnetic media, and optical dielectrics, to mention just a few. Vortices occur in complex fields and can be identified as topological defects, that is, pointlike singularities which locally breaks the symmetry.

Liquid crystals with negative anisotropic dielectric constant and homeotropic anchoring are a natural physical context where dissipative vortices are observed. Dissipative vortices are known in this context as *umbilical defects*. Recently, by exploiting reorientational nonlinearities in nematic liquid-crystal layers of an optically addressable liquid-crystal cell, it has been shown that spontaneous and stable matter vortices can be induced.

This thesis is composed of seven chapters and one appendix that contain the article published during this work. The first three chapters serve as an introduction: In Chapter 1 we present motivations and preliminary notions about topological defects, while Chapter 2 and 3 are focused on presenting general results about Ginzburg-Landau type equations.

Chapter 4 is devoted to establishing analytically the origin of vortex lattices observed in illuminated liquid crystal layers, we give a theoretical description in terms of an approximate vortex solution that we called *Rayleigh vortex* valid under the Fréederickzs transition and induced by a topological forcing.

In Chapter 5 we study a new type of topological forcing that induces vortex-like defects inspired by experimental observations with inhomogeneous magnetic fields in a nematic liquid-crystal light valve (LCLV). We give a theoretical description in terms of a Ginzburg-Landau type amplitude equation and also we derive an analytical solution which describes accurately the system behavior and shows fair agreement with numerical simulations and experimental observations.

In Chapter 6 we study the dynamics of defects in one (kinks) and two dimensional (vortices) cases, deriving in each one the dynamical motion equation for the defect position under topological forcing.

Finally, in Chapter 7 we show qualitative properties of global minimizers of the Ginzburg-Landau energy, prove the existence of global minimizers and state the main results about symmetry breaking scenarios.

RESUMEN DE LA MEMORIA PARA OPTAR
AL TÍTULO DE INGENIERO CIVIL MATEMÁTICO
TESIS PARA OPTAR
AL GRADO DE MAGÍSTER EN CIENCIAS, MENCIÓN FÍSICA
POR: ENRIQUE AUGUSTO CALISTO LEIVA
FECHA: 2019
PROF. GUÍA: MARCEL CLERC GÁVILAN

VORTICES INDUCED BY TOPOLOGICAL FORCING IN NEMATIC LIQUID CRYSTAL LAYERS

En sistemas bidimensionales, vórtices disipativos son descritos por medio de la ecuación de Ginzburg-Landau a coeficientes complejos (CGLE) la cuál tiene caracter universal y describe diferentes sistemas físicos tales como fluidos, superfluidos, superconductores, cristales líquidos, medios granulares, medios magnéticos y dieléctricos ópticos, por mencionar algunos. Los vórtices aparecen en campos complejos y pueden identificarse como defectos topológicos, esto es, singularidades puntuales que rompen localmente la simetría.

Crístales líquidos con constante de anisotropía dieléctrica negativa y anclaje homeotropico son un contexto físico natural donde vórtices disipativos son observados. En este contexto, se los denomina *defectos umbilicos.* Recientemente, aprovechando no linealidades orientacionales en capas de cristal líquido nemático de una celda óptica, se ha mostrado la indución de vórtices estables.

Esta tesis esta compuesta de 7 capítulos y 1 apéndice que contiene el artículo publicado durante este trabajo. Los primeros 3 capítulos sirven como una introducción: En el capítulo 1 presentamos motivaciones y nociones preliminares sobre defectos topológicos, mientras que los capítulos 2 y 3 estan enfocados en presentar resultados generales sobre ecuaciones tipo Ginzburg-Landau.

El capítulo 4 esta dedicado a establecer analiticamente el origen de redes de vórtices observadas en celdas de cristal líquido, se da una descripción teórica en términos de una solución aproximada denominada *Vórtice de Rayleigh* válida bajo la transición de Fréederickzs e inducida por un forzamiento topológico.

En el capítulo 5 estudiamos un nuevo tipo de forzamiento topológico que induce defectos tipo vórtices, inspirados en observaciones experimentales con campos magnéticos inhomogeneos aplicados a un celdad de cristal líquido nemático. Se da una descripción teórica en términos de ecuaciones de amplitud y tambien se deriva una solución analítica que describe de manera precisa al sistema en concordancia con simulaciones numéricas.

En el capítulo 6, estudiamos la dinámica de defectos en 1 y 2 dimensiones, derivando en cada caso una ecuación de movimiento para la posición del defecto bajo forzamiento topológico.

Finalmente, en el capítulo 7 estudiamos propiedades cualitativas de los minimizadores globales de la energía de Ginzburg-Landau, se prueban resultados de existencia de minimizadores globales y se enuncian los principales resultados existentes sobre escenarios de rompimiento de simetría.

A mi madre.

Agradecimientos

Quisiera agradecer a todas aquellas personas que de un modo u otro han contribuido al desarrollo de esta tesis, a quienes han estado presentes en distintos momentos de mi carrera universitaria y que con sus interacciones dan forma a parte de quien soy.

Comenzare por agradecer desde el principio: A mi madre, por su infinita paciencia y sacrificio, y quien merece todo lo bueno que el mundo puede dar, ójala todos supieran lo genial que eres. A mi hermano, por su paciencia y sus consejos, por haberme escuchado aún cuando yo no siempre hiciera lo mismo. Agradezco a mi padre y a mi tia Ivonne su preocupación.

A los que desde el lejano colegio volvimos a coincidir en la U, Felipe y Ricardo

A quienes conocí durante mis primeros años de Plan Común, los chicos de la pandilla, muy especialmente, a Suafle, Aurora y Mireya.

A los que estuvieron conmigo en el Preuniversitario José Carrasco Tapia: Nico, Astor, Magaly y Camila.

A mis compañeros de generación en los largos años en el DIM: Valentina Toro, David Hsson, Alonso Guzman, Martin Rios, Paul Silva, Carlos Saji, Francisco Venegas y Leonel Huerta. Mención especial a Mauro Campos por las siempre interesantes conversaciones, a Diego Gramusset y Sebastian Tapia que siempre encontraron tiempo para ir a perderlo a mi oficina, a Piero Zanocco por su calidad humana y todas las veces que fuimos auxiliares de Proba, a Camilo Rojas por su confianza, amabilidad y por que derrotamos juntos a Complejidad, a Pedro Vergara por su amistad, simpatía y generosidad y a Cristobal Rojas (8) por los partidos de futbol, las pizzas y las buenos ratos. A quienes no eran de mi generación, pero compartimos igualmente: Bob, Benja, Mario, Cabezas, Emilio, Matus, Marchant, Zelada, Evelyn y Tamara. A aquellos con los que coincidí en el departamento de Física, Guille, Eva, Archi, Jenny, Daniel. A Fernanda Perez y Beatriz Zenteno por su amistad, sonrisas y buenos momentos.

A quienes no incluí en ninguna categoría: Nelly Pinto, Francisca Oporto, Matias Abarca, Esteban Sapunar, Rayen Cariman y Carolina Gutierrez.

A Karina Muñoz por tu amistad desde que nos conocimos el primer día de clases, agradezco tu sencillez, tu sonrisa que nunca ha dejado de alegrarme el dia y tu confianza.

A María José Chávez agradezco tu amistad, tu confianza, tu risa, las conversaciones sobre la vida, el cafe y el tiempo compartidos.

Quisiera agradecer tambien a los profesores Nelson Zamorano, Fernando Lema y Claudio Muñoz por su buena voluntad y disposición conmingo.

Finalmente, agradezco profundamente a mi profesor guía Marcel Clerc, por haber confiado en mí. Agradezco su calidad humana, su paciencia conmigo y cada uno de los consejos que me dio.

Agradezco tambien el financiamiento de Conicyt mediante su Beca de Magister Nacional.

Contents

List of Figures

Introduction

In two-dimensional systems, dissipative vortices are described by the complex Ginzburg-Landau equation (CGLE) which has a universal character and describes such different systems as fluids, superfluids superconductors, liquid crystals, granular media, magnetic media, and optical dielectrics, to mention just a few [1]. Vortices occur in complex fields and can be identified as topological defects, that is, pointlike singularities which locally break the symmetry. They exhibit zero intensity at the singular point which is phase spiraling around it. The topological charge is assigned by counting the number of spiral arms in the phase distribution, while the sign is given by the sense of the spiral rotation.

Liquid crystals with negative anisotropic dielectric constant and homeotropic anchoring are a natural physical context where dissipative vortices are observed [2]. Dissipative vortices are known in this context as *umbilical defects* [2, 3]. Two types of stable vortices are observed. They have opposite charges and are characterized by being attracted to (repulsed from) the opposite (identical) topological charge. Recently, by exploiting reorientational nonlinearities in the nematic liquid-crystal layer of an optically addressable liquid-crystal cell, it has been shown that spontaneous, stable matter vortices can be induced.

Topological defects that had attracted a lot of attention in view of their technological applications are the so-called **Optical Vortices**, they are point phase dislocations; that is, they are singular points where the electromagnetic field goes to zero and around which the phase distribution forms an N-armed spiral, with N being the topological charge [1],[4]. In the last decade, optical vortices have attracted attention for the diverse photonic applications [5], ranging from the interchange of angular momentum between light and matter [6], optical tweezers [7], [8], quantum computation [9], enhancement of astronomical images [10], the generation of optical beams by micro/macro patterned in liquid crystals [11], and data transmission [12]. In these applications, optical vortices lattices are always involved and required, because they contain multiple optical vortices that supply information, flexibility, and manipulation [12]. Indeed, the generation, detection, and manipulation of optical vortices lattices are of fundamental relevance in the research described and in future optical applications. The realization of programable lattices of optical vortices with arbitrary distribution in space was demonstrated by exploiting reorientational nonlinearities in the nematic liquid crystal layer of light valve (LCLV) [13]. The vortex arrangements were determined qualitatively on the basis of consistent topological rules governing light-induced matter defects of both signs. When a LCLV is illuminated by a Gaussian beam, a vortex in the molecular orientation (umbilic defect) is induced [14], [15].

This dissertation is devoted to establishing analytically the origin of the vortex lattices observed in illuminated liquid crystal layers with photosensitive walls. Using a topologically driven Ginzburg-Landau equation that describes illuminated LCLV close to the Fréedericksz transition, the vortices and the lattices they form are described. The numerical simulations of the amplitude equation, analytical solutions, and experimental observations show good agreement.

Topological forcing induced vortices can be also achieved by means of an inhomogeneous magnetic field generated by a Neodymium magnet ring. Chapter 5 presents a method for robust vortex induction, which relies on nematic liquid crystal strong interaction with magnetic fields. Experimentally, permanent induction of a matter vortex triplet is observed and a static stable vortex is measured at the sample center.

In Chapter 6 we study the dynamics of defects in one (kinks) and two dimensional (vortices) cases, deriving in each one the dynamical motion equation for the defect position under topological forcing.

Finally, from a variational perspective vortex solutions correspond to minimizers of a Ginzburg-Landau energy. In Chapter 7 existence and qualitative properties of global minimizers of the Ginzburg-Landau energy are shown.

Chapter 1

Preliminar Concepts

1.1 Topological Defects

The study of topological defects arises within many of the branches of physics, from quantum field theory, cosmology, condensed matter physics, liquid crystals, among others [1]. The importance of these defects and their role in phase transitions in bidimensional systems was identified by Kosterliz and Thouless [16] and also by Berezinskii [17], and earned to the formers being awarded the 2016 Nobel Physics Prize [18].

The mathematical theory of topological defects find its foundations on the algebraic topology and the concept of homotopy groups [19], and connects abstract mathematical ideas with actual physical phenomena.

Topology concerns itself with the study of shapes and spaces (without a notion of distance) and how different shapes can be continuously deformed into one another. **Topological defects** are defects that break the order of otherwise ordered systems—for example, structural defects in crystalline solids or domain walls separating regions of different magnetic orientation in magnetic media, but what makes topological defects truly intriguing is that they are permanently stable in the sense that they can not be continuously deformed.

1.2 Topological Phase Transitions

In a classical sense, matter exists as either a solid, a liquid or a gas. A **phase transition** occurs when matter changes from one form into another, such as liquid water turning to ice. Quantum effects do not normally play any role in these phase transitions because they are ruled out by thermal fluctuations. However, at very low temperatures, matter takes on strange new phases and quantum effects become noticeable. For example, electrical resistance disappears at temperatures approaching absolute zero.

In 1972 Kosterlitz and Thouless identified a new type of phase transitions in 2D systems [16], where topological defects plays a crucial role. In parallel, this study was carried out in the Soviet orbit by V.L. Berezinksy [17]. As a result, they were able to show that superconductivity and superfluidity can occur in 2D layers at low temperatures.

The simplest model that exhibits the BKT (This acronym is in honor of Berezinsky, Kosterlitz and Thouless) transition is the XY model; i.e, a $2D$ lattice with unit $2D$ vectors at each site. Each vector $\vec{S}_{\mathrm{i}}$ is specified by a single angle θ_{i}

$$\vec{S}_{\mathrm{i}} = (\cos\theta_{\mathrm{i}}, \sin\theta_{\mathrm{i}}).$$

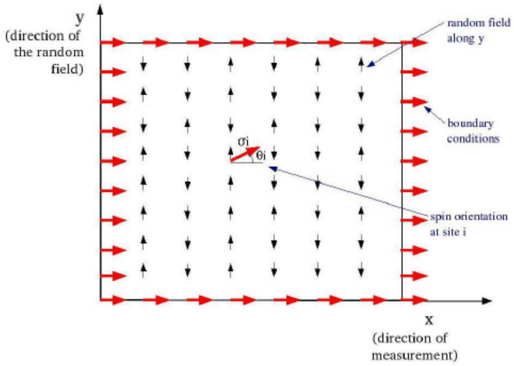

Figure 1.1: Schematic representation of the XY Model Lattice [20].

Considering nearest-neighbor interactions, we write the reduced Hamiltonian as

$$\mathcal{H} = -\frac{J}{k_B T}\sum_{<\mathrm{i},j>} \vec{S}_{\mathrm{i}} \cdot \vec{S}_j = -\frac{J}{k_B T}\sum_{<\mathrm{i},j>} \cos(\theta_{\mathrm{i}} - \theta_j),$$

where $J > 0$ is the interaction coupling constant and $k_B T$ accounts for the thermal energy. Now at low temperatures, as the fluctuations in the angles are going to be small, at long distances, we take the continuum limit of the lattice model assuming the angle field is slowly varying and we get

$$\mathcal{H} = -\frac{K}{2}\int \mathrm{d}^2 x |\nabla\theta|^2 \quad \text{and} \qquad K = \frac{1}{k_B T}.$$

On the other hand, the periodicity allows nontrivial topological configurations: for a periodic field, we can increase or decrease the field by integer multiples of the periodicity around the circuit and still come back to the same physical value of the field, in this case we can write the following constraint

$$\oint_{\Gamma} \nabla\theta \cdot \mathrm{d}l = 2\pi n.$$

For $n = \pm 1$, the configuration is called a **vortex**, they correspond to topological defects in the $\theta(x)$ field (which is not defined at the core of the defect). At the continuum level, the vortex is a singular solution of the Euler-Lagrange equation.

$$\nabla^2\theta = 0 \quad s.t. \quad \oint_{\Gamma} \nabla\theta \cdot \mathrm{d}l = 2\pi n.$$

And for a single defect, we have $|\nabla\theta| = \frac{n}{r}$ and is possible to estimate the energy of the single vortex configuration by

$$E_1 = J\pi \ln\left(\frac{L}{a}\right),$$

where a is the lattice spacing. In the thermodynamic limit($L \rightarrow \infty$) this energy diverges logarithmically, hence a lone vortex **cannot** exist. However, vortex pairs with opposite charges (dipoles) have a finite energy

$$E_2 = 2J\pi \ln\left(\frac{r}{a}\right),$$

where r is the finite vortex separation, hence pairs **can** be excited at finite temperature. There is a simple hand-waving argument for the existence of a phase transition: there are roughly $\left(\frac{L}{a}\right)^2$ ways to place a vortex of size $\sim a^2$ in an area of L^2. Then the configurational entropy is given by

$$S = 2k_B \ln\left(\frac{L}{a}\right),$$

and so the free energy

$$F = E_1 - TS = (\pi J - 2k_B T)\ln\left(\frac{L}{a}\right) \underbrace{\longrightarrow}_{\text{Thermodynamic Limit}} \begin{cases} +\infty & \text{low temperature} \\ -\infty & \text{conversely} \end{cases}$$

This indicates that at low temperatures energy effects will dominate and vortices will be suppressed (the system will behave like a dilute gas of vortex/antivortex pairs) while at higher temperatures the entropic contributions favor the proliferation of vortices. In other words, the pairs will unbind and the system will behave as a vortex plasma. Hence, we expect the BKT Transition to occur by the critical temperature $T_c = \frac{J\pi}{2k_B T}$.

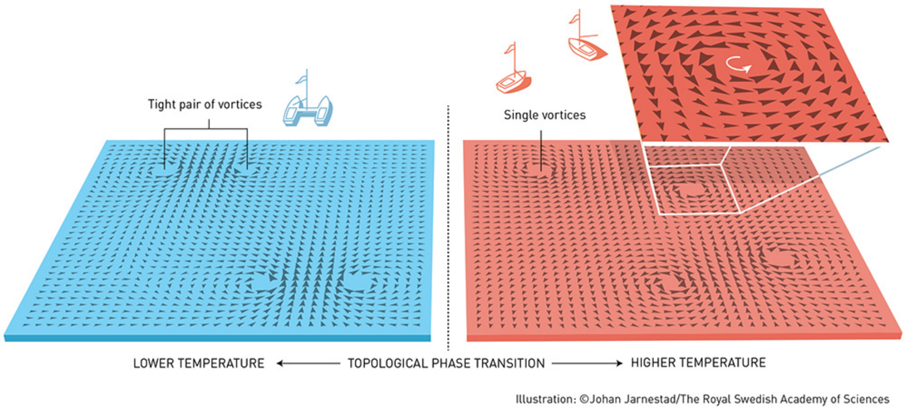

Illustration: ©Johan Jarnestad/The Royal Swedish Academy of Sciences

Figure 1.2: Schematic representation of the Kosterlitz Thouless Transition [18].

In contrast to usual continuous phase transitions, the BKT-transition does not break any symmetry, something that was completely new and unexpected, since initially, the phase transition were thought to be related to symmetry breaking phenomena (Landau Theory) [21].

The BKT topological model of a phase transition in two dimensions has been used to explain experiments with many different types of physical systems. Examples include very thin films of superfluid ^{4}He that form naturally on a solid substrate [22], disordered thin films of superconductors [23], granular films of superconductors [24].

1.3 Topological Theory of Defects

On a qualitative level, the formation of defects in phase transitions is described by the geometrical language of group theory [19]. In order to do that, we consider an *ordered medium* i.e. a region of space $M \subset \mathbb{R}^3$ described by a function $f : M \to X$ that assigs to each point of the region an *order parameter*. The space X it is known as the *order parameter space* or *manifold of internal states.*

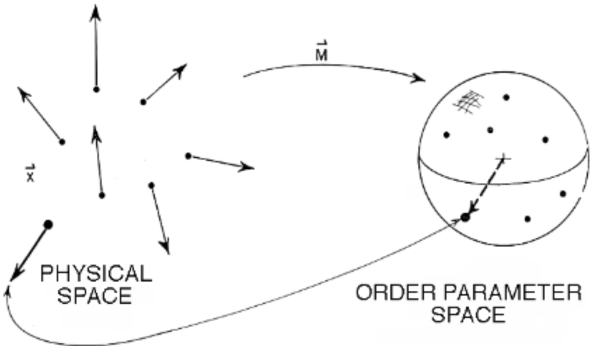

Figure 1.3: Order parameter space for 3D Magnetization [19].

Remark A medium is *uniform* if f is constant everywhere and it is *disordered* if $f = 0$, and *ordered* otherwise.

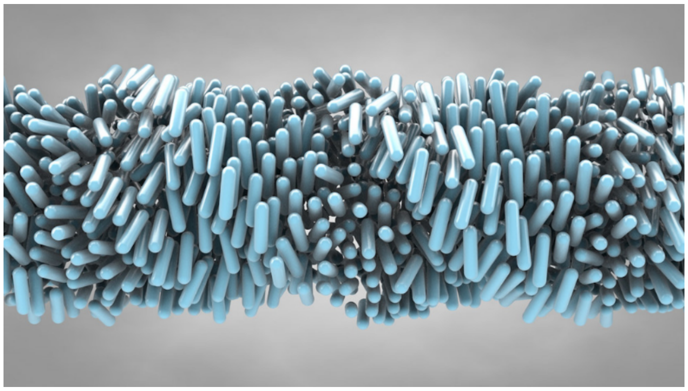

Figure 1.4: A Chiral Liquid Crystal is an example of ordered media

We shall be interested in nonuniform media in which the order parameter varies constinuously in space except, perhaps, at isolated points, lines or surfaces, these regions constitute the subset of *defects* $\mathcal{Z} \subset M$.

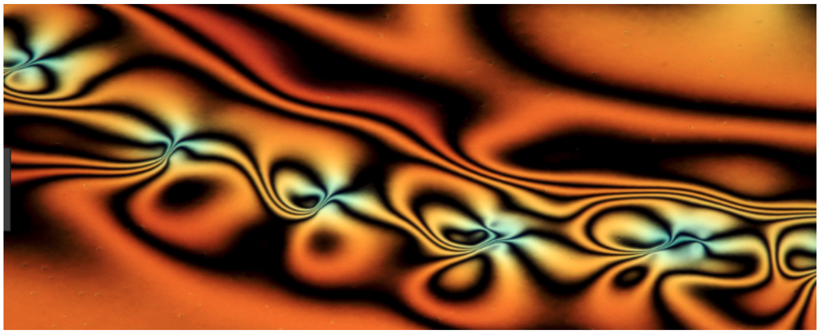

Figure 1.5: Snapshot of a liquid crystal cell, the interception of black lines shows umbilical defects, vortices

We now introduce, some topological notions which are necessary to understand and classify defects.

Definition 1.1 ***Path-connected***
A topological space X is said to be ***path-connected*** *or* ***pathwise connected*** *if there is exactly one path-component, i.e., if there is a path joining any two points in X*

Definition 1.2 ***Simple connected***
A topological space X is called ***simple connected*** *if it is path-connected and any loop in X can be contracted to a point, i.e, for any loop $f : S^1 \to X$ there exits a continuous map $F : D^2 \to X$ such that $F|_{S^1} = f$. Here, S^1 and D^2 denotes the unit circle and closed unit disk in the Euclidean plane respectively.*

Definition 1.3 ***Homotopy***
Let f_1 and f_2 be two curves in a simple connected space X with the same endpoints.
Then, f_1 and f_2 are ***homotopic*** *if there is a continuous deformation of f_1 into f_2, i.e. theres is a continuous function $H : X \times [0, 1] \to X$ such that, $H(x, 0) = f_1(x)$ and $H(x, 1) = f_2(x)$.*

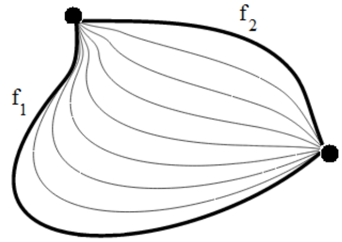

Figure 1.6: Illustration of a Homotopic curves

1. It can be shown that homotopy is an equivalence relation.
2. The **equivalence class** $[f]$ of a path f is defined as the set of all paths that are homotopic to f.
3. A path that is homotopic to a single point is called **nullhomotopic**

The *homotopy classes* in a path-connected space X have a group structure if we define the following operation:

1. Let $x_0 \in X$, let f, g be continuous paths that start and end at x_0.
2. We can form a new path by going along f first and then along g.
3. This new path is said to be the composition path fog.

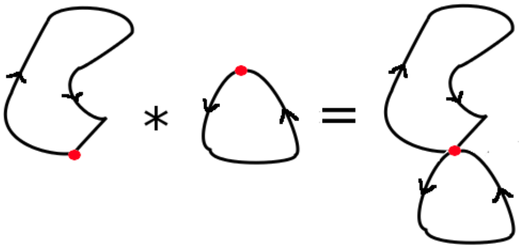

Figure 1.7: Composition path

Definition 1.4 ***Fundamental Group***
The set of all equivalence classes of paths that start and end at x_0 *is a group under the operation of path composition.*
This is called the ***fundamental group*** *of* X *at the point* x_0*, written as* $\pi_1(X, x_0)$

Remark In a space X path-connected the fundamental group does not depend on the choice of base point x_0

Topological spaces with different homotopy groups cannot be continuously deformed into one another and thus are not homeomorphic. As it can be seen in Figure 1.8, the fact that there is a hole in the M_2 manifold means that there are new classes of maps from the circle to the manifold.

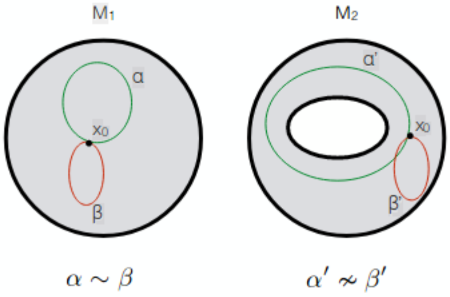

Figure 1.8: Non homeomorphic manifolds

On M_1, there is only one class of maps from S_1 and thus α is homotopic to β. However, on M_2, the hole defines infinite classes of maps from the circle. The fundamental group *detects* holes in a topological space by mapping loops to the space. If a space has no holes in it, then loops can always be contracted to points, and all maps are identical, i.e, the fundamental group on X is trivial $\pi_1(X) = \mathbb{I}$. However, if a space has a single hole in it there will be distinct maps from $S^1 \to X$.

Example 1. The fundamental group of the unit circle S^1 is the collection of paths with different **winding number**: $\pi_1(S^1) \cong \mathbb{Z}$

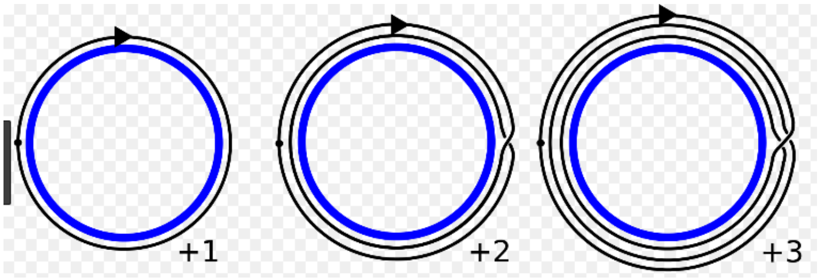

Figure 1.9: Fundamental group of S^1

2. On the unit sphere S^2, any loop can be smoothly deformed to a point. Thus, all loops on the sphere are nullhomotopic, and $\pi_1(S^2) \cong 0$.

Figure 1.10: Fundamental group of S^2

3. On the torus T^2 there are three types of loops, those that can be contracted and those that cannot be contracted because they wind around the donut hole or the donut tube. Thus, the first homotopy group of the torus is $\pi_1(T^2) = \mathbb{Z} \times \mathbb{Z} \times \mathbb{I} \cong \mathbb{Z}^2$

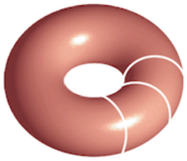

Figure 1.11: Fundamental group of T^2

It is possible to generalize the concept of the *fundamental group* to maps from higher dimensional spheres, instead of from S^1:

Definition 1.5 ***Homotopy Group***
The n-th ***homotopy group*** *of a topological space X is the set of homotopy classes of maps from the n-sphere to X, with a group structure, and is denoted $\pi_n(X)$. The fundamental group is $\pi_1(X)$, and the maps $S^n \to X$ must pass through a basepoint $x_0 \in X$.*

Remark For $n > 1$, the homotopy group $\pi_n(X)$ is an Abelian group, and the group operations are not as simple as those for the fundamental group.

When the n-th homotopy group is non-vanishing, their elements are identified as *topological defects* in codimension n. This formalism allow us a classification of topological defects as:

$$\begin{aligned}
\pi_0(X) &\neq 0 \rightarrow \text{walls} \\
\pi_1(X) &\neq 0 \rightarrow \text{vortices} \\
\pi_2(X) &\neq 0 \rightarrow \text{monopoles} \\
\pi_3(X) &\neq 0 \rightarrow \text{textures} \\
&\ldots
\end{aligned}$$

1.4 Optical Vortices

Topological defects that had attracted a lot of attention in view of their technological applications are the so-called **Optical Vortices**. There are a broad variety of applications of optical vortices in diverse areas of communications and imaging, from optical tweezers [7], to quantum computation [9], enhanced astronomical imaging and high-contrast coronagraph for exoplanet detection [10].

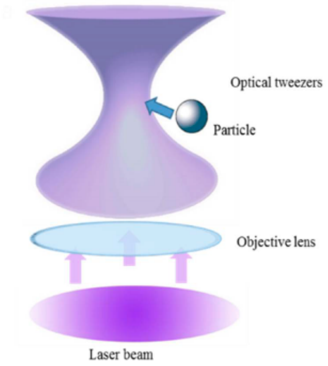

Figure 1.12: Optical Tweezer [7].

Optical vortices are singular points where the electromagnetic field goes to zero and around which the phase forms an n-armed spiral profile, with n the topological charge.

$$n = \frac{1}{2\pi} \oint_{\mathcal{C}} \nabla\varphi \cdot \mathrm{d}\vec{l},$$

where $\mathcal{C}$ is an arbitrary curve that goes around the singularity and φ is the field phase in complex representation.

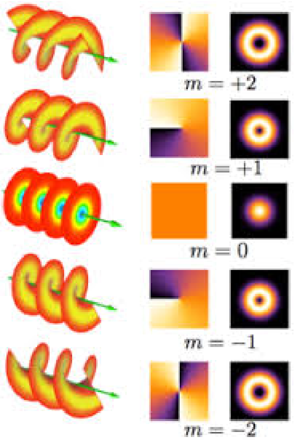

Figure 1.13: Optical Vortex

Different methods to generate optical vortices have been proposed: spiral phase [25], plates, diffractive elements [26], computer-generated holograms among others. Several of these methods are based on the light-matter interaction in liquid crystal media.

In a nematic liquid crystal light valve (LCLV) with a photosensitive substrate [27], the vortex induction is possible by transforming the intensity of the incoming light into a voltage that locally applies only across the illuminated regions, this enables the local induction of stable and positionally reconfigurable matter vortices, trapped at each location. This matter vortices, in turn, give rise to optical vortices via the transfer of spin-to-orbital angular momentum onto the incoming light.

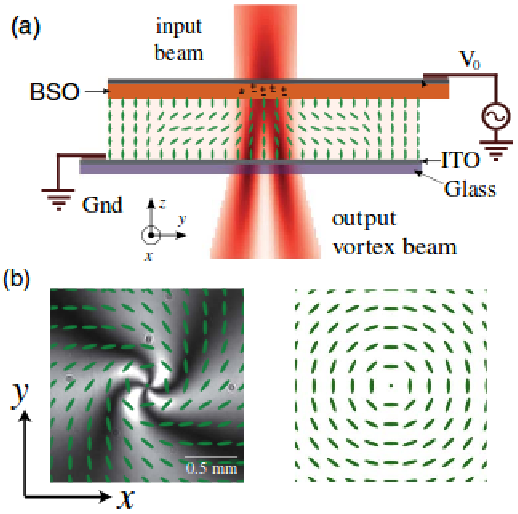

Figure 1.14: (a) Schematic representation of a LCLV. (b) Snapshot of a vortex in LCLV. (c) Representation of the directors projected on the plane [14]

1.5 Liquid Crystals

Liquid Crystals are materials that have local position and orientation correlation, but not at larger distances [2, 28], thus allowing them to flow and also to presente crystal-like properties. They have been a great source of interest since their discovery due to their optical properties and their use in technological applications, the most widely known being the Liquid Crystal Display (LCD)

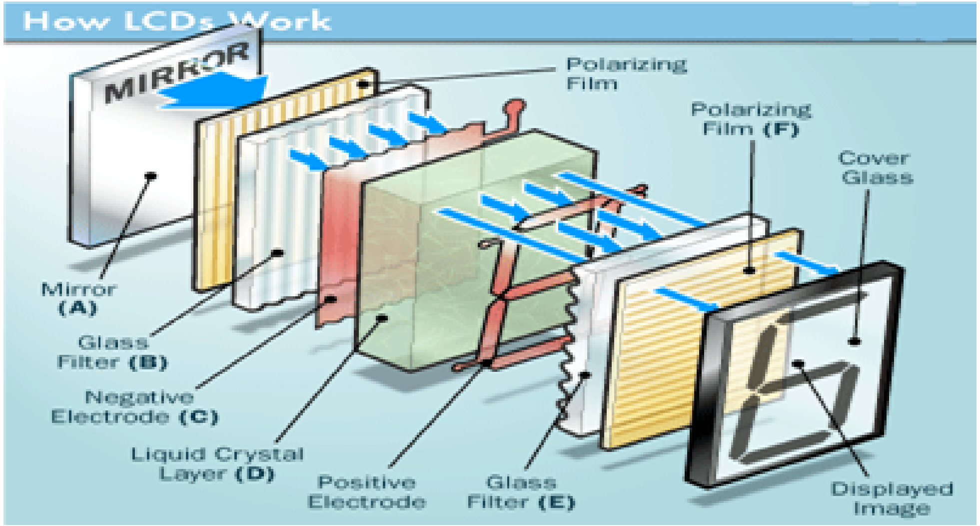

Figure 1.15: Liquid Crystal Display

Liquid crystals may appear in different phases depending on temperature (thermotropic state), straining conditions, and the particular properties of the chemical compound [29]. There are three principal phases: nematic, cholesteric and smectic. The nematic phase has the least order amount and the highest symmetry, presenting only orientational order of the long molecular axis. The cholesteric phase is similar to the nematic, but with chirality, meaning that it has a macroscopic helical structure. Finally, the smectic phase besides orientational order it also has positional order, having the molecules ordered in layers (cf. Fig. 1.16).

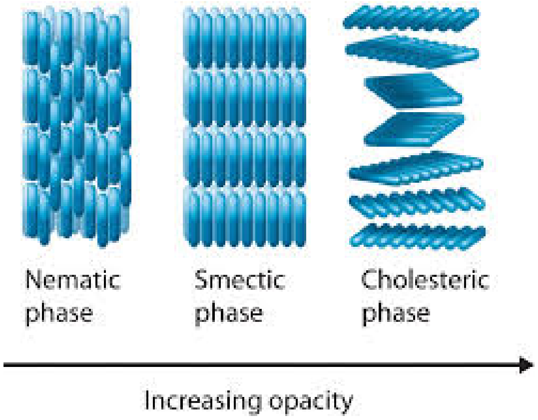

Figure 1.16: Liquid Crystal Classification

In the nematic mesophase, the molecules are elongated with a rod-like shape. The preferred direction may vary throughout the medium and is called a director. The orientation of the director is represented by a unit vector $\vec{n}(\vec{r},t)$. that describes the average molecule position in the liquid crystal. In a nematic, the molecules are able to rotate around their long axes, and there is no preferential arrangement of their ends, even if they differ. Hence, the sign of the director has no physical significance, and the nematic behaves optically as a uniaxial material with a center of symmetry.

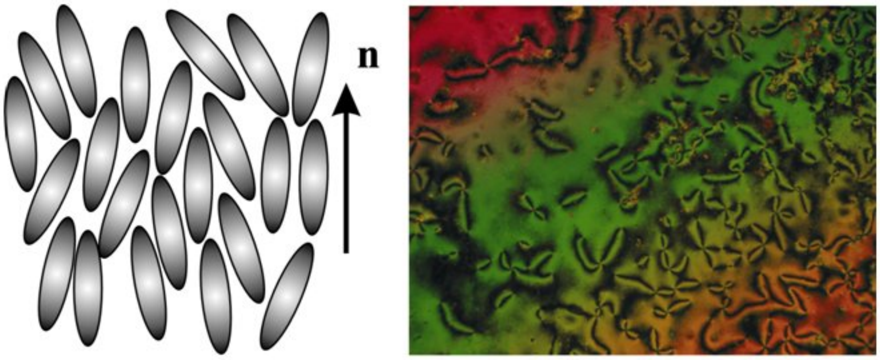

Figure 1.17: Nematic Liquid Crystal

Liquid Crystals are a highly dissipative medium whose dynamic is characterized by minimizing their elastic energy. In nematic materials there are three principal distinct director axis deformations: twist, splay and bend; each of these deformation has its own elastic constant giving rise to the Frank-Oseen Free energy density [2]:

$$\mathcal{F} = \frac{K_1}{2}(\nabla \cdot \vec{n})^2 + \frac{K_2}{2}(\vec{n} \times (\nabla \times \vec{n}))^2 + \frac{K_3}{2}(\vec{n} \times (\nabla \times \vec{n}))^2.$$

where K_1 corresponds to the splay deformation, K_2 to the twist deformation, and K_3 to the bend one. If the liquid crystal is subject to electric or magnetic fields, then those energy densities are added accordingly.

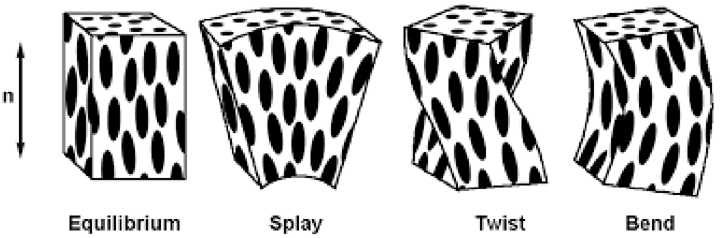

Figure 1.18: Principal deformations on a nematic liquid crystal

Chapter 2

Ginzburg Landau Equations

2.1 Dynamical Systems

A dynamical system is a manifold $\mathcal{M}$ called the *phase (state) space* endowed with a family of smooth evolution functions Φ^t that for any element of $t \in T$, map a point of the phase space back into the phase space.

Example The evolution function Φ^t is often the solution of a differential equation:

$$\begin{aligned} \dot{x} &= f(t, x), \\ x|_{t=0} &= x_0. \end{aligned}$$

Then $x(t) = \Phi(t, x_0)$.

When the evolution map Φ^t depends on a parameter μ, the structure of the phase space will also depend on this parameter.

Bifurcation theory considers a structure in the phase space (for example a fixed point or a periodic orbit) and studies its behavior as a function of the parameter μ [30, 31]. At the bifurcation point the structure may change its stability, split into new structures, or merge with other structures.

2.2 Bifurcations

To ilustrate this concept, let us consider the following autonomous dynamical system [32]:

$$\frac{\mathrm{d}\mathbf{x}}{\mathrm{d}t} = \mathbf{f}(\mathbf{x}; \mu), \tag{2.1}$$

where μ is a control parameter. In other words, this parameter allows a transition from one equilibrium to another. Suppose that $\mathbf{x} = \mathbf{x_0}$ is a fixed point (or steady state solution), i.e.:

$$f(\mathbf{x_0}; \mu) = 0.$$

To study the dynamics around $\mathbf{x_0}$, we consider $\mathbf{x} = \mathbf{x_0} + \delta\mathbf{x}$ with $\delta\mathbf{x}$ a small perturbation around the equilibrium. (Linear analysis). Replacing into (2.1) and linearizing in $\delta\mathbf{x}$:

$$\frac{\mathrm{d}}{\mathrm{d}t}\delta\mathbf{x} = \left[\frac{\partial \mathbf{f}}{\partial \mathbf{x}}(\mathbf{x_0})\right] \cdot \delta\mathbf{x}, \tag{2.2}$$

where the matrix $\left[\frac{\partial \mathbf{f}}{\partial \mathbf{x}}(\mathbf{x_0})\right]$ is the Jacobian of $\mathbf{f}$ evaluated at the equilibrium $\mathbf{x_0}$. Since the perturbation $\delta\mathbf{x}$ obeys a linear equation, its solution is:

$$\delta\mathbf{x} = \mathrm{e}^{\lambda t}\mathbf{v}.$$

Replacing into (2.1) one obtains:

$$\left[\frac{\partial \mathbf{f}}{\partial \mathbf{x}}(\mathbf{x_0}) - \lambda \mathbb{I}\right] \mathbf{v},$$

where $\mathbb{I}$ is the identity matrix. Such problem is soluble when:

$$\det\left(\frac{\partial \mathbf{f}}{\partial \mathbf{x}}(\mathbf{x_0}) - \lambda \mathbb{I}\right) = 0. \tag{2.3}$$

This is known as the *characteristic equation*,we note that since the left-hand side is a polynomial function of λ,it has n a priori complex roots, where n dimension of $\mathbf{x}$. For vector equations, the asymptotic stability of a state is determined by the real part of the eigenvalues because the imaginary part only generates oscillations at frequencies $\omega = \mathrm{Im}(\lambda)$, that is:

$$\delta\mathbf{x} = \sum_j \underbrace{\mathrm{e}^{\mathrm{Re}(\lambda_j)t}}_{\text{decay/growth}} \underbrace{\mathrm{e}^{\mathrm{i}\,\mathrm{Im}(\lambda_j)}}_{\text{oscillations}} \mathbf{v_j}.$$

where $\{\lambda_j\}_{j=1}^{n}$ are the eigenvalues and $\{\ v_j\}_{j=1}^{n}$ are their respective eigenvectors. If there is an eigenvalue with positive real part, then there is a direction of the phase space in which perturbations grow. In that case, the equilibrium $\mathbf{x_0}$ is unstable. If all the eigenvalues have negative real part, then the state is stable.

In general, the eigenvalues depend on the control parameter $\lambda = \lambda(\mu)$, and then a change of sign of the real part of one eigenvalue can be expected. This change in the stability of a state when a parameter is increased or decreased is called a *bifurcation* [33]. The eigenvector associated to the eigenvalue $\mathrm{Re}(\lambda) = 0$ is named a *critical mode*, and its direction define a **center manifold** in the phase space [34]. In a similar manner, we can define the **unstable manifold**, as the subspace spanned by the eigenvectors satisfying $\mathrm{Re}(\lambda) > 0$. Moreover, at the onset of instability the eigenvalue of the critical mode is small, $\mathrm{Re}(\lambda) \approx 0$, and then the center manifold is charaterized by a slow evolution. The rest of the phase space is the **stable manifold**, and in this region the evolution is much faster than in the central manifold. This behavior is known as a *temporal scales separation*; and it means that one or a few degrees of freedom are dynamical while all the others evolve fast. Separation of scales permits one to describe the system at long times in terms of a few relevant variables that corresponds to the **order parameters**.

The case when a solution changes its stability and two new stable solutions appear, it is called a **Supercritical Pitchfork Bifurcation** and it is common in systems with reflection symmetry.

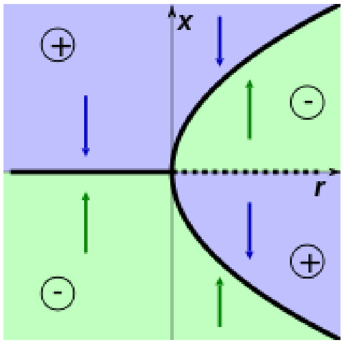

Figure 2.1: Supercritical Pitchfork Bifurcation

The simplest system that presents this bifurcation:

$$\partial_t x = \mu x - x^3,$$

here we recognize the bifurcation parameter μ and note that the bifurcation occurs at $\mu = 0$.

This system has three steady states: $x_0 = 0$ and $x_\pm = \pm\sqrt{\mu}$. The two last equilibria exist only for $\mu > 0$. The eigenvalue of x_0 is $\lambda_0 = \varepsilon$, therefore, this state loses its stability when μ becomes positive. The eigenvalues related to $x_\pm = -2\varepsilon$, then, this states are always stable.

2.3 Ginzburg Landau Equation

In extended systems, the dynamics can be described by an order parameter $A = A(\vec{r}, t)$ that is a function of time and space coordinates, hence its evolution is giving by a *partial differential equation*. Typically, the order parameter is a combination of the relevant fields in the system such that important changes can be easily visualized as changes in the order parameter.

If we consider the 2D bifurcation in extended systems,this is described by the following normal form :

$$\partial_t A = \mu A - |A|^2 A \tag{2.4}$$

and it is called a **Degenerated Pitchfork Bifurcation**.

In those systems, it is possible to find the emergence of *spatial instabilities*, depending on the parameters of the system. More generically when the amplitude of the order parameter goes to zero that point corresponds to a **defect**, because it breaks the translational invariance symmetry.

The simplest equation that describes the emergency of 2D defects in extended systems is the **Ginzburg Landau Equation** with real coefficientes:

$$\partial_t A = \mu A - |A|^2 A + \nabla^2 A, \tag{2.5}$$

The system above presents a **Degenerated Pitchfork Bifurcation** when $\mu = 0$, which means that the homegeneous state $A = \sqrt{\mu} e^{i\phi_0}$ can take any value of ϕ_0. In addition, due to initial conditions or fluctuations two solutions can exist in different locations simultaneously, these different locations are called **domains**. When this happens the two solutions are connected in a smooth way through an inhomogeneous solutions $A = \sqrt{\mu} e^{i\phi_0} \tanh x\sqrt{\mu/2}$ known in the literature as *kinks* [35].

Remark It is important to mention that this equation has a Lyapunov functional $\mathcal{F}$ so that $\partial_t A = -\frac{\delta \mathcal{F}}{\delta A}$, which means that the system is variational and has a relaxation dynamic, minimizing its free energy:

$$\mathcal{F} = \int \left(-\mu |A|^2 + \frac{|A|^4}{2} + \nabla A \nabla \bar{A} \right) \mathrm{d}S,$$

Indeed:

$$\begin{aligned} \frac{\mathrm{d}\mathcal{F}}{\mathrm{d}t} &= \int \left(\frac{\delta \mathcal{F}}{\delta A} \partial_t A + \frac{\delta \mathcal{F}}{\delta \bar{A}} \partial_t \bar{A} \right) \mathrm{d}S, \\ &= -2 \int \frac{\delta \mathcal{F}}{\delta A} \frac{\delta \mathcal{F}}{\delta \bar{A}} \leq 0. \end{aligned}$$

and the minimal energy solution corresponds to the homogeneous state $A = \sqrt{\mu} e^{i\phi_0}$, where ϕ_0 is an arbitrary phase.

2.3.1 Vortex solutions

Ginzburg Landau equations have been used to model a wide variety of physical systems (see, e.g. [1]). In the context of pattern formation the real Ginzburg Landau equation was first derived as long-wave amplitude equation in the conection with convection in binary mixtures near the onset of instability [36].

The complex Ginzburg Landau equation (also known as Gross-Pitaevsky equation) describe, among other things, macroscopic stationary states of superfluids, Bose-Einstein condensation, and solitary waves in plasmas [37]. In the recent years, it has become a subject of active mathematical research [38, 39, 40].

The stationary equation is simple to write:

$$-\Delta A + (|A|^2 - \mu) A = 0, \tag{2.6}$$

where (in the case of the entire plane) $A : \mathbb{R}^2 \to \mathbb{C}$ with the boundary condition:

$$|A| \to \sqrt{\mu} \quad \text{as} \quad |x| \to \infty,$$

The most studied particle type solution of this equation is the *Dissipative Vortex Solution*, i.e., a radially symmetric solution where the amplitude is axisymmetric and the phase grows continuously around the vortex: $A_m = R(r)\mathrm{e}^{\mathrm{i}(m\theta+\theta_0)}$, where (r, θ) are polar coordinates with the origin in the vortex position and θ_0 is an arbitrary parameter, related to the symmetry of the system, that shows explicitly the position of the phase discontinuity. Solutions A_m are called m vortices. We note that $m = \mathrm{deg}A_m$, where $\mathrm{deg}A_m$, the degree (or vorticity) of A is the total index (winding number) at ∞ of A considered as a vector field in $\mathbb{R}^2$, i.e.

$$\mathrm{deg}A = \frac{1}{2\pi} \int_{|x|=R} \mathrm{d}(argA),$$

for sufficiently large R.

The known facts about existence and properties of the vortex solutions are as follows:

1. Existence and uniqueness (modulo symmetry transformations and in a class of radially symmetric functions) [41].
2. Stability for $|n| \leq 1$, and instability for $|n| > 1$ [42].
3. Uniqueness of $A_{\pm 1})$ in a class of functions A with $\mathrm{deg}A = \pm 1$ and $\int (|A|^2 - 1)^2 < \infty$ [43].

Remark Also, solutions breaking the rotational symmetry were found to exist in the case of the Ginzburg-Landau equation in the ball $B_R = \{x \in \mathbb{R}^2 | |x| \leq R\}$ with the boundary condition $A|_{\partial B_R} = \mathrm{e}^{in\theta}$ and $|n| \geq 2$ ([38]). The boundary condition repels vortices, forcing their confinement. On the other hand, the energy is lowered by breaking up multiple vortices into $+1$ or -1 vortices and merging vortices of opposite signs. Thus, for R not very small, the lowest energy is reached by a configuration of $|n|$ vortices of degree $\pm$ depending on the sign of n, which, is not rotationally symmetric.

The function R(r) in the vortex solution A_m satisfies the ordinary differential equation:

$$\mathrm{e}^{\mathrm{i}(m\theta+\theta_0)} \left(\mu R - R^3 + \frac{\partial^2 R}{\partial r^2} + \frac{1}{r}\frac{\partial R}{\partial r} - \frac{m^2 R}{r^2} \right) = 0.$$

This equation does not have an analytic solution known, however we can find its asymptotic behavior close to infinity and near the origin [1].

$$R(r) \approx \begin{cases} \alpha_m r^{|m|} + \cdots, & r \to 0 \\ \sqrt{\mu} - \frac{m^2}{2} r^{-2} + \cdots, & r \to \infty \end{cases}$$

where α_m is a positive constant that depends on μ.

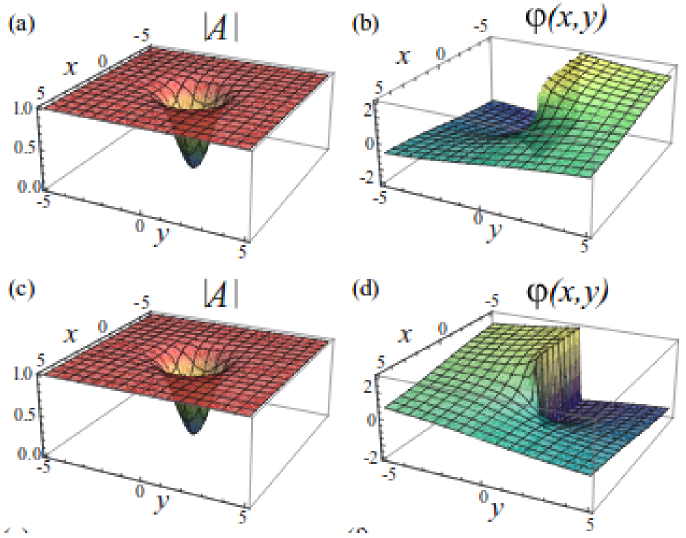

Figure 2.2: Ginzburg Landau Vortices with charges +1 and -1 [44]

We can calculate the energy $\mathcal{E}$ of the vortex, without lose of generality, we take $\mu = 1$, so we can write the energy:

$$\mathcal{E} = \frac{1}{2}\int \nabla A \nabla \bar{A} + \frac{1}{2}(1 - |A|^2)^2 \mathrm{d}S,$$

replacing the vortex solution $A = R_v \mathrm{e}^{\mathrm{i}m\theta}$:

$$\mathcal{E} = \frac{1}{2}\int (\partial_r R_v)^2 + \frac{m^2 R_v^2}{r^2} + \frac{1}{2}(1 - R_v^2)^2 \mathrm{d}S,$$

since R_v depends only in the absolute value of m, the energy of a vortex depends only on the size of the charge but not on its sign. We can write the energy $\mathcal{E}$ as:

$$\mathcal{E} = \underbrace{\pi \int_0^\infty \left((\partial_r R_v)^2 + \frac{m^2 R_v^2}{r^2} \right) r\mathrm{d}r}_{\mathcal{E}_1} + \underbrace{\frac{\pi}{2}\int_0^\infty (1 - R_v^2)^2 r\mathrm{d}r}_{\mathcal{E}_2},$$

the first term is divergent in an infinite domain, but the second can be solved analytically using the R_v is the vortex profile:

$$\mathcal{E}_2 = \pi \int_0^\infty (1 - R_v^2) R_v R_v' r^2 \mathrm{d}r = -\pi \int_0^\infty \left(r R_v' \frac{\mathrm{d}(rR'v)}{\mathrm{d}r} - m^2 R_v R_v' \right) \mathrm{d}r = \frac{\pi m^2}{2}.$$

It can be shown that considering a cut-off distance L (see Remark), the divergent term depends on a numerical constant a_0 giving by the specific shape of the vortex core solution:

$$\mathcal{E}_1 = \pi m^2 \ln\left(\frac{L}{a_0}\right),$$

then we get:

$$\mathcal{E} = \pi m^2 \ln\left(\frac{L\sqrt{\mathrm{e}}}{a_0}\right).$$

Hence, both vortices are indistinguishable from the point of view of their magnitude. Notice that this is the same result obtained by Berezinskii-Kosterlitz-Thouless.

Remark The Ginzburg Landau equation is invariant under the following symmetries:

- Spatial translation invariance: $\vec{r} \to \vec{r} + \vec{r}_0$.
- Coordinates rotation: $\varphi \to \varphi + \varphi_0$
- Coordinates reflection: $\varphi \to -\varphi$
- Phase invariance: $A \to A\mathrm{e}^{\mathrm{i}\varphi_0}$
- Reflection invariance: $A \to \bar{A}$

Remark Note that equation (2.6) is the equation for critical points of the Ginzbunrg-Landau functional

$$\mathcal{F}[A] = \frac{1}{2}\int \left(|\nabla A|^2 + \frac{1}{2}(|A|^2 - 1)^2 \right) \mathrm{d}^2x$$

But we have the following theorem [42]:

Theorem 2.1 *Let φ be a $\mathcal{C}^1$ vector field in $\mathbb{R}^2$ s.t. $|\varphi| \to 1$ as $|x| \to \infty$. If $\mathrm{de}f\varphi \neq 0$, then $\mathcal{F}[\varphi] = \infty$.*

Thus is we want to use energetic arguments for vortices we have to modify $\mathcal{F}$ as follows [42]

$$\mathcal{F}_{ren}[\varphi] = \frac{1}{2}\int \left(|\nabla\varphi|^2 - \frac{(\mathrm{de}g\varphi)^2}{r^2}\chi + \frac{1}{2}(|\varphi|^2 - 1)^2 \right) \mathrm{d}^2x$$

where $r = |x|$ and χ is a smooth cut-off function

$$\chi = \begin{cases} 0 & \text{for } r \leq 1 \\ 1 & \text{for } r \geq 2 \end{cases}$$

Chapter 3

Vortex Induction

3.1 Experimental Setup

Nematic liquid crystals with negative anisotropic dielectric constant and homeotropic anchoring are a natural physical context where dissipative vortices are observed [2, 28].

Furthermore, it is possible to produce optical vortices through the induction of a material vortex in a Liquid Crystal Light Valve(LCLV) under suitable illumination conditions [14, 15].

The LCLV is composed of a thin nematic liquid-crystal film sandwiched between a glass and a photoconductive plate. The LCLV is filled with a nematic mixture exhibiting negative dielectric anisotropy. The transparent interfaces are treated in order to provide a homeotropic alingment of the liquid crystals, that is, close to the walls the liquid crystal molecules are perpendicular to the confining layers (homeotropic configuration), one of which is the photoconductive slab.

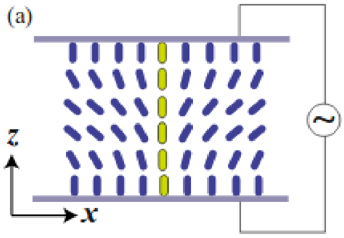

Figure 3.1: Schematic representation of a Liquid Crystal Light Valve [44]

If the material has negative dielectric constant ε_a, then when a voltage is applied to the plates, the molecules will tend to align perpendicular to the electric field in order to reduce their energy. This electric forces opposes the elasticity if there homeotropic, therefore, for low voltages the sample remains in equilibrium, but if the voltage is increased a transition occurs at the **Freedericksz Voltage** and a *schlieren texture* appears [45].

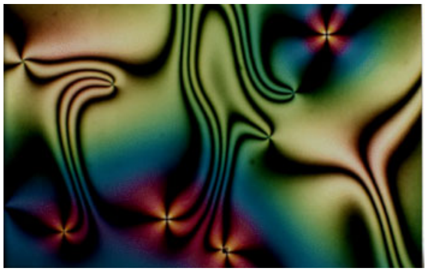

Figure 3.2: Schlieren Texture [46]

This transition is a *Degenerated Pitchfork Bifurcation*, where the molecules leave the vertical axis in an angle that depends on the magnitude of the voltage, but there is a cone of possible equilibrium positions for the molecules. Two types of stable vortices with opposite charges are observed, which are characterized by being attracted (repulsed) to the opposite (identical) topological charge.

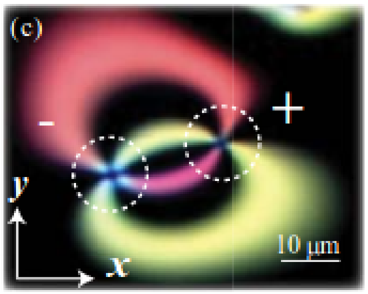

Figure 3.3: Umbilical Defects [44]

Owing to the photoconductive substrate, when the LCLV is illuminated by a Gaussian light beam, the effective voltage drop across the LC layers acquires a bell shaped profile (see Section 3.2), peaked in the center of the illuminated area and able to overcome the critical value of the Freédericksz transition for which the molecules start to reorient owing to the torque exerted by the electric field.
The created defect, couples orbital and spin components of the optical angular momentum; hence, the outgoing beam acquires a helical wavefront. This allows the creation of **Gauss Laguerre** modes in the light once it has crossed the sample. These modes correspond to an optical vortex, i.e, light modes with a singularity at their centre that carry angular momentum.

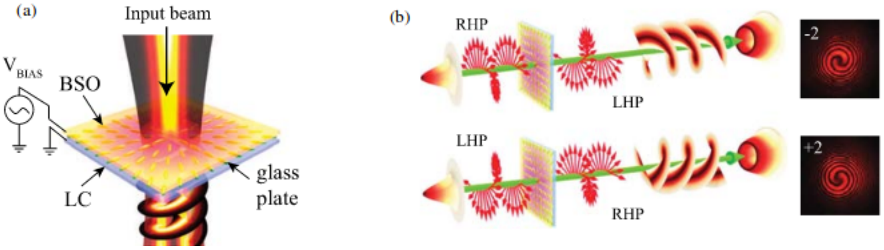

Figure 3.4: Optical Vortex Induction [47]

3.2 Anisotropic Laplace Equation

To calcule the electric field inside a LCLV, the cell is modelled as two infinite planar parallel plates separated by a distance d in the z axis, where the photoconductor is in $z = \mathrm{d}$ and has a gaussian-shaped voltage drop, and the other plate is taken as reference, thus the boundary conditions are:

$$\begin{aligned} V(r,\theta,z=\mathrm{d}) &= V_0 + \alpha I(r). \\ V(r,\theta,z=0) &= 0. \end{aligned}$$

where $I(r)$ is proportional to the light intensity that illuminates the sample and has a gaussian profile: $I(r) = I_0 \mathrm{e}^{-r^2/\omega^2}$, where I_0 is the intensity peak and ω is the waist of the beam. Introducing cylindrical coordinates at the center of the gaussian beam, the voltage satisfies the **anisotropic Laplace equation** [48]:

$$\partial_{zz} V + \frac{\varepsilon_\perp}{\varepsilon_\parallel} \nabla_\perp^2 V = 0,$$

where $\nabla_\perp^2 V$ is the laplacian in the transversal coordinates, $\varepsilon_\perp$ is the dielectric constant of the LC for the perpendicular electrical field and $\varepsilon_\parallel$ is the dielectric constant for the parallel one. By using Fourier transform in the parallel plane to the plates one obtains for the voltage:

$$\hat{V}(z,k) = \frac{1}{\sqrt{2\pi}} \int_{-\infty}^{\infty} \mathrm{e}^{\mathrm{i}k\cdot r_\perp} V(z, r_\perp) \mathrm{d}r_\perp,$$

and for the equation:

$$\partial_{zz} \hat{V} - \frac{\varepsilon_\perp}{\varepsilon_\parallel} k^2 \hat{V} = 0. \tag{3.1}$$

Aplying the boundary condition $V(z=0) = 0$, the solution of (3.1) only have odd modes, obtaining:

$$\hat{V}(z,k) = A(k) \frac{\sinh\left(\sqrt{\frac{\varepsilon_\perp}{\varepsilon_\parallel}} kz\right)}{\sinh\left(\sqrt{\frac{\varepsilon_\perp}{\varepsilon_\parallel}} k\mathrm{d}\right)}.$$

Using the inverse Fourier transform:

$$V(z,r) = \frac{1}{\sqrt{2\pi}} \int_{-\infty}^{\infty} \mathrm{d}k \mathrm{e}^{-\mathrm{i}k\cdot r_\perp} A(k) \frac{\sinh\left(\sqrt{\frac{\varepsilon_\perp}{\varepsilon_\parallel}} kz\right)}{\sinh\left(\sqrt{\frac{\varepsilon_\perp}{\varepsilon_\parallel}} k\mathrm{d}\right)}, \tag{3.2}$$

considering the boundary condition at the photoconductor:

$$V(r,\mathrm{d}) = V_0 + \alpha I(r/\omega) = \frac{1}{2\pi} \int_{-\infty}^{\infty} \mathrm{d}k \mathrm{e}^{-\mathrm{i}k\cdot r_\perp} A(k) \tag{3.3}$$

using again Fourier transform it follows:

$$A(k) = \frac{1}{\sqrt{2\pi}} \int_{-\infty}^{\infty} \mathrm{d}r_\perp \mathrm{e}^{\mathrm{i}k\cdot r_\perp} (V_0 \alpha I(r_\perp/\omega)). \tag{3.4}$$

Replacing (3.4) in (3.1) one obtains the solution to the initial equation:

$$V(z,r)=\frac{1}{\sqrt{2\pi}}\int_{-\infty}^{\infty}\mathrm{d}k\mathrm{e}^{-\mathrm{i}k\cdot r_\perp}\frac{\sinh\left(\sqrt{\frac{\varepsilon_\perp}{\varepsilon_\parallel}}kz\right)}{\sinh\left(\sqrt{\frac{\varepsilon_\perp}{\varepsilon_\parallel}}k\mathrm{d}\right)}\left(\int_{-\infty}^{\infty}\mathrm{d}r_\perp^*\mathrm{e}^{\mathrm{i}k\cdot r_\perp^*}(V_0\alpha I(r_\perp/\omega))\right).$$

For the sake of simplicity; one can consider the limit of a Gaussian beam sufficiently flattened ($\omega\to\infty$). This limit is consistent with experimental observations, since the beam waist (about 200 μm) is much larger than the size of the vortex (5 μm). In this aproximation:

$$\frac{\sinh\left(\sqrt{\frac{\varepsilon_\perp}{\varepsilon_\parallel}}kz\right)}{\sinh\left(\sqrt{\frac{\varepsilon_\perp}{\varepsilon_\parallel}}k\mathrm{d}\right)}\approx\frac{z}{\mathrm{d}}+\mathcal{O}\left(\frac{1}{\omega^2}\right),\tag{3.5}$$

then:

$$V(z,r)\approx\frac{z}{\mathrm{d}}\frac{1}{\sqrt{2\pi}}\int_{-\infty}^{\infty}\int_{-\infty}^{\infty}\mathrm{d}q\mathrm{d}p\mathrm{e}^{\mathrm{i}q(p-r/\omega)}(V_0+\alpha I(p))=\frac{z}{\mathrm{d}}\int_{-\infty}^{\infty}\mathrm{d}p\delta(p-r/\omega)(V_0+\alpha I(p)),$$

solving the integral, at first order the voltage inside the valve is giving by [48]:

$$V(z,r)\approx\frac{z}{\mathrm{d}}(V_0+\alpha I(r/\omega)).$$

Then, the electric field $E(r,\theta,z)$ inside the LCLV takes the form:

$$\vec{E}=-\vec{\nabla}V=E_z\hat{z}+E_r\hat{r}=-\frac{1}{\mathrm{d}}\left[V_0+\alpha I\left(\frac{r}{\omega}\right)\right]\hat{z}-\frac{z\alpha}{\mathrm{d}\omega}\frac{\mathrm{d}I(r/\omega)}{\mathrm{d}r}\hat{r},$$

with $\hat{z}$ and $\hat{r}$ the unitary vectors in cylindrical coordinates. Note that the electric field contains an axis-symmetrical structure (c.f. Fig. 3.5). This structure of the electric field projected onto the $x-y$ plane corresponds to a vortex with positive charge and zero phase as is shown in Figure 3.6

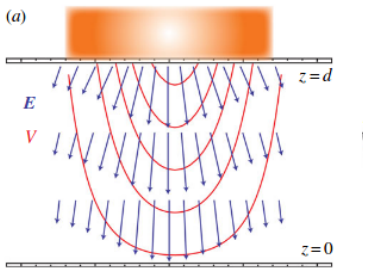

Figure 3.5: Vertical cross section [49]

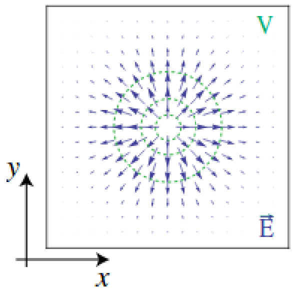

Figure 3.6: Horizontal cross section

3.3 Amplitude Equation

The description of the nematic liquid crystal is given by the director vector $\vec{n}$, which accounts for the molecular order. The dynamical equation for the director $\vec{n}$ comes from the Frank-Oseen Free Energy Density [2, 28]:

$$\mathcal{F} = \frac{K_1}{2}(\nabla \cdot \vec{n})^2 + \frac{K_2}{2}(\vec{n} \times (\nabla \times \vec{n}))^2 + \frac{K_3}{2}(\vec{n} \times (\nabla \times \vec{n}))^2 + \frac{\varepsilon_a}{2}(\vec{E} \cdot \vec{n})^2.$$

Minimizing the free energy, with the aditional constraint $|\vec{n}| = 1$ the Euler-Lagrange equation for the director reads:

$$\gamma \frac{\mathrm{d}\vec{n}}{\mathrm{d}t} = -\frac{\delta \mathcal{F}}{\mathrm{d}\vec{n}} + \vec{n}\left(\vec{n} \cdot \frac{\delta \mathcal{F}}{\delta \vec{n}}\right), \tag{3.6}$$

thus follows:

$$\begin{aligned}\gamma \partial_t \vec{n} = \quad & K_3 \quad [\nabla^2 \vec{n} - \vec{n}(\vec{n} \cdot \nabla^2 \vec{n})] + (K_3 - K_1)[\vec{n}(\vec{n} \cdot \vec{\nabla})(\vec{\nabla} \cdot \vec{n}) - \vec{\nabla}(\vec{\nabla} \cdot \vec{n})] \\ + \quad & (K_2 - K_3)[2(\vec{n} \cdot \nabla \times \vec{n})(\vec{n}(\vec{n} \cdot \nabla \times \vec{n}) - \nabla \times \vec{n}) + \vec{n} \times \nabla(\vec{n} \cdot \nabla \times \vec{n})] \\ - \quad & \varepsilon_a (\vec{n} \cdot \vec{E})(\vec{n}(\vec{n} \cdot \vec{E}) - \vec{E}),\end{aligned}$$

where γ is the relaxation time, ε_a is the anisotropic dielectric constant that accounts for non-linear response, $\{K_1, K_2, K_3\}$ are the nematic liquid crystal elastic constants, which acounts for the elastic deformation of splay, twist, and bend type, respectively. Under uniform illumination, the electric field is given by $\vec{E} = (V/\mathrm{d})\hat{z} = E_z \hat{z}$, where E_z is the root mean square amplitude of the electric field, V is the applied voltage, and d is the thickness of the liquid crystal layer.

A trivial equilibrium of the liquid crystal layer is the homeotropic state, $\vec{n} = \hat{z}$. This state undergoes a degenerate stationary instability due to the effect of the electric field, setting $\vec{n} = \left(u, v, 1 - \frac{u^2+v^2}{2}\right)$ where u, v are small perturbations, we obtain at first order:

$$\begin{aligned}\gamma \dot{u} &= K_3 \partial_{zz} u - \varepsilon_a E^2 u, \\ \gamma \dot{v} &= K_3 \partial_{zz} v - \varepsilon_a E^2 v.\end{aligned}$$

By taking a solution of the form $u(z,t) = u_0 \mathrm{e}^{\sigma t} \sin(\pi n z/\mathrm{d})$ and $v(z,t) = v_0 \mathrm{e}^{\sigma t} \sin(\pi n z/\mathrm{d})$ with $\{u_0, v_0\}$ constants and n an integer number, we obtain the rate growthn relation:

$$\gamma \sigma = -K_3 k^2 - E^2 \varepsilon_a,$$

where $k = \frac{n\pi}{\mathrm{d}}$, this shows that the first wavelenght that destabilizes the system is $k_c = \frac{\pi}{\mathrm{d}}$, and solving for the electric field we obtain the minimum value that causes movement in the molecules:

$$E = \sqrt{\frac{-K_3 \pi^2}{\varepsilon_a \mathrm{d}^2}},$$

and thus the critical *Freedericksz Voltage* is $V_F = \sqrt{-K_3 \pi^2/\varepsilon_a}$ [45]. Then, the director undergoes orientational instability, i.e., the molecules do not want to aling with the electric field. As a result of elastic coupling between the molecules the director has a cone of possible equilibria. Figure 3.7 illustrates a degenerate Pitchfork bifurcation.

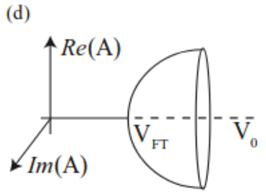

Figure 3.7: Freedericksz Bifurcation

When the illumination has a Gaussian profile, close to the transition point we introduce the ansatz:

$$n(r,\theta,z) \approx \begin{pmatrix} u(r,\theta,t)\sin\left(\frac{\pi z}{\mathrm{d}}\right) \\ w(r,\theta,t)\sin\left(\frac{\pi z}{\mathrm{d}}\right) \\ 1-\frac{(u^2+w^2)}{2}\sin^2\left(\frac{\pi z}{\mathrm{d}}\right) \end{pmatrix}.$$

Introducing the above ansatz in the director equation, integrating in the z coordinate over one period, and defining the complex amplitude $A = u + \mathrm{i}w$, after straightforward calculations (see Appendix) one obtains the **Topologically Driven Ginzburg Landau Equation**:

$$\gamma\partial_t A = \mu A - aA|A|^2 + \nabla_\perp^2 A + \delta\partial_{\eta,\eta}\bar{A} + bf(r)\mathrm{e}^{\mathrm{i}\theta}, \tag{3.7}$$

where $\mu(r) = -K_3(\pi/\mathrm{d})^2 - \varepsilon_a(V_0+\alpha I)^2/\mathrm{d}^2$ is the bifurcation parameter, $a = -[K_3(\pi/\mathrm{d})^2/4 + 3\varepsilon_a(V_0+\alpha I)^2/4\mathrm{d}^2] > 0$ is the linear response, $b = 2\varepsilon_a \mathrm{d}\alpha V_0/\pi$, $\partial_\eta = \partial_x + \mathrm{i}\partial_y$, $\delta = (K_1 - K_2)/(K_1+K_2)$ stands for the anisotropy elasticity of the system, and $f(r) = \frac{I_0 r}{\omega^2}\mathrm{e}^{-r^2/2\omega^2}$ is strength of the external forcing.

The external forcing is generated by the inhomogeneous radial electric field, which in turn is induced by the inhomogeneous profile of the light beam. The forcing term is responsible for inducing a matter vortex with positive charge in the centre position where the applied Gaussian beam is peaked, which is at origin of the self-stabilization mechanism for the vortex induction. A simple explanation of the origin of this vortex is due to the structure of the electric field (see Fig. 3.5), the molecules are oriented forming a positive charged vortex configuration.

Without forcing and anisotropy this equations corresponds to the **Ginzburg Landau Equation**, with real coefficients, which admits stable dissipative vortex solutions with topological charge (winding number) ±1. The presence of anisotropy breaks the symmetry, and the +1 vortex is energetically favored with respect to −1.

Similar equation were derived before: using the method of homogenization for nematic liquid crystals near the Fréedericksz transition [45], and for modeling self-organization in an array of microtubules interacting via molecular motors [50].

3.4 Anisotropic Ginzburg Landau Equation

Ignoring the inhomogeneous forcing, the amplitude of the critical mode satisfies the *Anisotropic Ginzburg Landau* equation:

$$\gamma\partial_t A = \mu_0 A - aA|A|^2 + \nabla_\perp^2 A + \delta\partial_{\eta,\eta}\bar{A}. \tag{3.8}$$

This equation has lost the independent rotational symmetries $A \to A\mathrm{e}^{\mathrm{i}\theta}$ and $z \to z\mathrm{e}^{\mathrm{i}\theta}$ with $\theta \in (0, 2\pi)$, retaining only the joint symmetry $A(z) \to \mathrm{e}^{-\mathrm{i}\theta}A(z\mathrm{e}^{\mathrm{i}\theta})$ [44].
Note that equation (3.8) can be rewritten in the form:

$$\partial_t A = -\frac{\delta\mathcal{E}}{\delta\bar{A}},$$

where the free energy is:

$$\mathcal{E}(A,\delta) = \int_\Omega \mathrm{d}S\left[|\nabla A|^2 + \frac{1}{2}(\mu_0 - |A|^2)^2 + \delta\mathrm{Re}\{(\partial_\eta\bar{A})^2\}\right], \tag{3.9}$$

where $\Omega \subset \mathbb{R}^2$ is a bounded domain [1].

The trivial equilibria that minimize the free energy are $|A|^2 = \mu_0$. However, this equation has nontrivial inhomogeneous equilibria.

Using the notation $\mathcal{R}_{\varphi_0}$ for a rotation by a angle φ_0 of $\mathbb{R}^2$ about the origin, a short calculation shows that when $\varphi_0 = \pi/2$:

$$\mathcal{E}(A,\delta) = \mathcal{E}(A\circ\mathcal{R}_{\varphi_0}, -\delta) = \mathcal{E}(\mathcal{R}_{\varphi_0}A, -\delta).$$

Moreover, $\mathcal{E}$ has a fourfold symmetry in the sense that:

$$\mathcal{E}(A,\delta) = \mathcal{E}[\mathcal{R}_{m\pi/2}A\circ\mathcal{R}_{k\pi/2}, (-1)^{m+k}\delta].$$

By introducing the ansatz $A(r,\theta) = R(r)\mathrm{e}^{\mathrm{i}(\theta+\varphi_0)}$ in equation (3.8) for the vortex solution with positive topological charge, we obtain the following set of scalar equations:

$$0 = \mu_0 R - aR^3 + (1 + +\delta\mathrm{e}^{-2\mathrm{i}\varphi_0})\left(\frac{\mathrm{d}^2R}{\mathrm{d}^2r} + \frac{1}{r}\frac{\mathrm{d}R}{\mathrm{d}r} - \frac{R}{r^2}\right). \tag{3.10}$$

$$0 = \delta\sin 2\varphi_0\left(\frac{\mathrm{d}^2R}{\mathrm{d}^2r} + \frac{1}{r}\frac{\mathrm{d}R}{\mathrm{d}r} - \frac{R}{r^2}\right). \tag{3.11}$$

From equation (3.11), the only possibility to obtain a nontrivial solution is to consider the phase parameter satisfying $\sin 2\varphi_0 = 0$, which gives the discrete solutions $\varphi_0 = \{0, \pi/2, \pi, 3\pi/2\}$ and which is consistent with the fourfold symmetry mentioned above. On the other hand, the equation for the magnitude of the amplitude reads:

$$0 = \mu_0 R - R^3 + (1 + \cos 2\varphi_0)\left(\frac{\mathrm{d}^2R}{\mathrm{d}^2r} + \frac{1}{r}\frac{\mathrm{d}R}{\mathrm{d}r} - \frac{R}{r^2}\right).$$

---

[1] The energy of vortex solutions diverges in unbouded domains (c.f. Remarks Section [2.3])

Since $\varphi_0 = \{0, \pi/2, \pi, 3\pi/2\}$, we must have $\cos 2\varphi_0 = \pm 1$. Rescaling the space by the factor $\sqrt{1 \pm \delta}$, the isotropic solution is recovered:

$$A = R_v^{\pm}\left(\frac{r}{\sqrt{1 \pm \delta}}\right) \mathrm{e}^{\mathrm{i}(\theta + \frac{\pi}{4} + \mp \frac{\pi}{4} + n\pi)}.$$

with R_v the magnitude of the vortex solution of the Ginzburg Landau equation $n = 0, \pm 1, \pm 2, \ldots$. Consequently, the anisotropic vortex solution corresponds to a scaling of the isotropic vortex solution, with a finite number of possible phase jumps.

Remark Note that the vortex solution of the anisotropic Ginzburg Landau equation is not well-defined for $\delta = \pm 1$, this extremes cases occurs when one of the elastic constants (K_1 or K_2) diverges. This happens when the liquid crystal goes through a phase transition from the nematic state to a smetic one.

To study the existence, stability properties and bifurcation diagram of the vortex solution with positive topological charge, one can analize the properties of the free energy $\mathcal{E}(A, \delta)$. Using the vortex solution $A = R_v^{\pm}(r/\sqrt{1 \pm \delta})\mathrm{e}^{\mathrm{i}(\theta + \varphi_0)}$, where $+$ stands for $\varphi_0 = \{0, \pi\}$ and $-$ for $\varphi_0 = \{\pi/2, 3\pi/2\}$, and taking $\Omega = B(0, L)$ we obtain:

$$\mathcal{E}_A = \pi \int_0^L \left\{ (\partial_r R_v)^2 + \frac{R_v^2}{r^2} + \frac{1}{2}(1 - R_v^2)^2 + \delta \cos(2\varphi_0)\left(\partial_r R_v + \frac{R_v}{r}\right)^2 \right\} r \mathrm{d}r,$$

changing variables $\rho = r/\sqrt{1 \pm \delta}$, we obtain:

$$\mathcal{E}_A = \pi \int_0^{L/\sqrt{1 \pm \delta}} \left\{ (\partial_\rho R_v(\rho))^2 + \frac{R_v^2(\rho)}{\rho^2} + \frac{(1 \pm \delta)(1 - R_v^2(\rho))^2}{2} \pm \delta \left(\partial_\rho R_v(\rho) + \frac{R_v(\rho)}{\rho}\right)^2 \right\} \rho \mathrm{d}\rho,$$

after straightforward calculations (see [48]), the energy of the vortex with positive topological charge is:

$$\mathcal{E} = \pi \ln\left(\frac{L}{a_0\sqrt{1 \pm \delta}}\right) + \frac{\pi(1 \pm \delta)}{2} \pm \pi\delta\left(\ln\left(\frac{L}{a_0\sqrt{1 \pm \delta}}\right) + 1\right).$$

This expression shows that the scaling that makes the core smaller is the one with less energy and, therefore, preferred by the system.

Chapter 4

Rayleigh Vortex

4.1 Rayleigh Vortex

In the context of the LCLV experimental setup described in Sec[3.1], we can consider the topologically driven Ginzburg Landau equation (3.7):

$$\gamma\partial_t A = \mu A - aA|A|^2 + \nabla_\perp^2 A + \delta\partial_{\eta,\eta}\bar{A} + bI'\mathrm{e}^{\mathrm{i}\theta}, \tag{4.1}$$

with the parameters given in Sec[3.3] and $I' = \sqrt{(\partial_x I)^2 + (\partial_y I)^2}$. When the LCLV is forced with a single beam of sufficiently intense light, it always induces a vortex of positive charge at the center of the beam [14, 15]. To characterize analytically the solutions of equation (4.1), we assume $\mu(r) < 0$ (i.e in a region below the Fréedericksz transition) and consider a single ray of light with intensity $I = I_0\mathrm{e}^{r_\perp^2/\omega^2}$, where I_0 and ω are, the stregth and waist of the light beam, and $r_\perp = \sqrt{x^2+y^2}$ is the radial coordinate with its origin in the center of the beam. We can renormalize the variables using the width ω of the gaussian beam: $\rho = r/\omega$ and renaming constants

$$\partial_t A = \underbrace{\left(\mu_0 + \beta\mathrm{e}^{-\rho^2}\right)}_{\mu(r)<0} A - |A|^2 A + \frac{1}{\omega^2}\nabla^2 A + \frac{\delta}{\omega^2}\partial_{\eta\eta}\bar{A} + \mu_1\frac{\rho}{\omega}\mathrm{e}^{-\rho^2}\mathrm{e}^{\mathrm{i}\theta}. \tag{4.2}$$

When $\omega \gg 1$ and $I \ll 1$, we find the following approximate stationary solution

$$A_R(r_\perp,\theta) = -\frac{bI'(x,y)}{\mu}\mathrm{e}^{\mathrm{i}\theta} = \frac{\mu_1}{\omega^2\mu} r_\perp \mathrm{e}^{-r_\perp^2/\omega^2}\mathrm{e}^{\mathrm{i}\theta}, \tag{4.3}$$

where θ is the angular coordinate with its origin in the center of the Gaussian. It can be checked that the error of this approximate solution is of order $O\left(\frac{1}{\omega^6}\right)$, in other words, the nonlinear term and the spatial derivatives are negligible in this limit. We called this solution the **Rayleigh vortex** after the Rayleigh distribution [51]. Figures 4.1 shows surface plot, vectorial representation, and phase of the Rayleigh vortex.

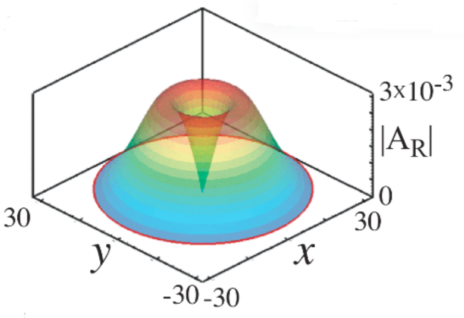

(a) Surface plot of Rayleigh vortex

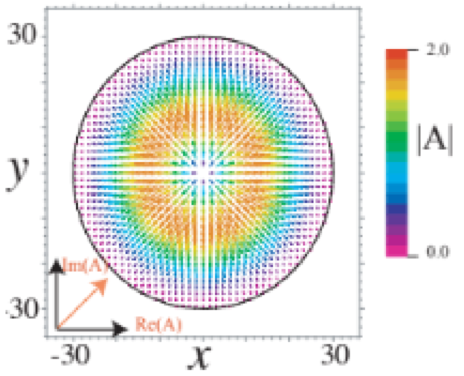

(b) Vector representation of the vortex solution. The colors show the magnitude of the amplitude $|A|$

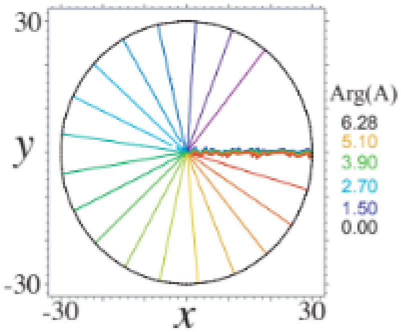

(c) Countour plot of the phase of amplitude A, $arg(A) = Im(A)/Re(A)$

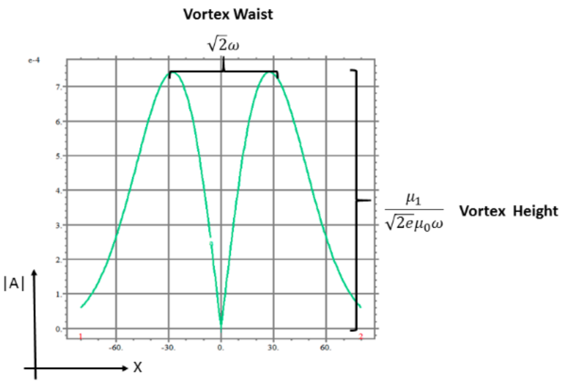

(d) Rayleigh vortex profile

Figure 4.1: Rayleigh vortex of the topologically driven Ginzburg Landau equation with $\mu = -3$,$a = 1$, $\delta = 0$,$b = 1$,$I_0 = 0.01$ and $\omega = 30$. The colors account for the magnitude of the amplitude

4.2 Numerical Results

The maximum value h that the vortex reaches corresponds to vortex height, $h = 2bI_0/\mu\omega\sqrt{2\mathrm{e}}$ and the width of the vortex is $l = \omega/\sqrt{2}$ (c.f. Fig. 4.1). Figure 4.2 shows a comparison between numerical solutions of the topologically driven Ginzburg Landau equation (4.1) and the approximation (4.2). From this figure we infer that for a light beam of big waist the Rayleigh vortex is an excellent approximation of the topologically driven Ginzburg Landau vortex. For light beams of order one, the effect of the Laplacian and the nonlinear term begins to play a role, and the Rayleigh solutions ceases to be dominant.

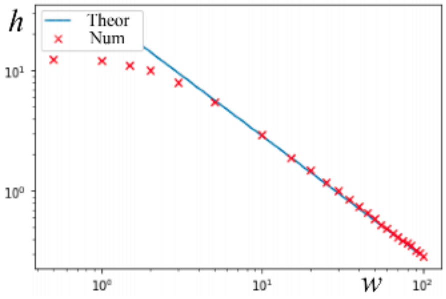

Figure 4.2: Log-log plot of the height of the vortex as function of beam waist ω. The heights obtained by numerical simulations of the topologically forced Ginzburg Landau equation(crosses) with $\mu = -3$,$a = 1$, $\delta = 0$,$b = 1$,$I_0 = 0.01$ are compared with $h = 2bI_0/\mu\omega\sqrt{2\text{e}}$.

In Figure 4.3 we can observe the form of the numerical solution as the effect of the neglected terms becomes noticiable.

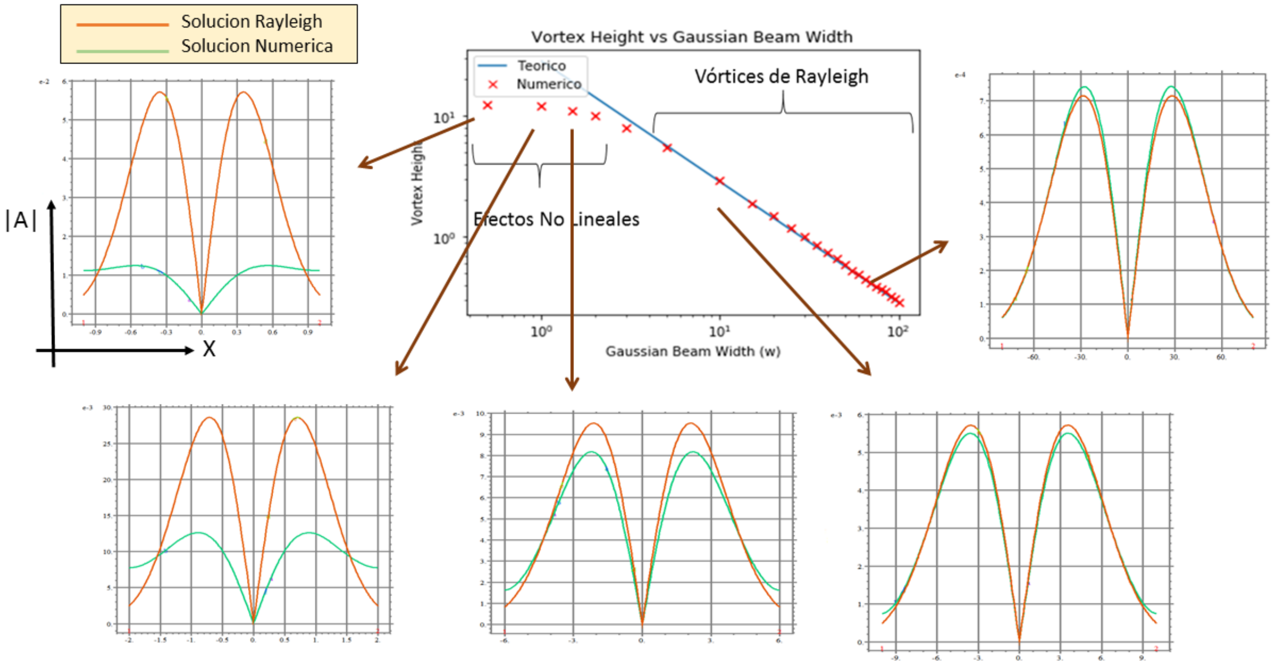

Figure 4.3: Numerical comparison of the Rayleigh solution and the vortices obtained from equation (4.1)

To give actual physical sense to the condition $\omega \gg 1$, we need to build-up a dimensionless number from the constants of the problem:

$$\frac{\omega\gamma^2}{K} \gg 1$$

where γ is the rotational viscosity and K is any of the elastic anisotropy constants of the liquid crystal:

$$[K] = \frac{L}{T^2} \qquad [\gamma] = \frac{1}{T},$$

with [52]:

$$K \sim 3.4 \times 10^{-7} \frac{cm}{s^2} \qquad \gamma \sim 1.9 \frac{1}{s},$$

then $K/\gamma^2 \sim 3\mu m$.

Experimentally, the standard width used for the waist of the light beam ($250\mu m$) is 50 times larger that the length associated with the elastic constant ($5\mu m$), that is, in our dimensionless units $\omega = 50$. Then, below the Fréedericksz transition, Rayleigh vortices accounts for the umbilical defects.

To explain the origin of the Rayleigh vortex, we note that the liquid crystal light valve is a thin film and thus one should consider averaged quantities. The voltage averaged over the thickness $\langle V(r_\perp)\rangle$ takes the form:

$$\langle V(r_\perp)\rangle = \frac{1}{\mathrm{d}} \int_0^{\mathrm{d}} V(z, r_\perp)\mathrm{d}z = \frac{V_0 + \alpha I(r_\perp)}{2}.$$

Likewise, calculating the electric field averaged in the vertical direction, we obtain $\langle E(r_\perp, \phi)\rangle = -\nabla_{r_\perp}\langle V\rangle = \alpha I_0(r_\perp/2\omega^2)\mathrm{e}^{-r_\perp^2/\omega^2}\mathrm{e}^{\mathrm{i}\phi}$, where the electric field is represented in complex variable notation. Therefore, the Rayleigh vortex is proportional to the averaged electric field or, equivalently the gradient of the averaged potential $A_R(r_\perp, \phi) = 4b\langle E\rangle/\alpha = -4b\nabla_\perp\langle V\rangle/\alpha$.

Then the external forcing giving by the external electric field is resposible for inducing a matter vortex with positive charge at the center position where the applied Gaussian beam is peaked, this is the origin of the self-stabilization mechanism for the vortex induction.

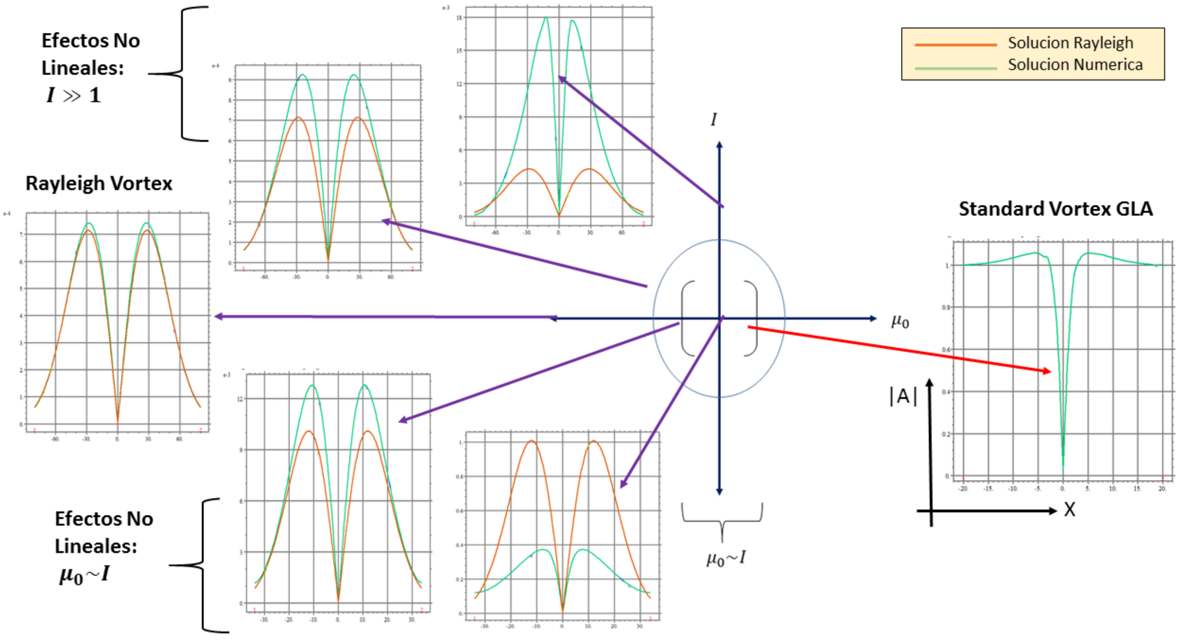

Figure 4.4: Numerical comparison of the Rayleigh solution and the vortices obtained from equation (4.1) in the I vs μ_0 space parameter

4.3 Cubic Approximation

In the limit when $\omega \gg 1$ but I is not necessarily small, the cubic term in equation (4.1) can not longer be neglected, and in the stationary case equation (4.2) becomes:

$$(\mu_0 + \beta \mathrm{e}^{-\rho^2})A - |A|^2 A + \frac{\mu_1}{\omega}\rho \mathrm{e}^{-\rho^2}\mathrm{e}^{\mathrm{i}\theta} = 0. \tag{4.4}$$

Looking for vortex solutions $A(r,\theta) = R(r)\mathrm{e}^{\mathrm{i}\theta}$ and defining $\mu(\rho) = (\mu_0 + \beta \mathrm{e}^{-\rho^2})$ and $f(\rho) = \frac{\mu_1}{\omega}\rho \mathrm{e}^{-\rho^2}$, the amplitude of the vortex solution R satifies:

$$R^3 - \mu R - f = 0. \tag{4.5}$$

This is a *depressed cubic equation* and can be solved following the **Cardano formula**:

$$R = \sqrt[3]{\frac{f}{2} + \sqrt{\frac{f^2}{4} - \frac{\mu^3}{27}}} + \sqrt[3]{\frac{f}{2} - \sqrt{\frac{f^2}{4} - \frac{\mu^3}{27}}}. \tag{4.6}$$

Figure 4.5 shows the amplitude profile in this *cubic* approximation.

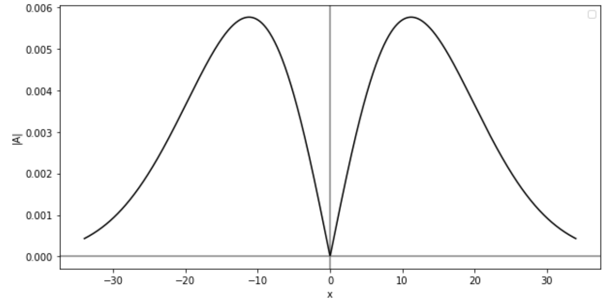

Figure 4.5: Amplitude profiele of vortex solution in the cubic approximation

In the limit $\omega \gg 1$ and $I \ll 1$, this solutions coincides with the Rayleigh vortex solution discused in Section [4.2], and numerical simulations shows that this new approximated solution accounts for the nonlinear effects when $I \ll 1$.

Then, the **Cubic or Cardano** vortex is an even better approximation of the topologically driven Ginzburg-Landau vortex than the Rayleigh vortex with drawback of being less manipulable analytically.

4.4 Bifurcation Diagrams

In this section, we study the bifurcations diagrams found by simulating numerically equation (4.1) in the space of parameters $\{\omega, \mu\}$ and $\{I, \mu\}$.

We will name the different regions showed in the figures 4.6 and 4.7 simply by *yellow region*, *pink region*, *blue region*, *green region* and *red region*:

1. **Yellow region:** In this region, the solution is given by the Rayleigh vortex.
2. **Pink region:** In this region, the solution is given by the Cubic Vortex given by formula (4.6).
3. **Blue region:** In this region, the effect of the spactial derivatives can not be negleted and the Raylegh approximation ceases to be valid.
4. **Green Region:** In this region, the system is above the Fréedericksz transition, and the core of the vortex solution is given by the intrisic parameters of the system.
5. **Red Region:** In this region, the solution correponds to the Standard Vortex of the Ginzburg Landau equation studied in Chapter 3.

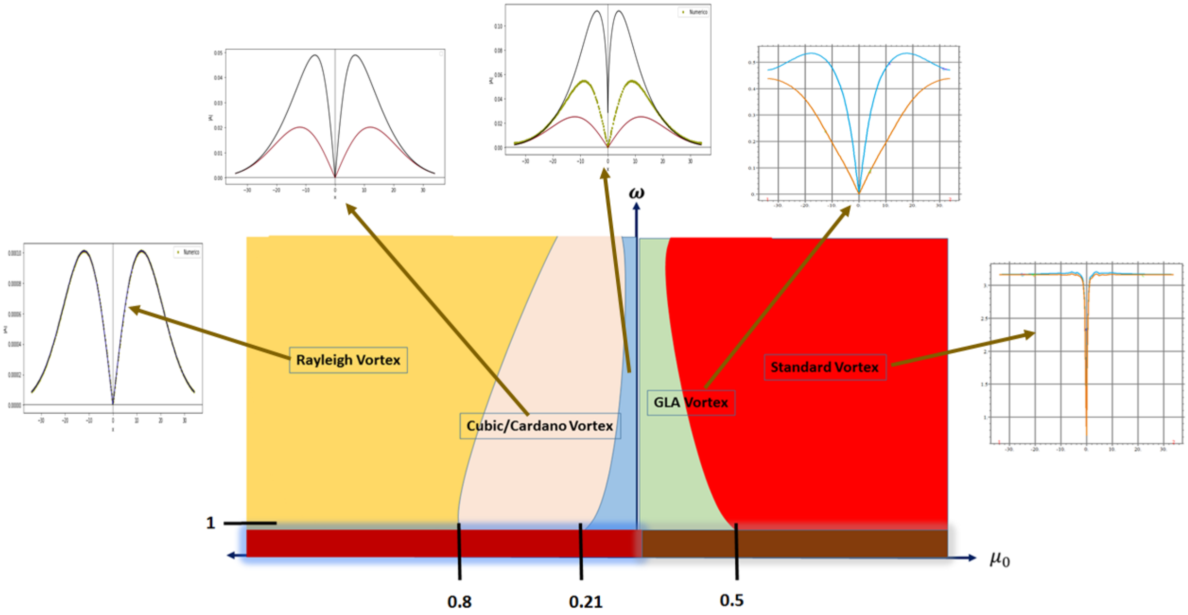

Figure 4.6: Bifuraction Diagram μ vs ω

Remark In the regime $\omega \ll 1$, numerical simulations breakdown since this region is under the charactheristic scale of the equation.

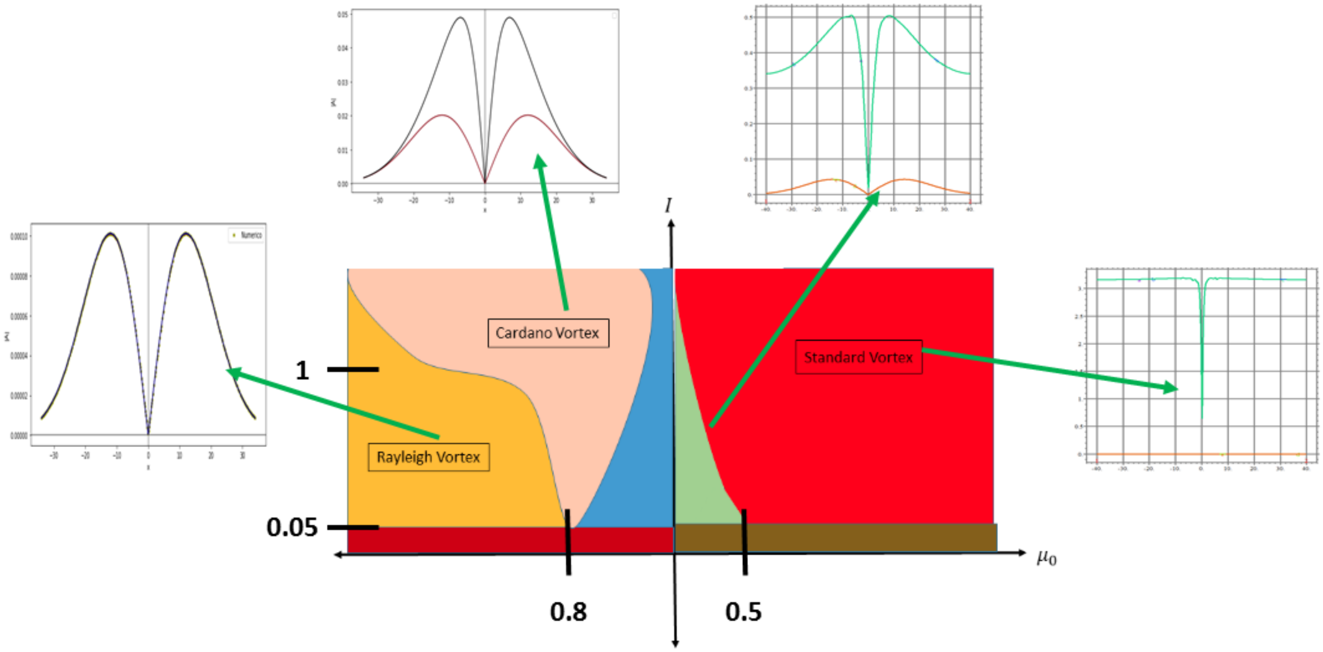

Figure 4.7: Bifuraction Diagram μ vs I

4.5 Standard vortex solution

When the system is above the molecular reorientational transition ($\mu > 0$), the elastic couplings (taking into account in (4.1) by the Laplacian and the second-order differential operator describing anisotropic space variation with $\delta \neq 0$) determines the vortex core size, which is now of the order of few microns.

In this regime, the Rayleigh vortex solution does not account for the observed vortice, and the solution of the system is given by a slightly deformation of the Standard Vortex solution (Chapter 3) of the Ginzburg Landau equation.

Considering the amplitude equation (4.1) as in [48]:

$$\partial_t A = \mu A + \nabla^2 A + \delta \partial_{\eta\eta} \bar{A} - A|A|^2 + bI' \mathrm{e}^{\mathrm{i}(\theta+\theta_0)} \tag{4.7}$$

The forcing induces a single vortex along with the preferred direction for the phase jump θ_0. This phase jump may or may not coincide with the phase jump preferred by the anisotropy (which depends only in the sign of δ).

When these two effects do not agree, numerical simulations and experimental observations [14, 15, 48] have shown that the vortex starts to turn in order to align its phase jump close to the center with the preferred value for the anisotropy, but mantaining the phase jump imposed by the forcing in the border of the illuminated area. This phenomenon gives rises to a vortex with swirling arms as a stationary state. Figure 4.8 shows numerical and experimental observations of this solution:

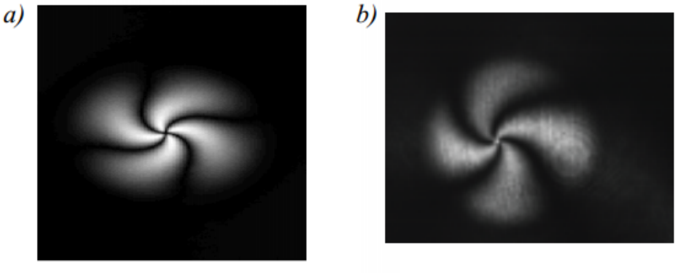

Figure 4.8: a) Numerical simulation of a vortex with swirling arms, b) Experimental observations [48]

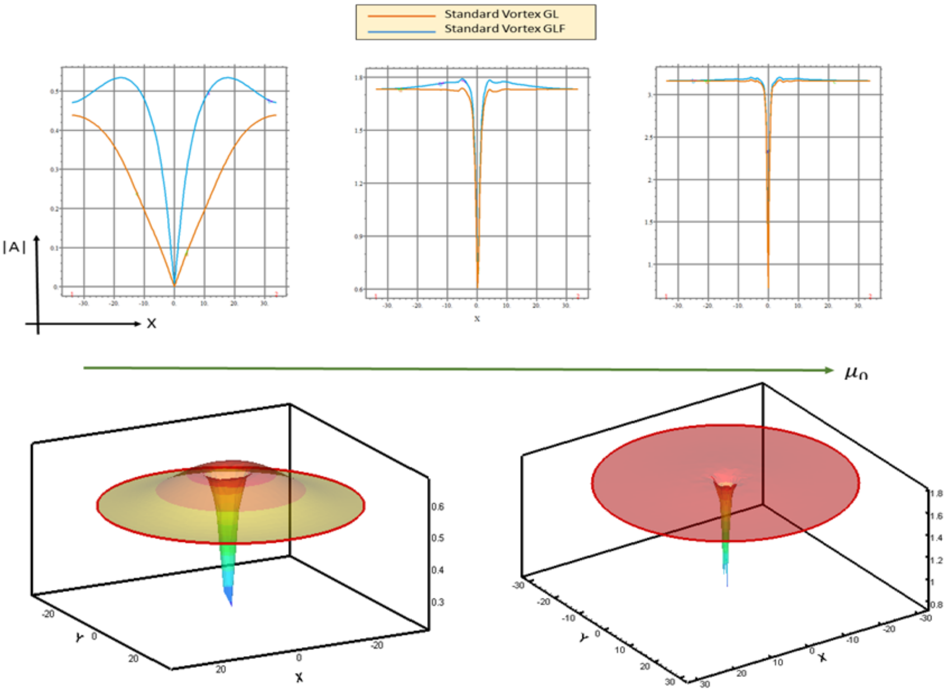

Figure 4.9: Profile and surface plot of the solution for $\mu > 0$ as μ increases

Remark This solution converges monotocally to $\sqrt{\mu}$ as $r \to \infty$.

4.6 Vortex Lattice

Generalizing the previous analysis one can consider two light beams illuminating the optical light valve in different positions (r_1 and r_2). The averaged potential $\langle V(r_\perp)\rangle = (V_0 + \alpha I(x,y,r_1) + \alpha I(x,y,r_2))/2$, where $I(x,y,r_i)$ is a Gaussian beam centered at r_i, corresponds to a surface with two mounds. Since the equilibrium amplitude is the gradient of the averaged potential we identify maxima or minima of the potential with positively charged vortices and the saddle points with vortices of negative charged. Figure 4.9 illustrates this in the case of two Gaussian beams. Note that a negative vortex is located between the positive vortices. By decreasing the distance between the centers of the Gaussian, the charges approach each other. When this distance is of the order of the beam waist, the vortices merge, leaving a single vortex of a positive charge.

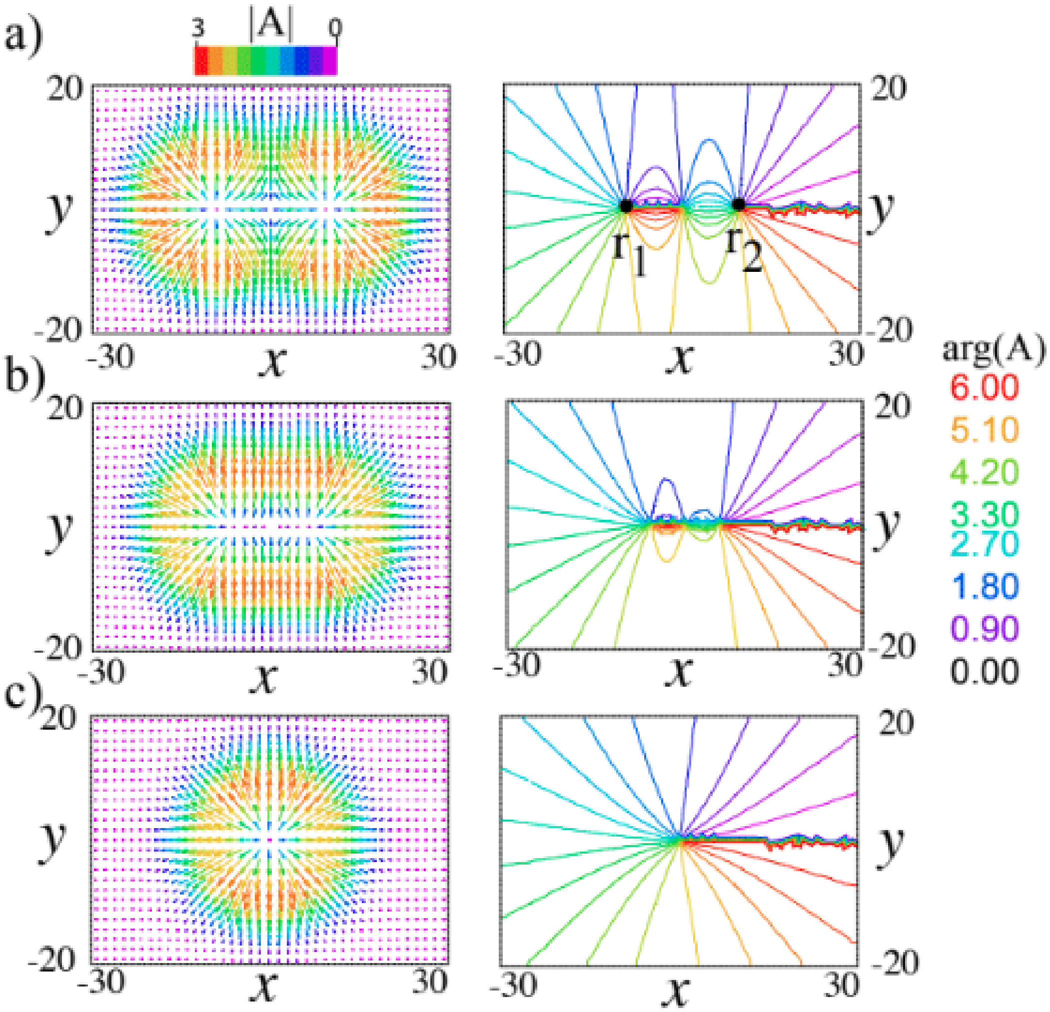

Figure 4.10: Analitycal vortices solutions induced by two Gaussians using equation 4.1 with two forcing terms. The total topological charge is $N = 1$. The complex amplitude A was obtained using formula $A = -4b\nabla_{r_\perp}\langle V\rangle/\alpha$. The left panels correspond to the vector representation of the complex amplitude. The colors account for the magnitude of the amplitude. The contour plot of the phase of the amplitude is shown on the left panel.

This can also be shown considering the superposition of two Rayleigh vortices nested in noncoaxial Gaussian beams. Assuming the vortices are located along the x axis and separated symmetrically from the origin a distance a. The superposition of such beams can be written as

$$v(x,y) = v_1(x,y) + v_2(x,y),$$

with

$$v_1(x,y) = \begin{pmatrix} -(x-a)\mathrm{e}^{-[(x-a)^2+y^2]/\omega^2} \\ -y\mathrm{e}^{-[(x-a)^2+y^2]/\omega^2} \end{pmatrix},$$

$$v_2(x.y) = \begin{pmatrix} -(x+a)\mathrm{e}^{-[(x+a)^2+y^2]/\omega^2} \\ -y\mathrm{e}^{-[(x+a)^2+y^2]/\omega^2} \end{pmatrix},$$

One finds that all the existing vortices are located on the $y = 0$ axis, and their x coordinates satisfy:

$$\frac{x}{a} = \tanh(2xa).$$

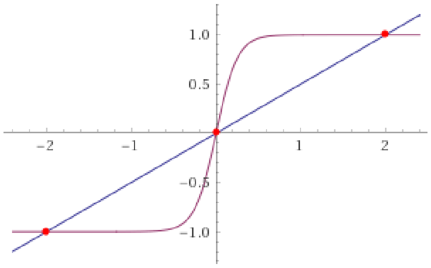

Figure 4.11: Single vortices presented in the superposition $v(x,y)$

When the initial separation between the individual beams reaches the critical value $a = a_c = 1/\sqrt{2}$ the number of existing vortices changes. Below a_c, the total field contains only one vortex. This case can be understood physically since there is a strong superposition between rays of light. Such vortex has positive charge and is located at the origin. Beyond the critical separation, the two existing single-charge vortices with positive charge are expelled toward both sides of the origin, at which a negatively charged vortex remains. This vortex with negative charge is always present, so the net topological charge of the superposition of the two charges +1 vortices is always +1. Indeed, expanding $v(x,y)$ in Taylor series around $(0,0)$:

$$v(x,y) \approx \begin{pmatrix} -x + \frac{2a^2x}{\omega^2} \\ -y \end{pmatrix}.$$

Taking $a = \omega$ shows, explicitely a vortex of topological charge -1 at the origin:

$$v(x,y) = \begin{pmatrix} x \\ -y \end{pmatrix} = r\mathrm{e}^{-\mathrm{i}\theta}.$$

But when the individual vortices are separated by several beam widths ($a \gg \omega$), the negatively charged vortex is hidden in the dark region surrounding the individual beams, where the field amplitude is exponentially small. Thus the presence of this negative charged vortex might be difficult to detect by experimental means like the polarimetry technique.

Numerical simulations of equation (4.1) with forcing term consisting of a superposition of Gaussians equivalent to illuminating the optical valve with several light beams give vortex lattices as a stable equilibria. The middle pannels in Figure 4.8 show the typical lattices. Circles account for the waist of the Gaussian forcing. When the liquid crystal light valve is forced with a single beam of sufficiently intense light, it always induces a vortex of positive charge at the center of the beam. This result is easily understood as a consequence of the voltage induced by a single ray being an electric field with a positively charged vortex. Figure 4.8 shows the vortices induced by a green laser.

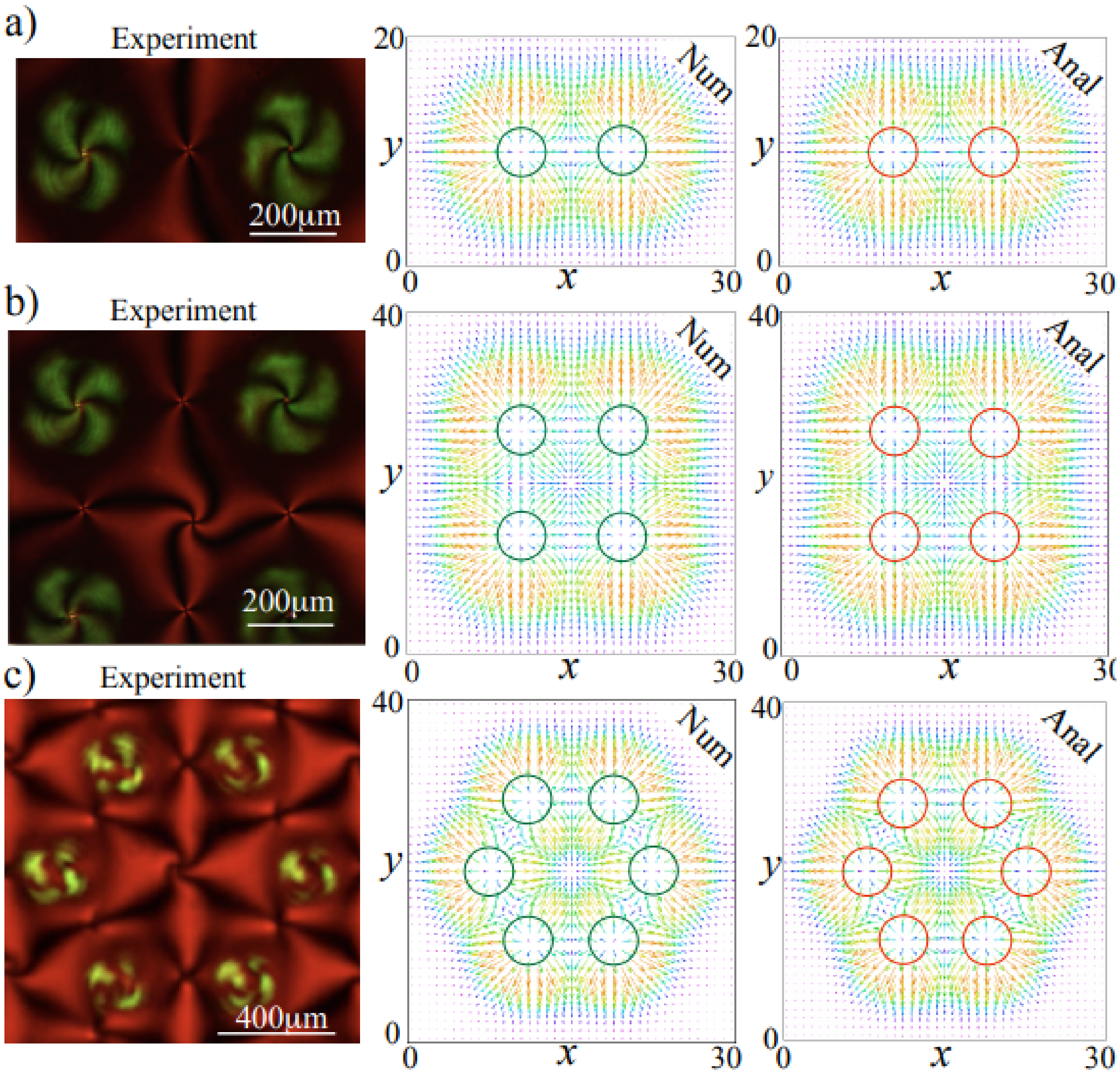

Figure 4.12: Numerical Vortex Lattices forced with two, four, and six rays of light.

An excellent agreement is observed with the vortex lattices obtained by numerical simulations of the topologically driven Ginzburg Landau equation (4.1). Liwewise, there is excellent agreement with the experimental observations. However, due to the anisotropic effects that are not accounted for in the Rayleigh vortex approximation, the experimental positive vortices exhibit swirling arms discused in Section [4.5]. Note that in the case of four light beams, the averaged potential has four saddle points on the side of a square formed by the maxima and a minimun on the intersection of the diagonals. This explains why in the experiment a swirling vortex is induced on the diagonal between the topologically forced vortices.

The existence of a +1 vortex at the origin in configurations with +1 vortices placed at the vertices of any $2n$-sized regular polygon with $n \geq 2$, can also be shown following simple steps.

Taking $\vec{v}(x, y) = \sum_{\mathrm{i}=1}^{4} v_{\mathrm{i}}$ the superposition of 4 vortices in the square configuration of Figure 4.12

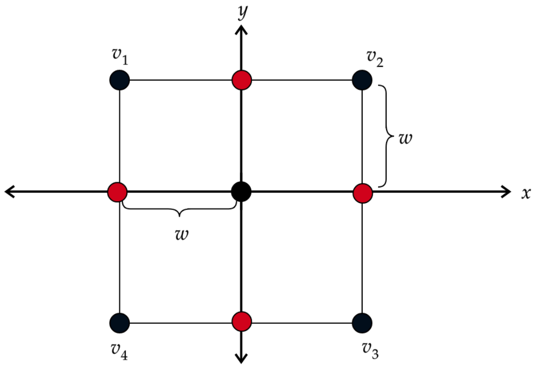

Figure 4.13: Square configuration: black dots acounts for +1 charges, while red for −1 charges

Then for the x coordinate:

$$\begin{aligned} v_x = \sum_{\mathrm{i}=1}^{4} (v_{\mathrm{i}})_x &= (x+\omega)\mathrm{e}^{-x_+ + y_+} + (x-\omega)\mathrm{e}^{-x_- - y_-} \\ &\quad + (x+\omega)\mathrm{e}^{-x_+ - y_-} + (x-\omega)\mathrm{e}^{-x_- - y_-}, \end{aligned}$$

where $x_\pm$ and $y_\pm$ denotes the following quantities:

$$x_\pm = \left(\frac{x \pm \omega}{\omega}\right)^2 \qquad y_\pm = \left(\frac{y \pm \omega}{\omega}\right)^2.$$

Expanding in Taylor series around the origin gives:

$$\begin{aligned}\sum_{\mathrm{i}=1}^{4}(v_{\mathrm{i}})_x &\approx \omega-\frac{\omega}{2}(x_+ + y_+)-\omega+\frac{\omega}{2}(x_- + y_-)\\ &\quad +\omega-\frac{\omega}{2}(x_+ + y_-)+\omega+\frac{\omega}{2}(x_- + y_+)\\ &\approx \omega(x_+ - x_-)\\ &\approx 4x.\end{aligned}$$

Similarly, in the y component expansion gives $v_y \approx 4y$. This implies that locally around the origin the field follows a $+1$ vortex configuration.

In conclusion, we have been able to establish analytically the origin of the vortex lattices observed in illuminated liquid crystal layers with photosensitive walls below the Fréedericks transition. In the regime where the Rayleigh vortex does not account for the observed vortices, the position and configuration of the vortex lattices are qualitatively described by the lattices of the Rayleigh vortices. The amplitude equation describe qualitatively and quantitatively the dynamics near the instability point.

At the onset of the Fréedericksz transition, depending on the light intensity, the vortices positioned in the center of the light beam can undergo instabilities and move to dark areas (the area outside the illuminated region). Thesse new topological defects known as *shadow vortices* [53, 54] are characterized by having an exponetially small height. Experimentally they are detected indirectly. The lattice created by these and the induced vortices is a problem currently in progress. These are all the topological solutions in the one-dimensional model giving by equation (4.8).

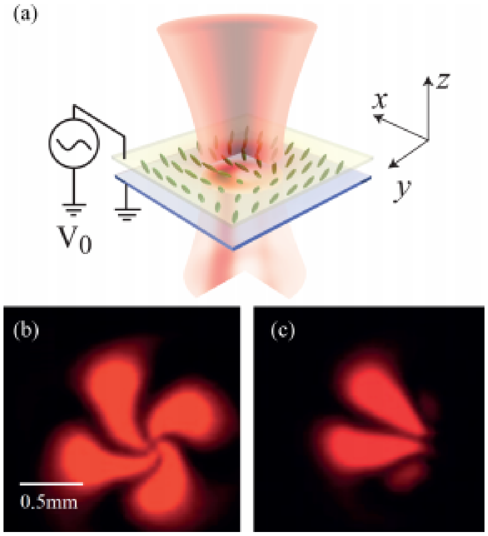

Figure 4.14: (a)Schematic setup for vortex induction. (b), (c) Intensity profile measured using linear crossed polarizers for a large ($V_0 = 18V$) and a small ($V_0 = 17V$) voltage, respectively. The presence of a shadow vortex is revealed in (c) by the lines of zero intensity intersecting at the boundaries of the illuminated region. After [53]

4.7 One-dimensional scalar model

To shed lthe dynamics of phase singularities, we can consider the equivalent equation in one dimension [53, 55]

$$\partial_t u = (\mu_0 + \beta \mathrm{e}^{-x^2/\omega^2})u - u^3 + \partial_{xx} u + \alpha x \mathrm{e}^{-x^2/\omega^2}, \tag{4.8}$$

where $u(x,t)$ is a one-dimensional order parameter, $\mu_0 < 0$ is a control parameter, β stands for the intensity of the inhomogeneous linear parameter and satisfies $\beta + \mu_0 > 0$, ω is the width of the Gaussian, and α is the intensity of the forcing. For $\beta = \alpha = 0$, the previous model corresponds to the real Ginzburg-Landau equation or the overdamped ϕ^4 model [56]. Topologically non trivial solutions of (4.6) are kink (and they corresponds to the equivalent of vortex solution in Eq. (4.1)). When the kinks are spatially monotone increasing (decreasing), they are positively (negatively) charged. The innhomegeneous linear term (proportional to β) causes the kink to move in the direction of its gradient. On the other hand, the forcing term (proportional to α) tends to generate a kink that is positioned at the origin. Then, the superposition of these two terms-when α is large enough-must generate a kink that is positioned at the origin, i.e, **standard kink**.

When α decreased and exceeds a critical value, the standard kink becomes unstable and begins to move to the region where the linear parameter $\mu(x)$ is negative and is finally positioned in the corner region, this corresponds to the **shadow kink** [53, 55]. If the limit $\omega \gg 1$ is taking into account in the region $\mu(x) < 0$, it is possible to find an analytical solution $u \sim -\frac{\alpha x \mathrm{e}^{-x^2/\omega^2}}{\mu_0}$ that is called the **Rayleigh kink**. These are all the topological solutions that exists in the model giving by equation (4.8).

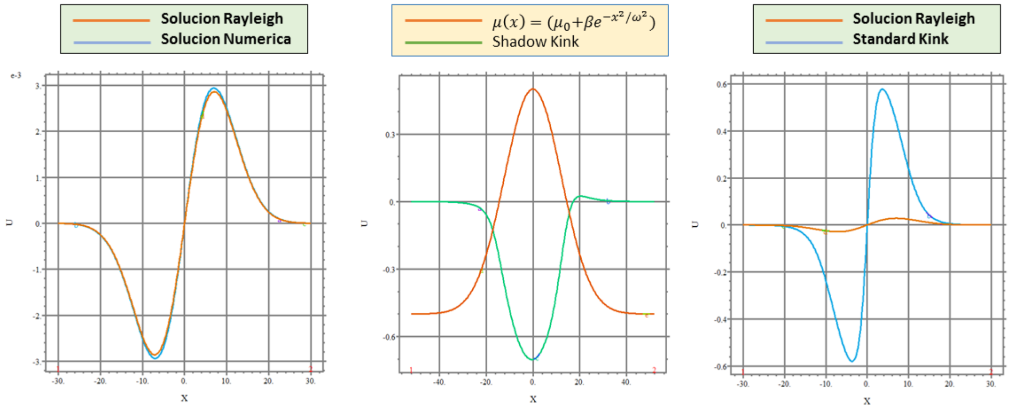

$\mu < 0$ $\mu \sim 0$ $\mu > 0$

Figure 4.15: One dimensional topological equilibria

The case when $\mu_0 > 0$ and $\alpha = \beta = 0$ was briefly in Section [2.3], in this scenario (4.8) reduces to

$$\partial_t u = \mu_0 u - u^3 + \partial_{xx} u.$$

In this equation there are two symmetrical homogeneous solutions, $u = \sqrt{\mu_0}$ and $u = -\sqrt{\mu_0}$, these solutions are both stable and have the same energy.

Moreover, because of initial condition or fluctuations these two solutions can exist in different locations in the system simultaneously, these different locations are called **domains**. When this happens the two solutions are connected in a smooth way through a *kink solution*, $u = \sqrt{\mu_0} \tanh x \sqrt{\mu_0/2}$ which is shown in Figure 4.16. Due to the symmetry $u \to -u$, the analogous *Antikink* also exist $u = -\sqrt{\mu_0} \tanh x \sqrt{\mu_0/2}$. If more than one kink (or antikink) exists in the system, they will atract if they are of different charge or repel if they have the same charge, in order to minimize the total free energy. Then, when two kinks of different type collide they annihilate leaving a homogeneous solution in the system as a global energy minimum.

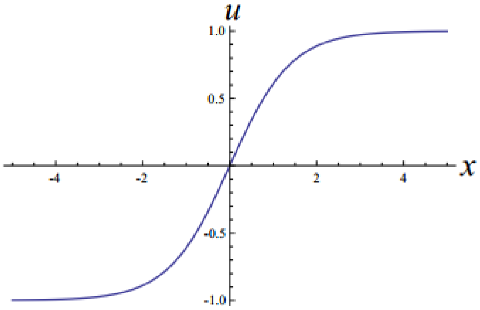

Figure 4.16: Kink solution with $\mu_0 = 1$. This state connects the solutions $u = \sqrt{\mu_0}$ and $u = \sqrt{\mu_0}$

Experimentally, kink solutions connecting spatially modulated states on one-dimensional fluidized granular layers have been reported [57]

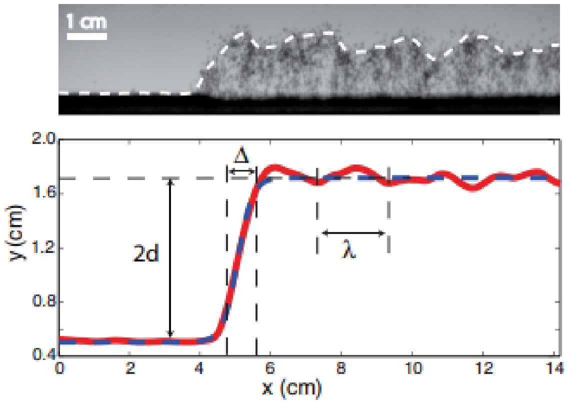

Figure 4.17: Top: Typical image of a granular kink. Bottom: Granular kink averaged over 1000 frames, d stands for the granular kink height with respect to middle plane and Δ stands for the typical core size of the kink. [57]

4.8 Numerical Results in the one-dimensional model

The Rayleigh kink solution is an excellent approximation for the one-dimensional model (4.8). Figure 4.18 shows a comparison between numerical solutions of equation (4.8) and the approximation $u = -\frac{\alpha x \mathrm{e}^{-x^2/\omega^2}}{\mu_0}$, we can observe the form of the numerical solution as the effect of the neglected term becomes noticiable.

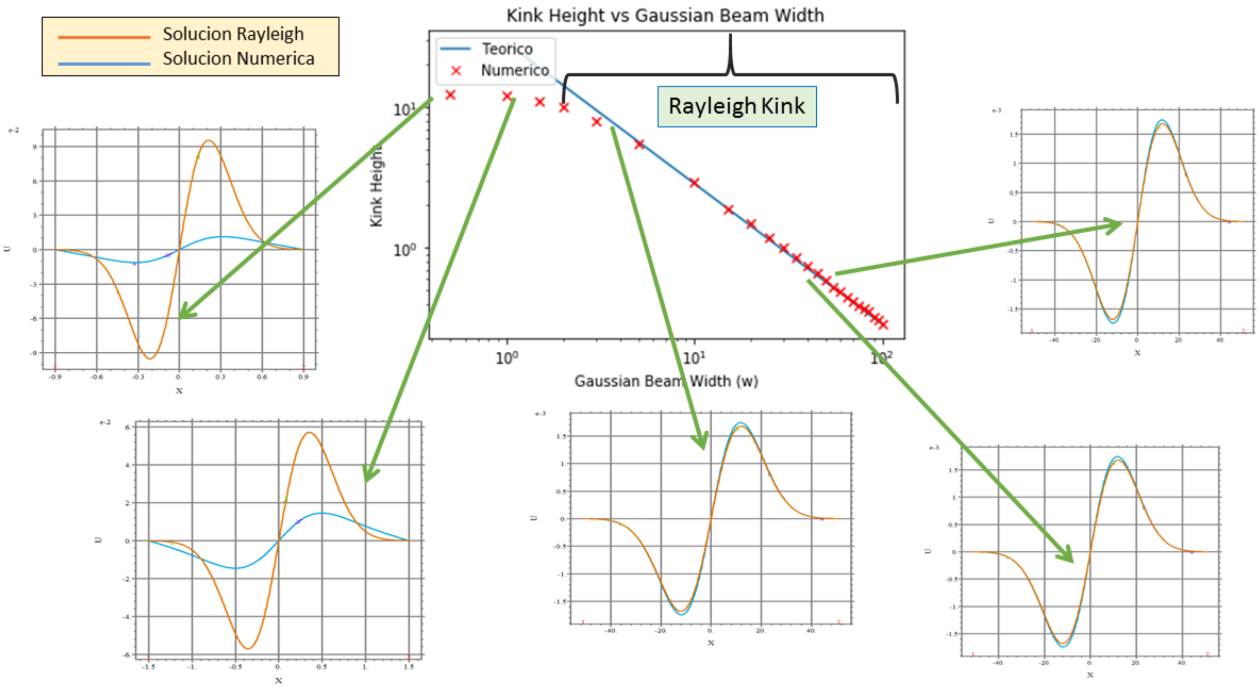

Figure 4.18: Numerical comparison of the Rayleigh kink solution and the kinks obtained from equation (4.8)

One-dimensional parallel of the vortex lattice discused in Section [4.5] correspond to periodic solutions of equation (4.8) with n forcing terms centered at points x_{i}, $\mathrm{i} = 1, \ldots, n$

$$\partial_t u = (\mu_0 + \beta \mathrm{e}^{-x^2/\omega^2})u - u^3 + \partial_{xx} u + \sum_{\mathrm{i}=1}^{n} \alpha(x - x_{\mathrm{i}})\mathrm{e}^{-(x-x_{\mathrm{i}})^2/\omega^2}. \tag{4.9}$$

With points x_{i} equidistant i.e. $|x_{\mathrm{i}} - x_{\mathrm{i}+1}| = \lambda$, $\forall \mathrm{i}$. Since actually there exists a critical distance λ_c such that the number of existing kinks changes (c.f. Section [4.5]), as long as the distance between the forcings exceed the critical distance the equilibrium solution will exhibit pairs kink-antikink.

Figure 4.19 shows the periodic solutions of equation (4.9) in the case $n = 2$ for different values of the control parameter μ. (In blue numerical solution of equation (4.9) and in yellow Rayleigh approximation superposition)

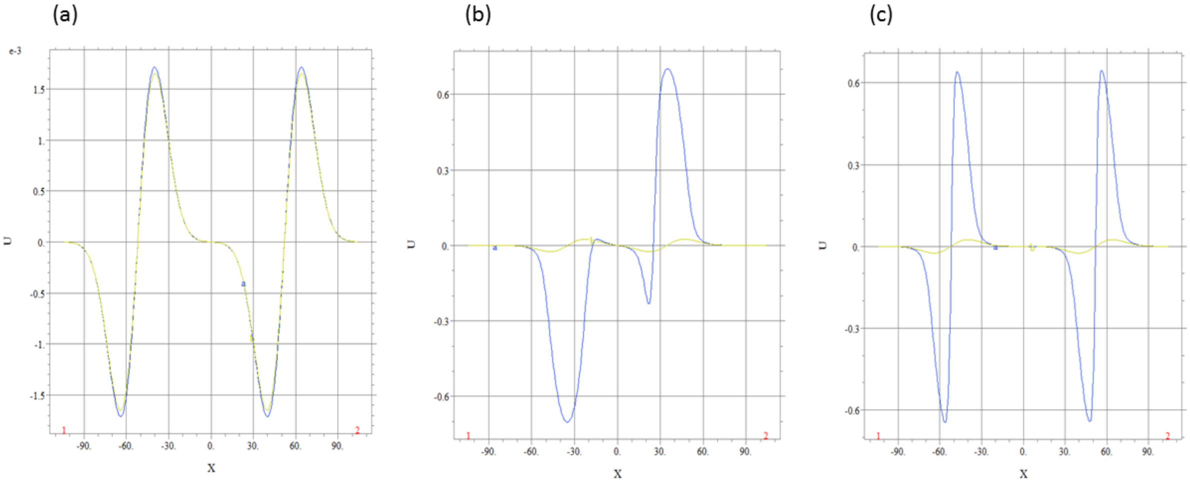

$\mu < 0$ $\mu \sim 0$ $\mu > 0$

Figure 4.19: Periodic solutions of equation (4.9) for different signs of the control parameter

Particularly interesting for future research is the case when $\mu \sim 0$ since standard kinks appears connected through pairs of shadow kinks/antikinks.

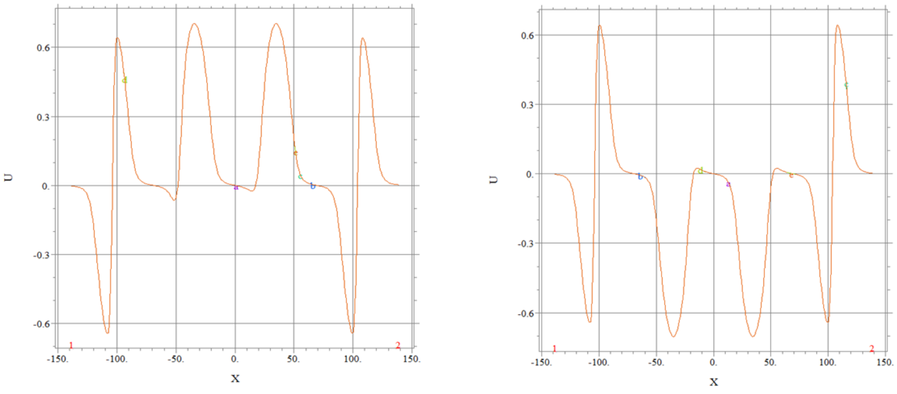

Figure 4.20: Standard kinks connected through shadow kinks obtained in numerical simulations

We conjecture that the emergence of these kind of solutions is due to shadow kinks pairs decrease the total energy, but this is yet to be confirmed through rigorous methods since interaction shadow-standard kink is not fully understand.

Chapter 5

Topological Magnetic Forcing

5.1 Generation of umbilics by inhomogeneuos magnetic fields

As discussed in the previous chapters, optical vortices can be derived directly from induced umbilical defects in Liquid Crystal textures. Indeed, an umbilical defect is one that naturally possesses a vortex-like morphology, making it attractive for spontaneously enabling the matter template to impress a helical structure on an incoming light wavefront. Nonetheless, major problems arise when practical implementations are aimed at, because soft-matter defects are dissipative structures that obey a complex Ginzburg-Landau equation (CGLE) and undergo a coarsenig dynamics ruled by their mutual interaction and annihilation. Therefore, they are unstable, usually limited to a single defect pair per sample or a defect-free sample, and without the possibility of controlled addressing.

In [58] Pieranski presents a method of controlled generation of umbilics by means of magnetic fields of appropiate geometry applied temporarily before, during or after the Freederick's transition. Therefore,magnets are used to control the initial conditions where the vortices were positioned. The induction is achieved by the use of a cylindrical magnet oriented with is symmetry axis along the $\vec{n}_0 \parallel z$ direction. But this approach have a lot of significant disadvantages that prevents the true creation and pinning of matter vortices in the nematic sample, since the magnets are applied for 5 minutes and then removed resulting in a transient induction of defects as the system relaxes after the removal of the magnet and the simultaneous application of a electric field $E > E_c$ is not enough to sustain a permanent vortex.

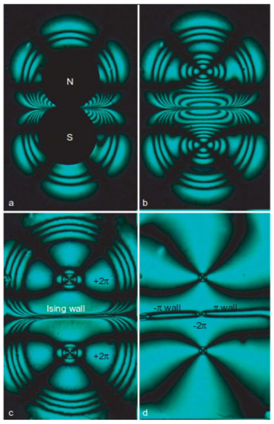

Figure 5.1: Generation of a -2π umbilic by a system of antiparallel magnets: (a), (b) final state of the distortion in the presence of magnets; (c), (d) relaxation of the distortion after the removal of the magnets. After [58]

5.2 Experimental Setup

Recently, in the Laboratory of robust phenomena in optics (LAFER), a novel and cheap method for robust vortex induction has been designed, this approach relies on nematic liquid crystal strong interaction with magnetic fields.

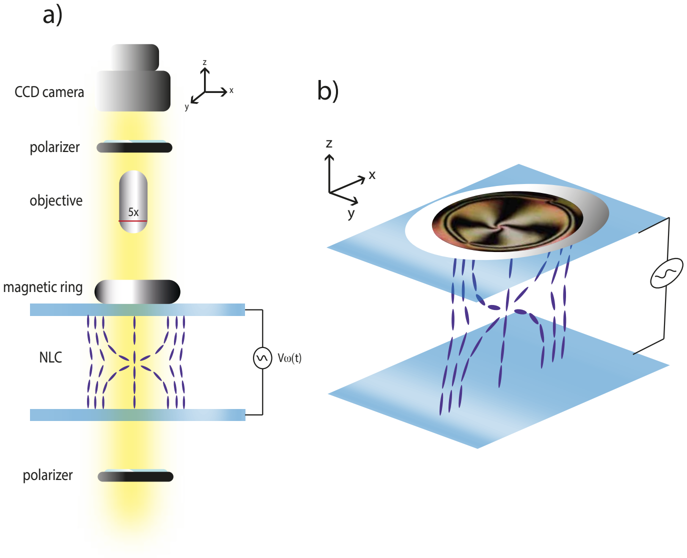

Figure 5.2: Experimental setup. Courtesy of Valezka Zambra

We consider a liquid crystal cell with thickness d= $0.75\mu m$ sandwiched between two glass plates which have been chemical treated for hometropic anchoring and equipped with indium tin oxide (ITO) electrodes, the cell is filled, by capilarity, with the nematic liquid crystal MLC-6608(Merck). On top of nematic liquid crystal cell a neodymium magnetic ring 14x5 mm was placed. The system is located betweeen linear crossed polarizers of a Olympus Bx51 microscope. A sinusoidal voltage with 100 Hz frequency is applied to the sample, and the experimental images are captured by a MODELO ThorLabs CCD camera

The employed LC has negative magnetic and dielectric anisotropy, $\chi_a = \chi_\parallel - \chi_\perp$ ($\varepsilon_a = \varepsilon_\parallel - \varepsilon_\perp$), with $\chi_\parallel$ and $\chi_\perp$ the magnetic (dielectric) susceptibility for the magnetic(electric) fields parallel and orthogonal, respectively, to the molecular director.
In its ground state withoud external fields, the director $\vec{n}$ field is homogeneous and the sample has the axial symmetry around the z-axis.

Owing to the magnetic anisotropy $\chi_a = \chi_\parallel - \chi_\perp$ of the diamagnetic susceptibility of the nematic phase, the magnetic field $\vec{B}$ applied to the sample exerts the torque:

$$\Gamma_m = \frac{\chi_a}{\mu_0}(\vec{n} \cdot \vec{B})(\vec{n} \times \vec{B}) \approx \frac{\chi_a}{\mu_0} B_z (\vec{n} \times \vec{B}), \tag{5.1}$$

on the director and tilts it out from its initial orientation. The new orientation results form the balance between the magnetic torque and the restoring elastic torque.

When a bias V_0 is applied to the LCLV beyond the Fréederickzs transition voltage V_{FT}, the molecules tend to reorient perpendicularly to the (low frequency) electric field because of the negative ε_a ; hence, since $\vec{E} = V_s/\mathrm{d}\hat{z}$ is applied along the longitudinal z direction and the 2π azimuthal degeneracy imposes rotational invariance around it, the LC molecules can arbitrarily align in any direction, spontaneously forming spatial domains separated by walls, loops, and umbilic defects or vortices [3]. In the present experiment, we keep $V_0 \lesssim V_{FT}$ in order to avoid the spontaneous reorientation while bringing the molecules close to the transition point. When a magnetic field is applied onto the sample: the Fréedericskz threshold is locally overcome and the molecules start reorienting, following the gradient associated with magnetic field profile.

5.3 Experimental Observations

Experimentally we observe the existence of a stable vortex triplet composed by a positive vortex at the center of the magnet and two vortices of opposite charge at the boundaries. This is given by the topological conditions, since the net topological charge imposed by such a magnet ring is +1.

Figure 5.3: Vortex triplet induced by a magnet ring. Courtesy of Valezka Zambra

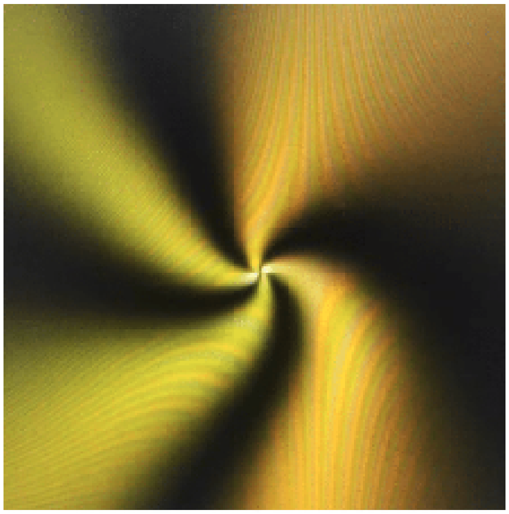

Figure 5.4: Intensity profile of the central vortex measured under white illumination and crossed polarizers. Courtesy of Valezka Zambra

5.4 Theoretical Description

In a first approximation, the magnetic field $\vec{B}$ produced by such a magnet is well described by a dipolar field and can be expressed analytically:

$$\vec{B}(\rho, z) = \left(\frac{\mu_0 m_0}{4\pi}\right)\left\{\left[\frac{3z^2}{(\sqrt{\rho^2+z^2})^5} - \frac{1}{(\rho^2+z^2)^{3/2}}\right]\hat{z} + \frac{3z\rho}{(\rho^2+z^2)^{3/2}}\hat{\rho}\right\}$$

Where m_0 is the polar moment of the magnet and $\rho = \sqrt{x^2+y^2}$.

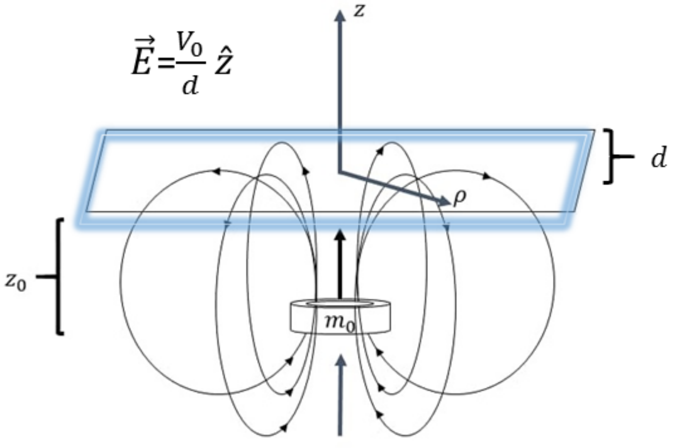

Figure 5.5: Schematic representaion of the magnetic field of a magnet ring

Here we consider the following correction to the Dipolar Magnetic Field:

$$\vec{B}(\rho, z) = B_z\hat{z} + B_\rho\hat{\rho} = \left(\frac{\mu_0 m_0}{4\pi}\right)\left\{\left[\frac{3z^2+\varepsilon}{(\sqrt{\rho^2+z^2})^5} - \frac{1}{(\rho^2+z^2)^{3/2}}\right]\hat{z} + \frac{3z\rho}{(\rho^2+z^2)^{3/2}}\hat{\rho}\right\}$$

where $\varepsilon > 0$ is a phenomenological parameter that accounts for the width of the magnet ring. Figure 5.6 shows the contrast in the magnetic field lines between the dipolar approximation and the proposed correction. Note that correction gives account for the non punctual magnet size in the actual physical experiment.

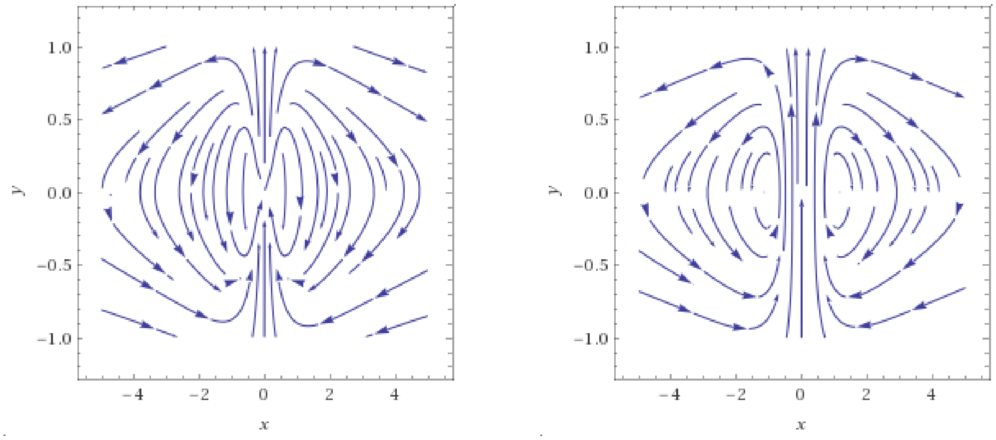

Figure 5.6: Magnetic field lines comparison. Left: Dipolar magnetic field lines. Right: Magnetic field lines in the approximation

The generating field $B(\rho, h)$ in the plane of the sample given by $z = h$ can be calculated in the dipolar approximation and has the radial geometry required for the production of a +1 umbilical defect and its amplitude varies with the distance ρ from the z axis as shown in Figure 5.6. Note that the B_z component of the magnetic field has zeros at $\rho = \sqrt{2}h$. (This is where the B_z component is reversed).

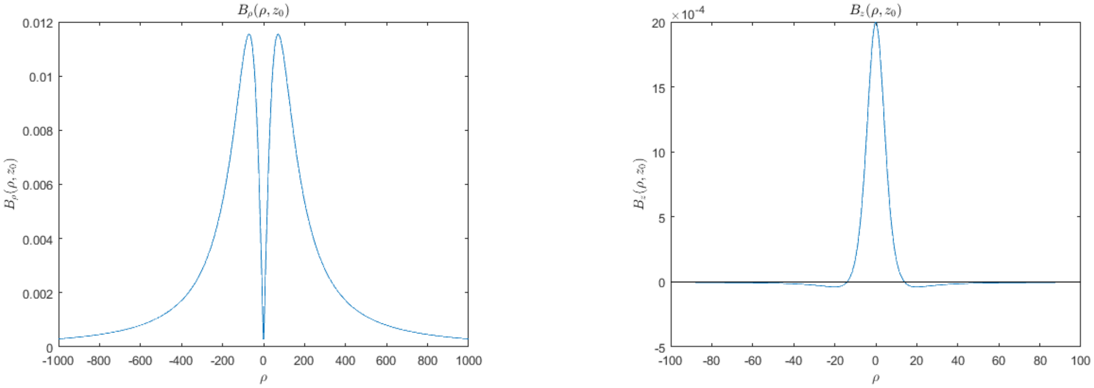

Figure 5.7: Left: Radial component of the magnetic field $B_\rho(h, \rho)$; Right: Vertical component of the magnetic field $B_z(h, \rho)$

Plotting the amplitude of the forcing term in a log-log scale, we observe that follows a power law decay consistent with $A(\rho) \sim 1/\rho^5$ as ρ goes to ∞.(c.f. Figure 5.8). This type of behavior is expected since the forcing decay polynomially. Performing a polynomial fitting on the experimental data (c.f. Figure 5.9) we found a decay exponent close to -4.5, hence our theoretical considerations describes not only qualitatively and also qualitatively the physical situation.

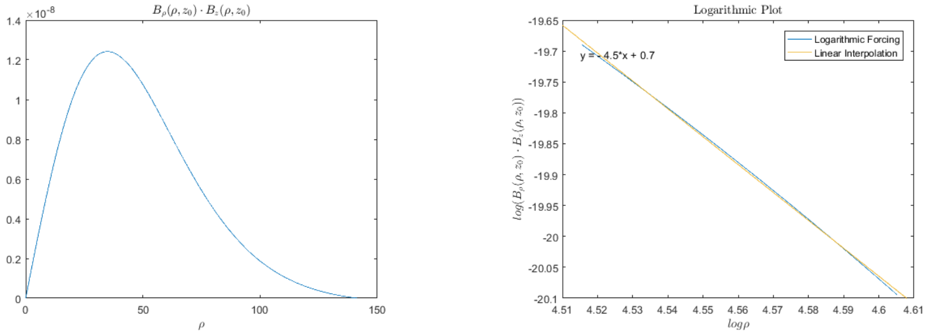

Figure 5.8: Left: Power law decay radial forcing term; Right: Plot in log-log scale

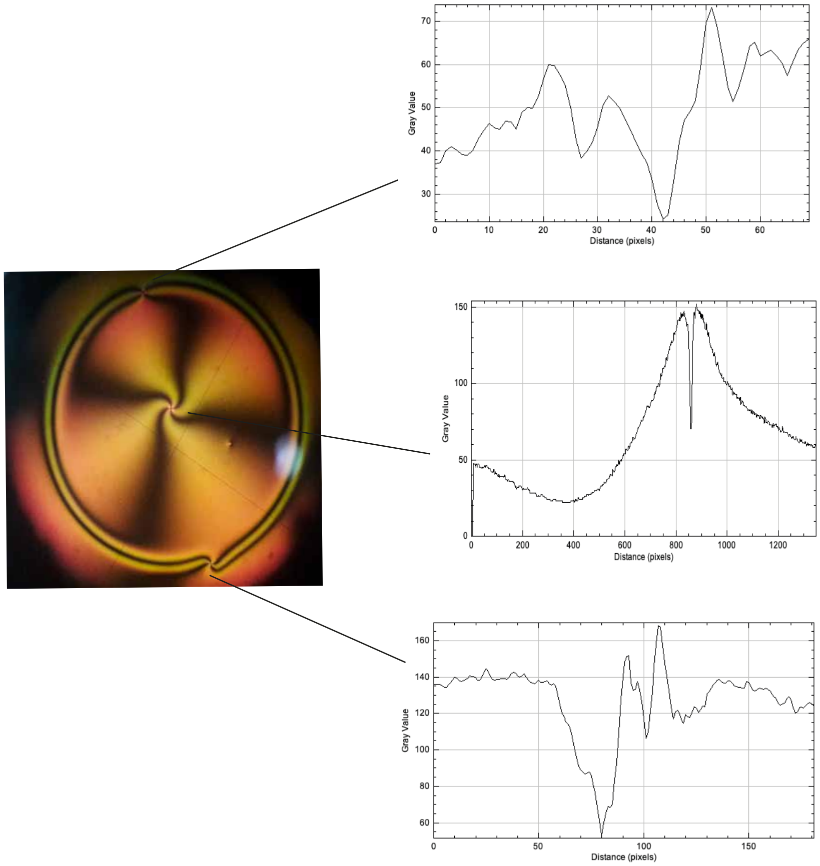

Figure 5.9: Vortex triplet intensity profiles induced by a magnet ring. Courtesy of Valezka Zambra

To describe the mechanism of creation and pinning of this vortices, we derive a model in the vicinity of the Fréedericksz transition, a limit where analytical results are accessible, as nematic LC molecules are weakly tilted from the longitudinal axis $\hat{z}$ and backflow effects can be neglected. The dynamical equation for the molecular director $\vec{n}$ is derived from the Frank-Ossen energy taking into account the contribution of the magnetic field $\vec{B}$:

$$\mathcal{F} = \frac{K_1}{2}(\nabla\cdot\vec{n})^2 + \frac{K_2}{2}(\vec{n}\cdot(\nabla\times\vec{n}))^2 + \frac{K_3}{2}(\vec{n}\times(\nabla\times\vec{n}))^2 - \frac{\varepsilon_a}{2}(\vec{E}\cdot\vec{n})^2 - \frac{\chi_a}{2}(\vec{B}\cdot\vec{n})^2.$$

From the Euler-Lagrange equations associated

$$\frac{\delta\mathcal{R}}{\delta\dot{\vec{n}}} = -\frac{\delta\mathcal{F}}{\delta\vec{n}} \qquad s.a \quad \vec{n}\cdot\vec{n} = 1, \qquad \mathcal{R} = \frac{\gamma}{2}|\vec{n}|^2,$$

the dynamics reads:

$$\begin{aligned}
\gamma\partial_t\vec{n} = \; & K_3 \quad [\nabla^2\vec{n} - \vec{n}(\vec{n}\cdot\nabla^2\vec{n})] + (K_3 - K_1)[\vec{n}(\vec{n}\cdot\nabla)(\nabla\cdot\vec{n} - \nabla(\vec{n}\cdot\nabla))] \\
& + \quad 2(K_2 - K_3)\{(\vec{n}\cdot\nabla\times\vec{n})[\vec{n}(\vec{n}\cdot\nabla\times\vec{n}) - \nabla\times\vec{n}] \\
& + \quad \vec{n}\times\nabla(\vec{n}\cdot\nabla\times\vec{n})\} - \varepsilon_a(\vec{n}\cdot\vec{E}[\vec{E} - \vec{n}(\vec{n}\cdot\vec{E})]) \\
& - \quad \chi_a(\vec{n}\cdot\vec{B}[\vec{B} - \vec{n}(\vec{n}\cdot\vec{B})]),
\end{aligned}$$

where γ is the LC rotational viscosity and $\{K_1, K_2, K_3\}$ are the NLC elastic constants

Under uniform illumination, $\vec{E} = \frac{V}{\mathrm{d}}\hat{z} = E_z\hat{z}$ and close to the transition point, it is possible to suppose that:

$$\vec{n} \approx \left(n_1, n_2, 1 - \frac{n_1^2 + n_2^2}{2}\right),$$

therefore:

$$\begin{aligned}
\gamma\dot{n}_1 = \; & K_3 \quad [\nabla^2 n_1 + n_1((\partial_z n_1)^2 + (\partial_z n_2)^2)] \\
& - \quad (K_3 - K_1)[n_1\partial_{zz}(n_1^2 + n_2^2)/2 + \partial_{xx}n_1 + \partial_{xy}n_2] \\
& + \quad (K_2 - K_3)[-\partial_{xy}n_2 + \partial_{yy}n_1] \\
& - \quad \varepsilon_a n_1 E^2(1 - n_1^2 - n_2^2) - \varepsilon_m n_1 B_z^2(1 - n_1^2 - n_2^2) \\
& - \quad \chi_a[2n_1^2 B_z B_x + 2n_1 n_2 B_z B_x - B_y B_z(1 - n_1^2/2 - n_2^2/2)] \\
\gamma\dot{n}_2 = \; & K_3 \quad [\nabla^2 n_2 + n_2((\partial_z n_1)^2 + (\partial_z n_2)^2)] \\
& - \quad (K_3 - K_1)[n_2\partial_{zz}(n_1^2 + n_2^2)/2 + \partial_{xx}n_1 + \partial_{xy}n_2] \\
& + \quad (K_2 - K_3)[-\partial_{xy}n_2 + \partial_{yy}n_1] \\
& - \quad \varepsilon_a n_2 E^2(1 - n_1^2 - n_2^2) - \varepsilon_m n_2 B_z^2(1 - n_1^2 - n_2^2) \\
& - \quad \chi_a[2n_2^2 B_z B_x + 2n_1 n_2 B_z B_x - B_y B_z(1 - n_1^2/2 - n_2^2/2)].
\end{aligned}$$

Considering the following ansatz for the critical mode:

$$\begin{aligned} n_1 &= X\sin\left(\frac{\pi}{\mathrm{d}}(z-z_0)\right) + W_1 \\ n_2 &= Y\sin\left(\frac{\pi}{\mathrm{d}}(z-z_0)\right) + W_2, \end{aligned}$$

where $\vec{W} = (W_1, W_2)$ stands for higher order corrections. If $k = \pi/\mathrm{d}$ and $z' = z - h$ we obtain:

$$\begin{aligned} \gamma\dot{X}\sin(kz') = \quad & (K_3\partial_{zz} - \varepsilon_a E_z^2 - \chi_a B_z^2)W_1 + K_3\sin(kz')[\nabla_\perp X - k^2X + k^2X(X^2+Y^2)\cos^2(kz')] \\ - \quad & (K_3 - K_1)\sin(kz')[Xk^2(X^2+Y^2)(\cos^2(kz') - \sin^2(kz')) + \partial_{xx}X + \partial_{xy}Y] \\ + \quad & (K_2 - K_3)\sin(kz')[\partial_{yy}X - \partial_{xy}Y] \\ - \quad & \varepsilon_a X\sin(kz')E_z^2(1 - (X^2+Y^2)\sin^2(kz')) \\ - \quad & \chi_a X\sin(kz')B_z^2(1 - (X^2+Y^2)\sin^2(kz')) \\ + \quad & \chi_a B_y B_z - \chi_a\sin^2(kz')[2X^2B_zB_y + 2XYB_zB_x + B_yB_z(X^2+Y^2)/2] \\ \gamma\dot{Y}\sin(kz') = \quad & (K_3\partial_{zz} - \varepsilon_a E_z^2 - \chi_a B_z^2)W_2 + K_3\sin(kz')[\nabla_\perp Y - k^2Y + k^2Y(X^2+Y^2)\cos^2(kz')] \\ - \quad & (K_3 - K_1)\sin(kz')[Yk^2(X^2+Y^2)(\cos^2(kz') - \sin^2(kz')) + \partial_{xx}X + \partial_{xy}Y] \\ + \quad & (K_2 - K_3)\sin(kz')[\partial_{yy}Y - \partial_{xy}X] \\ - \quad & \varepsilon_a Y\sin(kz')E_z^2(1 - (X^2+Y^2)\sin^2(kz')) \\ - \quad & \chi_a Y\sin(kz')B_z^2(1 - (X^2+Y^2)\sin^2(kz')) \\ + \quad & \chi_a B_y B_z - \chi_a\sin^2(kz')[2Y^2B_zB_y + 2XYB_zB_x + B_yB_z(X^2+Y^2)/2]. \end{aligned}$$

The linear operator acting on W is:

$$\mathcal{L} = \begin{pmatrix} K_3\partial_{zz} - \varepsilon_a E^2 - \varepsilon_m B_z^2 & 0 \\ 0 & K_3\partial_{zz} - \varepsilon_a E^2 - \varepsilon_m B_z^2 \end{pmatrix}$$

Defining the inner product $\langle f|g\rangle = \int_{z_0}^{z_0+\mathrm{d}} f\cdot g$ this operator is self-adjoint and its kernel is $K\mathrm{er}\{\mathcal{L}^\dagger\} = \{(\sin(kz'), 0); (0, \sin(kz'))\}$.

Using Fredholm alternative [59] projecting onto the kernel elements of the adjoint operator and considering that $B_z(z, r_\perp)$ and $B_\rho(z, r_\perp)$ are slowly varying as functions of z, then for $\mathrm{d} \ll 1$:

$$\int_{z_0}^{z_0+\mathrm{d}} B_z(z)B_\rho(z)\sin^2\left(\frac{\pi}{\mathrm{d}}(z-z_0)\right)\mathrm{d}z \approx B_z(z_0)B_\rho(z_0)\frac{2\mathrm{d}}{\pi}$$

$$
\begin{aligned}
\gamma\dot{X} = & \quad K_3[\nabla_\perp X - k^2X + k^2X(X^2+Y^2)/4] - (K_3-K_1)[(\partial_{xx}X + \partial_{xy}Y) - Xk^2(X^2+Y^2)/2] \\
- & \quad (K_2-K_3)[\partial_{yy}X - \partial_{xy}Y] \\
- & \quad \varepsilon_a X E_z^2(1-3(X^2+Y^2)/4) - \chi_a X B_z^2(1-3(X^2+Y^2)/4) \\
+ & \quad \chi_a \frac{2}{\mathrm{d}} \int_{z_0}^{z_0+\mathrm{d}} B_z B_x \sin{(k'z)}\mathrm{d}z \\
- & \quad \chi_a \frac{2}{\mathrm{d}} [2X^2 \int_{z_0}^{z_0+\mathrm{d}} B_z B_x \sin^3{(k'z)}\mathrm{d}z + 2XY \int_{z_0}^{z_0+\mathrm{d}} B_z B_y \sin^3{(k'z)}\mathrm{d}z \\
+ & \quad \frac{X^2+Y^2}{2} \int_{z_0}^{z_0+\mathrm{d}} B_z B_x \sin^3{(k'z)}\mathrm{d}z] \\
\gamma\dot{Y} = & \quad K_3[\nabla_\perp Y - k^2Y + k^2Y(X^2+Y^2)/4] - (K_3-K_1)[(\partial_{xx}X + \partial_{xy}Y) - Yk^2(X^2+Y^2)/2] \\
- & \quad (K_2-K_3)[\partial_{yy}Y - \partial_{xy}X] \\
- & \quad \varepsilon_a Y E_z^2(1-3(X^2+Y^2)/4) - \chi_a X B_z^2(1-3(X^2+Y^2)/4) \\
+ & \quad \chi_a \frac{2}{\mathrm{d}} \int_{z_0}^{z_0+\mathrm{d}} B_z B_x \sin{(k'z)}\mathrm{d}z \\
- & \quad \chi_a \frac{2}{\mathrm{d}} [2Y^2 \int_{z_0}^{z_0+\mathrm{d}} B_z B_x \sin^3{(k'z)}\mathrm{d}z + 2XY \int_{z_0}^{z_0+\mathrm{d}} B_z B_y \sin^3{(k'z)}\mathrm{d}z \\
+ & \quad \frac{X^2+Y^2}{2} \int_{z_0}^{z_0+\mathrm{d}} B_z B_x \sin^3{(k'z)}\mathrm{d}z]
\end{aligned}
$$

$$
\begin{aligned}
\gamma\dot{X} = & \quad K_3[\nabla_\perp X + k^2X + k^2X(X^2+Y^2)/4] \\
- & \quad (K_3-K_1)[(\partial_{xx}X + \partial_{xy}Y) - Xk^2(X^2+Y^2)/2] + (K_2-K_3)[\partial_{yy}X - \partial_{xy}Y] \\
- & \quad \varepsilon_a X E_z^2(1-3(X^2+Y^2)/4) - \chi_a X B_z^2(1-3(X^2+Y^2)/4) \\
+ & \quad \chi_a \frac{4}{\pi} B_x B_z - \chi_a B_z \frac{8}{3\pi}[2X^2 B_y + 2XYB_x + B_y(X^2+Y^2)/2] \\
\gamma\dot{Y} = & \quad K_3[\nabla_\perp Y + k^2Y + k^2Y(X^2+Y^2)/4] \\
- & \quad (K_3-K_1)[(\partial_{xx}Y + \partial_{xy}X) - Yk^2(X^2+Y^2)/2] + (K_2-K_3)[\partial_{yy}X - \partial_{xy}Y] \\
- & \quad \varepsilon_a Y E_z^2(1-3(X^2+Y^2)/4) - \chi_a Y B_z^2(1-3(X^2+Y^2)/4) \\
+ & \quad \chi_a \frac{4}{\pi} B_x B_z - \chi_a B_z \frac{8}{3\pi}[2Y^2 B_y + 2XYB_x + B_y(X^2+Y^2)/2]
\end{aligned}
$$

Rewriting with the help of the complex parameter $A = X + \mathrm{i}Y$, defining $\partial_\eta = \partial_x + \mathrm{i}\partial_y$ and after straightformard calculations:

$$\partial_t A = \underbrace{\left[\lambda_0 + \varepsilon_a \left(\frac{V_0}{\mathrm{d}}\right)^2 + \chi_a B_z^2(z_0)\right]}_{\mu} A - a|A|^2 A + \frac{K_1+K_2}{2}\nabla^2 A + \frac{K_1-K_2}{2}\partial_{\eta\eta}\bar{A}$$
$$-\frac{4\chi_a}{\pi}B_z(z_0)B_\rho(z_0) - \frac{8\chi_a}{3\pi}B_z(z_0)B_\rho(z_0)\left(2A\mathrm{Re}(A\mathrm{e}^{-\mathrm{i}\theta}) + \frac{|A|^2\mathrm{e}^{\mathrm{i}\theta}}{2}\right)$$

with

$$\boxed{\lambda_0 = -K_3\left(\tfrac{\pi}{\mathrm{d}}\right)^2 \qquad a = \tfrac{1}{4}\left[(K_1-K_3)\left(\tfrac{\pi}{\mathrm{d}}\right)^2 - 3\varepsilon_a E_z^2 - 3\chi_a B_z^2\right]}$$

dropping the smaller correction and reescaling the parameter A:

$$A(\vec{\rho}, t) \to \frac{\gamma}{\sqrt{a}} A\left(\vec{r}\sqrt{\frac{2}{K_1+K_2}}, t\right)$$

we obtain:

$$\boxed{\partial_t A = \mu A - |A|^2 A + \nabla^2 A + \delta\partial_{\eta\eta}\bar{A} + bB_\rho(z_0)B_z(z_0)\mathrm{e}^{\mathrm{i}\theta}} \tag{5.2}$$

where $\delta = (K_1 - K_2)/(K_1 + K_2)$ and $b = \frac{4\chi_a\sqrt{a}}{\gamma\pi}$. This corresponds to a *Topologically Driven Ginzburg Landau* equation. Then, renormalizing the variables $\rho = \sqrt{x^2+y^2}/z_0$ and considering the Fermi limit $z_0 \gg 1$ under the Fréedericksz transition (in analogy to the limit used to deduce the Rayleigh vortex solution), we obtain the following approximate stationary solution:

$$\boxed{A(\rho) = -\frac{bB_z(\rho, z_0)B_\rho(\rho, z_0)}{\mu}\mathrm{e}^{\mathrm{i}\theta}} \tag{5.3}$$

It can be checked that the error of this approximate solution is of order $O\left(\frac{1}{z_0^4}\right)$, in other words, the nonlinear term and the spatial derivatives are negligible in this limit.

This solution goes to zero when $\rho = 0$ and $\rho = \sqrt{2z_0^2 + \varepsilon}$, where ε is a phenomenological parameter that accounts for the magnet width. Consequently the forcing term will induced a +1 vortex at the sample center and any number of ±1 vortices on the circle of radius $\rho = \sqrt{2z_0^2 + \varepsilon}$ consistent with the global topological constraint.

However in the actual physical experimente and due to the anisotropic nature of the nematic liquid crystal only two vortices of opposite charge remains close to the magnet boundaries (c.f Figure 5.11)

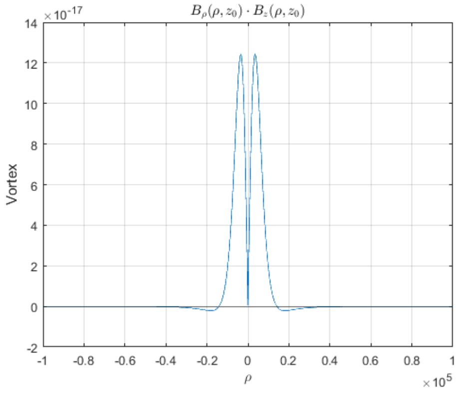

Figure 5.10: Magnetic induced vortex profile

Figure 5.11: Induced vortex triplet

Numerical simulations of model (5.2) were conducted considering a triangular finite element code with adaptative spatial and temporal steps, and a simulation box of dimensions 150×150 with Neumann boundary condition. This matches qualitatively the experimental observations.

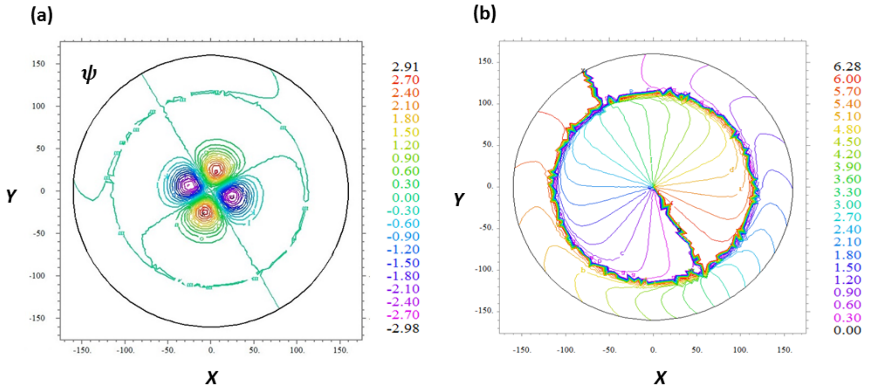

Figure 5.12: (a) Contour plot of the nullcline field $\psi(x, y) = Re(A)Im(A)$. (d) Phase field of the complex amplitude $A(x, y)$

Restricted to the region $\rho < \sqrt{2z_0^2 + \varepsilon}$ we can study the accuracy of the Fermi approximation (5.3)

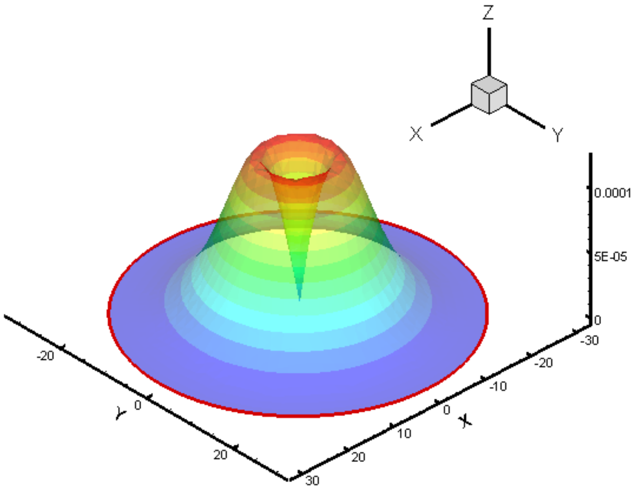

Figure 5.13: Tridimensional graph of the magnitude of the complex amplitude $A(x, y)$ in the Fermi Approximation

In Figure 5.14 (a) we observed the vector representation of the complex amplitude A, with horizontal and vertical components corresponding, respectively to the real and imaginary parts of A , in (b) a contour plot of the nullcline field $\psi(x, y) = Re(A)Im(A)$ while (c) corresponds to the phase field associated.

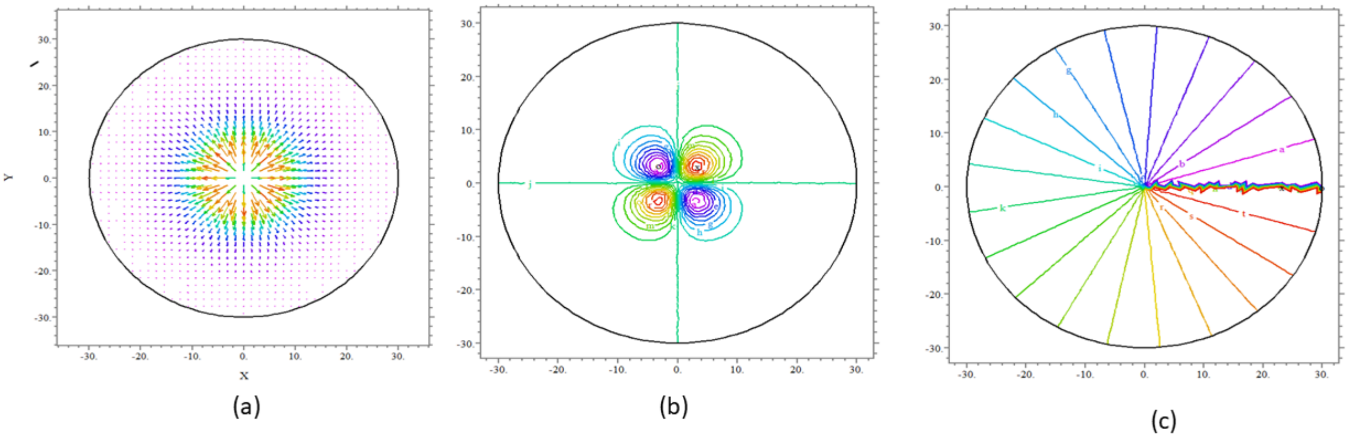

(a)

(b)

(c)

Figure 5.14: Induced vortex obtained from numerical simulations

In the onset of the transition point, numerical and theorical simulations show quite fair agreement (in green the Fermi approximation and in red the corresponding numerical solution):

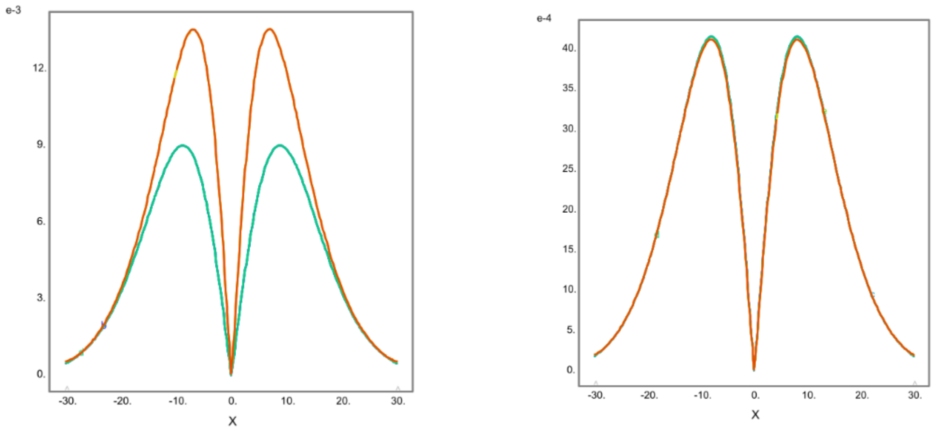

Figure 5.15: Fermi solution against numerical simulations with $\mu = -0.5$ and $\mu = -3$

5.4.1 Existence of Shadow Vortex

In the vicinity of the Fréedericksz transition, under the critical transition threshold numerical simulations shows that when the voltage is decreased the vortex in the center becomes unstable. As a result, it moves away from the origin towards the boundaries of the system reaching an equilibrium position eventually.

We call this type of singularity a *shadow vortex* and has beed studied in the context of light-matter interaction in liquid crystal light valves by Clerc et al [53, 54]. (c.f. Chapter 4). Experimental observation has not been possible, given the absence of a continuum magnetic field generator, since the available magnets are too weak or too strong to provide careful measurements.

In Figure 5.16 (a) we observed the vector representation of the complex amplitude A of the shadow vortex with magnetic forcing, with horizontal and vertical components corresponding, respectively to the real and imaginary parts of A , in (b) a contour plot of the nullcline field $\psi(x, y) = Re(A)Im(A)$ while (c) corresponds to the phase field associated.

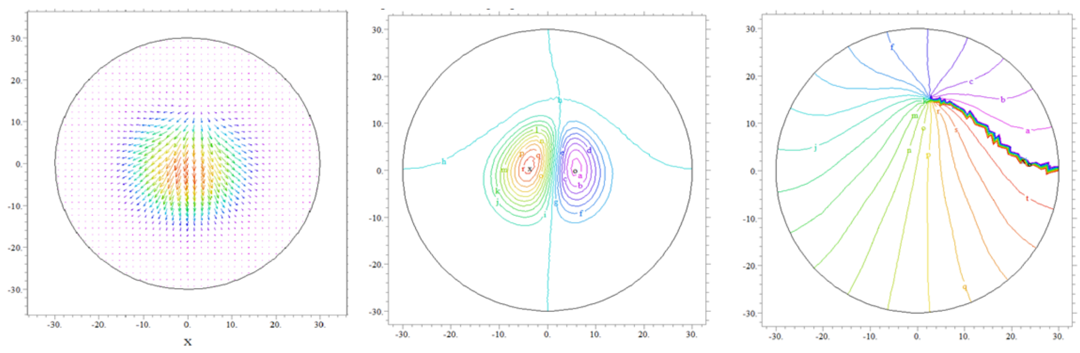

Figure 5.16: Shadow vortex under magnetic forcing. Left: Vector Representation. Center: Contour plot of the nullcline field. Right: Phase Field

Numerical results shows the existence of two vortex (Standard and shadow) that bifurcates accordingly a Supercritical Pitchfork Bifurcation when the control parameter μ reach a critical value. Taking as order parameter the separation r between the origin and the vortex position, then as a function of the control parameter μ this order parameter follows the universal law $r \sim \sqrt{\mu - \mu_c}$.

In Figure 5.17 we present a curve fitting in log-log scale of r in function of μ obtained numerically.

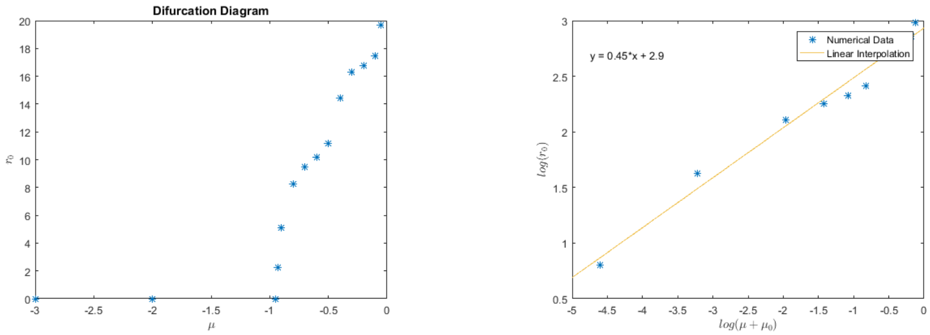

Figure 5.17: Left: Numerical data of the separation r between the sample center and the vortex position. Right: Curve fitting of numerical data in log-log scale

Chapter 6

Defects dynamics

6.1 Moving Defects

The problem of motion of topological defects on a spatially innhomogeneous background arises in connection with studies of vortex confinement in superfluids and superconductors. Indeed, Schwarz [60] studied the motion of a quantized vortex in superfluid He^4 attracted to a pinning site on a macroscopically rough surface. This problem has been widely studied by Pismen, Rica and others [1, 61, 62, 63].

We shall consider the motion of vortices in the dissipative Ginzburg Landau equation in 2D with a variable supercritically parameter and a external forcing term. The basic equation can be written as

$$\partial_t u = \nabla^2 u + (\mu(r) - |u|^2)u + F(r). \tag{6.1}$$

It is assumed that the relief $\mu(r)$ varies on a scale large compared to the size of the vortex core. As seen in chapter 3, topologically non-trivial vortex solution have a general form

$$u(r,t) = \rho(r,t)\mathrm{e}^{\mathrm{i}\theta(r,t)}.$$

where the phase θ of a vortex with a topological charge $n \neq 0$ satisfies the circulation condition

$$\oint_\Gamma \nabla\theta \cdot \mathrm{d}\vec{l} = 2\pi n.$$

on any closed contour Γ surrounding the vortex position. The vortex position can be defined precisely as a zero of the complex order parameter field. A stationary solution corresponding to an isolated circularly symmetric vortex exists at $\mu =$ const. and $F = 0$. The vortex is set into motion when the circular symmetry is broken owing to spatial inhomogeneities, external fields, or presence of other vortices.

6.2 One-Dimensional Case

To understand the dynamics of defects, we first consider the problem in the one-dimensional approach discussed in Section 4.7.

$$\partial_t u = \varepsilon u - u^3 + \partial_{xx} u + \delta \mathrm{e}^{-\alpha x^2} u - \delta\beta x \mathrm{e}^{-\alpha x^2}. \tag{6.2}$$

where $u(x,t)$ is a one dimensional order parameter, ε is a control parameter, β stands for the intensity of the forcing term and $\delta \ll 1$ is a formal expansion parameter. The previous model corresponds to the perturbed real Ginzburg Landau equation or the overdamped ϕ^4 model. Topologically non trivial solutions of (7.1) are **kinks** and can be written explicitly:

$$\boxed{\mathrm{u}_{KINK} = \sqrt{\varepsilon} tanh\left(\sqrt{\tfrac{\varepsilon}{2}} x\right) \qquad u'_{KINK} = \tfrac{\varepsilon}{\sqrt{2}} sech^2\left(\sqrt{\tfrac{\varepsilon}{2}} x\right)}$$

Looking for solutions of (5.1) in the form of an expansion in the small parameter δ

$$u = u_{KINK}\underbrace{(x_0 - Vt)}_{=x(t)} + \delta\varphi.$$

In the comoving frame $u = u(x_0 - Vt) \Rightarrow \partial_t u = -Vu'_{KINK}$, and follows

$$\begin{aligned} -Vu'_{KINK} &= \varepsilon u_{KINK} + \delta\varepsilon\varphi - [u^3_{KINK} + 3u^2_{KINK} \cdot \delta\varphi + 3u_{KINK}(\delta\varphi)^2 + (\delta\varphi)^3] \\ &+ \delta \mathrm{e}^{-\alpha x^2} u_{KINK} + \delta^2 \mathrm{e}^{-\alpha x^2}\varphi - \delta\beta x \mathrm{e}^{-\alpha x^2} + \partial_{xx} u_{KINK} + \delta\partial_{xx}\varphi. \end{aligned}$$

Writting the *order zero* solution in δ, u_{KINK} verifies

$$\varepsilon u_{KINK} - u^3_{KINK} + \partial_{xx} u_{KINK} = 0.$$

While the *first order* equation reads

$$-Vu'_{KINK} = \varepsilon\varphi + \partial_{xx}\varphi + 3u^2_{KINK}\varphi + \mathrm{e}^{-\alpha x^2} u_{KINK} - \beta x \mathrm{e}^{-\alpha x^2},$$

rearranging

$$-Vu_{KINK} = \mathcal{L}\varphi + \mathrm{e}^{-\alpha x^2} u_{KINK} - \beta x \mathrm{e}^{-\alpha x^2}, \tag{6.3}$$

where $\mathcal{L}$ is the linear operator:

$$\mathcal{L}\varphi = [\varepsilon\varphi + 3u^2_{KINK}\varphi + \partial_{xx}\varphi]. \tag{6.4}$$

Equivalently (7.2) can be written:

$$\mathcal{L}\varphi = \underbrace{\mathrm{e}^{-\alpha x^2} u_{KINK} - \beta x \mathrm{e}^{-\alpha x^2} + Vu_{KINK}}_{=\Phi}. \tag{6.5}$$

The solvability condition of the first-order equation (7.4) is the orthogonality of the inhomogeneous part to the eigenfunction $u'_{KINK} \in \mathbb{K}er\mathcal{L}^*$ under the scalar product:

$$\langle f, g\rangle = \int_{-\infty}^{\infty} f \cdot g \mathrm{d}l.$$

Then, by Fredholm Alternative [64]

$$\langle \mathcal{L}\varphi, u'_{KINK}\rangle = \langle \Phi, u'_{KINK}\rangle = 0,$$

which leads to the velocity of the defect as a function of x

$$V(x) = \frac{\beta \int_{-\infty}^{\infty} (x - x_0) \mathrm{e}^{-\alpha(x-x_0)^2} u'_{KINK} \mathrm{d}x_0 - \int_{-\infty}^{\infty} \mathrm{e}^{-\alpha(x-x_0)^2} u_{KINK} u'_{KINK \mathrm{d}x_0}}{\int_{-\infty}^{\infty} u'_{KINK} \cdot u'_{KINK} \mathrm{d}x} \tag{6.6}$$

it is possible to identify

$$I_1(x) = \beta \int_{-\infty}^{\infty} (x - x_0) \mathrm{e}^{-\alpha(x-x_0)^2} u'_{KINK} \mathrm{d}x_0, \qquad I_2(x) = \int_{-\infty}^{\infty} \mathrm{e}^{-\alpha(x-x_0)^2} u_{KINK} u'_{KINK \mathrm{d}x_0}$$

as potential whose superposition generate the motion of the perturbed defect. This way equation (6.6) correspond to a motion equation for the vortex position (kinetic equation)

$$\dot{x} = I_1(x) - I_2(x)$$

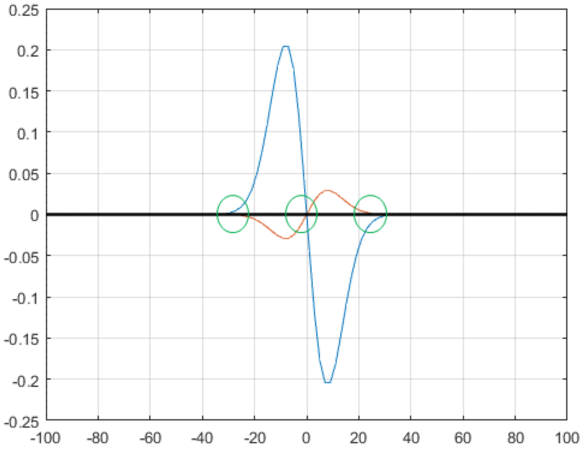

Figure 6.1: Red:$I_1(x)$. Blue:$I_2(x)$. Green circles acounts for the emergence of equilibria

These two potentials give rise to forces that compete with each other shifting the equilibrium kink position away from the origin. Figure 6.2 shows the existence of two new equilibria depending on the direction of the net force acting on the kink

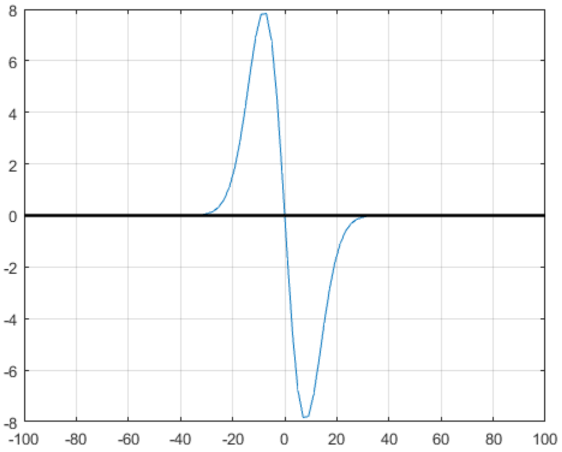

Figure 6.2: Potential: $I_1(x) - I_2(x)$

6.3 Previous results for vortex motion

Following the previous studies done by Pismen and Rubistein in [65], we derive the equation of vortex motion using the method of matched asymptotic expansion on the core and far field solutions [1]. The matching procedure results in a mobility relationship connecting the vortex velocity with the local gradient of the supercritically parameter.

In the core region, we use the comoving coordinate frame centered on the vortex position $\vec{r}_0$ and propagating withn a slow velocity $\varepsilon\vec{v}$. Stationary solutions in the comoving frame verify the equation

$$\varepsilon\vec{v} \cdot \nabla u + \nabla^2 u + (\mu(r) - |u|^2)u = 0. \tag{6.7}$$

The local relief in the core region is expanded in Taylor series

$$\mu(\vec{r}) = \mu(\vec{r}_0) + \varepsilon\vec{M} \cdot \vec{r} + \cdots = \mu_0 + \varepsilon\mu_1 + \ldots,$$

where $\vec{M} = \nabla\mu(\vec{r}_0)$.

We are looking for a solution of equation (6.7) in the form of an expansion in the small parameter ε:

$$u = u_0 + \varepsilon u_1 + \varepsilon^2 u_2 + \ldots.$$

The *zero-order* solution is written in the polar coordinate frame r, θ as $u_0 = \rho_0(r)\mathrm{e}^{\mathrm{i}\theta}$, where the function $\rho_0(r)$ verifies the stationary zero-order equation

$$\rho_0'' + \frac{1}{r}\rho_0' + \left(\mu_0 - \frac{1}{r^2} - \rho_0^2\right)\rho_0 = 0. \tag{6.8}$$

The *first-order* equation reads

$$\mathcal{L}(u_1, u_1^*) = -\vec{v} \cdot \nabla u_0 - \mu_0\mu_1 u_0. \tag{6.9}$$

where $\mathcal{L}$ is the linear operator

$$\mathcal{L}(u_1, u_1^*) = \nabla^2 u_1 + (\mu_0 - 2|u_0|^2)u_1 - u_0^2 u_1^*. \tag{6.10}$$

The solvability condition of the first order equation is the orthogonality of the inhomogeneous part to the eigenfunction ∇u_0^*. In order to avoid divergencs, the solvability condition has to be obtained by integration over a circle with radius $L = O(\varepsilon^{-1/2}) \gg 1$:

$$Re\left\{\int_0^L r\mathrm{d}r \int_0^{2\pi} \mathrm{d}\theta \nabla u_0^*(\vec{v}\cdot\nabla u_0 + \mu_0\mu_1 u_0) + L\int_0^{2\pi}(\nabla u_0^* \cdot \partial_r u_1 - u_1 \cdot \partial_r \nabla u_0^*)_{r=L}\right\} = 0. \tag{6.11}$$

The contour integral depends on the asymptotics of the first- order field u_1. Since $\rho_0(L) = \mu_0(1 - O(\varepsilon))$, ∇u_0^* can be multiplied by a cut-off function in order to avoid divergences in the phase field and to obtain simple qualitative results.

The area integral in (4.11) is evaluated as

$$\pi \int_0^L \mathrm{d}r \rho_0'(r)\rho_0(r)(2v - Mr^2\mu_0)$$

The term proportional to v can be computed using (4.8) as $\pi v \mu_0$, while the second term can be calculated numerically using the core solution as $2\pi M\mu_0 \ln(a_1 L\mu_0)$, where the constant a_1 is given numerically as $\ln a_1 = 0.405$. Thus, the mobility relation takes the form

$$v \sim 2M \ln a_1 \mu_0 \tag{6.12}$$

6.4 Vortex dynamics in the Topologically Driven Ginzburg Landau equation

Considering the previous studies done for the Isotropic Ginzburg Landau Equation by Bodenchatz et al in [63]. We follow the same procedure for the Topologically Driven Ginzburg-Landau equation:

$$\partial_t A = (\varepsilon + \alpha \mathrm{e}^{-\gamma r^2})A - A|A|^2 + \nabla_\perp^2 A + \beta r \mathrm{e}^{-\gamma r^2}. \tag{6.13}$$

Rewriting the equation as

$$\partial_t A = \varepsilon A - A|A|^2 + \nabla_\perp^2 A + \alpha \mathrm{e}^{-\gamma r^2})A + \beta r \mathrm{e}^{-\gamma r^2},$$

we can consider the last terms as perturbations and as vortices are still solutions, we insert the **ansatz** of a vortex moved by a phase disturbance:

$$A = R(\vec{r} - \vec{r}_0(t))\mathrm{e}^{\mathrm{i}\vec{k}\cdot\vec{r}} + W$$

where R is the vortex solution of the Isotropic Ginzburg Landau equation, $k = Q\hat{x} + P\hat{y}$ is a phase disturbance and W are small nonlinear corrections.

Inserting the ansatz into the equation we obtain to the leading order

$$\begin{aligned} -\dot{x}_0\partial_x R - \dot{y}_0\partial_y R = & \quad (\varepsilon W - R^2\bar{W} - 2|R|^2 + \nabla^2 W) + 2\mathrm{i}Q\partial_x R + 2\mathrm{i}P\partial_y R \\ - & \quad (Q^2 + P^2)R + \alpha \mathrm{e}^{-\gamma r^2} R + \beta r \mathrm{e}^{-\gamma r^2} \mathrm{e}^{\mathrm{i}\theta} \end{aligned}$$

The linear operator acting on W is

$$\mathcal{L} = \begin{pmatrix} \varepsilon - 2|R|^2 + \nabla^2 & -R^2 \\ -\bar{R}^2 & \varepsilon - 2|R|^2 + \nabla^2 \end{pmatrix}$$

and the Kernel of its conjugate is

$$K\mathrm{er}\{\mathcal{L}\dagger\} = \left\{ \begin{pmatrix} \partial_x R \\ \partial_x \bar{R} \end{pmatrix}, \begin{pmatrix} \partial_y R \\ \partial_y \bar{R} \end{pmatrix} \right\}$$

Using solvability condition with the first and the second of the kernel elements we obtain respectively

$$\begin{aligned} 0 = & \quad \dot{x}_0 \quad (\langle \partial_x R | \partial_x R \rangle + \langle \partial_x \bar{R} | \partial_x \bar{R} \rangle) + 2\mathrm{i}P((\langle \partial_x R | \partial_y R \rangle + \langle \partial_x \bar{R} | \partial_y \bar{R} \rangle) \\ & + \quad \alpha(\langle \partial_x R | \mathrm{e}^{-\gamma r^2} R \rangle + \langle \partial_x \bar{R} | \mathrm{e}^{-\gamma r^2} \bar{R} \rangle) + \beta(\langle \partial_x R | r\mathrm{e}^{-\gamma r^2} \rangle + \langle \partial_x \bar{R} | r\mathrm{e}^{-\gamma r^2} \rangle)\delta(\theta - \vec{k} \cdot \vec{r}) \\ 0 = & \quad \dot{y}_0 \quad (\langle \partial_y R | \partial_y R \rangle + \langle \partial_y \bar{R} | \partial_y \bar{R} \rangle) + 2\mathrm{i}P((\langle \partial_y R | \partial_x R \rangle + \langle \partial_y \bar{R} | \partial_x \bar{R} \rangle) \\ & + \quad \alpha(\langle \partial_y R | \mathrm{e}^{-\gamma r^2} R \rangle + \langle \partial_y \bar{R} | \mathrm{e}^{-\gamma r^2} \bar{R} \rangle) + \beta(\langle \partial_y R | r\mathrm{e}^{-\gamma r^2} \rangle + \langle \partial_y \bar{R} | r\mathrm{e}^{-\gamma r^2} \rangle)\delta(\theta - \vec{k} \cdot \vec{r}) \end{aligned}$$

where the first inner product in each equation corresponds to the mobility of the solution and requires a renormalization in the phase in order to be calculated [63]. Solving the inner products is possible to obtain the kinetic equation. In this case numerical integration is needed and results are in progress, but we expect as in the one-dimensional case the emergence of new equilibria position for the vortex solution.

Chapter 7

Variational Approach

In this chapter we study the qualitative properties of global minimizers of the Ginzburg-Landau energy which describes light-matter interaction; the principal results accounts for the symmetry breaking phenomenon as the physical parameters of the problem vary. This section it is based mainly in the articles by Clerc, Kowalczyk and Smyrnelys [55],[54].

7.1 Euler Lagrange Equations

To the describe the formation of defects in liquid crystal starting form the classical Frank-Ossen energy near the Freédericksz transition, one can reduce the problem to considering the Ginzburg Landau equation [1]. After some transformations involving scaling to nondimensional variables the energy takes the form

$$E(u) = \int_{\mathbb{R}^2} \frac{1}{2}|\nabla u|^2 - \frac{1}{2\varepsilon^2}\mu(x)|u|^2 + \frac{1}{4\varepsilon}|u|^4 - \frac{a}{\varepsilon}f(x)\cdot u,$$

where $u = (u_1, u_2) \in H^1(\mathbb{R}^2, \mathbb{R}^2)$, and $\varepsilon > 0$, [1]$a \geq 0$ are real parameters. In the physical context of Chapter 4. the functions μ and f are specific

$$\mu(x) = \mathrm{e}^{-|x|^2} - \chi, \qquad \text{with some } \chi \in (0,1), \qquad f(x) = -\frac{1}{2}\nabla\mu(x).$$

Under more general hypothesis on μ and f, we suppose that $\mu \in \mathcal{C}^\infty(\mathbb{R}^2, \mathbb{R})$ is radial, i.e. $\mu(x) = \mu_{rad}(|x|)$,with $\mu_{rad} \in \mathcal{C}^\infty(\mathbb{R}, \mathbb{R})$ an even function. We take $f = (f_1, f_2) \in \mathcal{C}^\infty(\mathbb{R}^2, \mathbb{R}^2)$ also to be radial, i.e. $f(x) = f_{rad}(|x|)\frac{x}{|x|}$, with $f_{rad} \in \mathcal{C}^\infty(\mathbb{R}., \mathbb{R})$ an odd function. In addition we assume that:

$$\begin{cases} \mu \in L^\infty(\mathbb{R}^2, \mathbb{R}),\ \mu'_{rad} < 0 \text{ in } (0,\infty), \text{ and } \mu_{rad}(\rho) = 0 \text{ for a unique } \rho > 0 \\ f \in L^1(\mathbb{R}^2, \mathbb{R}^2) \cap L^\infty(\mathbb{R}^2, \mathbb{R}^2), \text{ and } f_{rad} > 0 \text{ on } (0, \infty) \end{cases}$$

---

[1] Keep in mind that ε plays the role of $1/\omega$

The Euler-Lagrange equation of E is:

$$\varepsilon^2\nabla^2 u + \mu(x)u - |u|^2 u + \varepsilon a f(x) = 0, \qquad x \in \mathbb{R}^2. \tag{7.1}$$

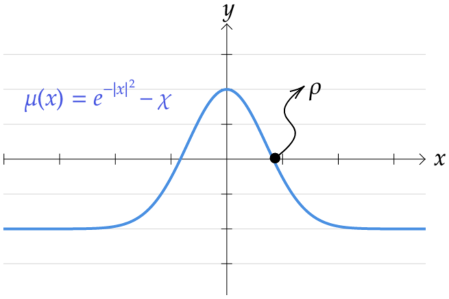

Figure 7.1: $\mu(x) = \mathrm{e}^{-|x|^2} - \chi$

Some properties of the global minimizers are stated in

Theorem 7.1 *Let $v_{\varepsilon,a}$ be a global minimizer of E, let $a \geq 0$ be bounded (possilbly dependent on ε), let $\rho > 0$ be the zero of μ_{rad} and let $\mu_1 = \mu'_{rad}(\rho) < 0$. The following statements hold:*

1. *Let $\Omega \subset D(0;\rho)$ be an open set such that $v_{\varepsilon,a} \neq 0$ on Ω, for every $\varepsilon \ll 1$. Then $|v_{\varepsilon,a}| \to \sqrt{\mu}$ in $\mathcal{C}^0_{loc}(\Omega)$.*
2. *For every $\xi = \rho \mathrm{e}^{\mathrm{i}\theta}$, we consider the local coordinates $s = (s_1, s_2)$ in the basis $(\mathrm{e}^{\mathrm{i}\theta}, \mathrm{i}\mathrm{e}^{\mathrm{i}\theta})$, and the rescaled minimizers:*

$$w_{\varepsilon,a}(s) = 2^{-1/2}(-\mu_1\varepsilon)^{-1/3} v_{\varepsilon,a}\left(\xi + \varepsilon^{2/3}\frac{s}{(-\mu_1)^{1/3}}\right).$$

Assuming that $\lim_{\varepsilon\to 0} a(\varepsilon) = a_0$, then as $\varepsilon \to 0$ the function $w_{\varepsilon,a}$ converges in $\mathcal{C}^2(\mathbb{R}^2,\mathbb{R}^2)$ up to subsequence to a function y bounded in $[s_0,\infty)\times\mathbb{R}$ for every $s_0 \in \mathbb{R}$, which is a minimal solution of:

$$\Delta y(s) - s_1 y(s) - 2|y(s)|^2 y(s) - \alpha = 0 \qquad \forall s = (s_1, s_2) \in \mathbb{R}^2, \tag{7.2}$$

with $\alpha = \frac{a_0 f(\xi)}{\sqrt{2}\mu_1} \in \mathbb{R}^2$

3. *Assuming that $\lim_{\varepsilon\to 0} a(\varepsilon) = a_0$, then for every $r_0 > \rho$, we have $\lim_{\varepsilon\to 0}\frac{v_{\varepsilon,a}((r_0+t\varepsilon)\mathrm{e}^{\mathrm{i}\theta})}{\varepsilon} = -\frac{a_0}{\mu_{rad}(r_0)} f(r_0\mathrm{e}^{\mathrm{i}\theta})$ uniformly when t remains bounded and $\theta \in \mathbb{R}$.*

Theorem 5.1 gives account on how nonsmoothness of the limit of $|v_{\varepsilon,a}|$ is mediated near the circumference $|x| = \rho$, where μ changes sign, through equation (5.1). This equation is a generalization of the second Painlevé equation:

$$y'' - sy - 2y^3 - \alpha = 0, \qquad s \in \mathbb{R}. \tag{7.3}$$

We state now the following theorem due to Clerc-Smyrnelis-Kowalczyk [54] that shows existence of topological defects of the global minimizers of E in several regimes of the parameters (ε, a):

Theorem 7.2 *Let $v_{\varepsilon,a}$ be a global minimizer. Assume that $a(\varepsilon) > 0$, a is bounded and $\lim_{\varepsilon\to 0} \varepsilon^{1-\frac{3\gamma}{2}} \ln a = 0$ for some $\gamma \in [0, 2/3)$.*

1. *For $\varepsilon \ll 1$, $v_{\varepsilon,a}$ has at least one zero $\bar{x}_\varepsilon$ such that*

$$|\bar{x}_\varepsilon| \leq \rho + o(\varepsilon^\gamma). \tag{7.4}$$

In addition, any sequence of zeros of $v_{\varepsilon,a}$, either satisfies (5.3) or it diverges to ∞.

2. *For every $\rho_0 \in (0, \rho)$, there exist $b_* > 0$ such that when $\limsup_{\varepsilon\to 0} \frac{a}{\varepsilon|\ln\varepsilon|} < b_*$, then any limit point $l \in \mathbb{R}^2$ of the set of zeros of $v_{\varepsilon,a}$ satisfies:*

$$\rho_0 \leq |l| \leq \rho.$$

In adition, if $a = o(\varepsilon|\ln\varepsilon|)$, then $|l| = \rho$.

3. *On the other hand, for every $\rho_0 \in (0, \rho)$, there exist $b^* > 0$ such that when $\limsup_{\varepsilon\to 0} \frac{a}{\varepsilon|\ln\varepsilon|^2} > b^*$, the set of zeros of $v_{\varepsilon,a}$ has a limit point l such that*

$$|l| \leq \rho_0.$$

If $v_{\varepsilon,a}(\bar{x}_\varepsilon) = 0$ and $\bar{x}_\varepsilon \to l$, then up to a subsequence

$$\lim_{\varepsilon\to 0} v_{\varepsilon,a}(\bar{x}_\varepsilon + \varepsilon s) \to \sqrt{\mu(l)}(g \circ \eta)(\sqrt{\mu(l)}s),$$

in $\mathcal{C}^2_{loc}(\mathbb{R}^2)$, for some $g \in O(2)$. In addition, if $\limsup_{\varepsilon\to 0} \frac{a}{\varepsilon|\ln\varepsilon|^2} = \infty$ then $l = 0$.

Theorem 7.3 *(i) When $a = 0$, the global minimizer can be written as $v(x) = (v_{rad}(|x|), 0)$ with $v_{rad} \in \mathcal{C}^\infty(\mathbb{R})$ positive. It is unique up to change of v by gv with $g \in SO(2)$*[2].

(ii) Given $\varepsilon > 0$, there exists $A > 0$ such that for every $a > A$, the global minimizer $v_{\varepsilon,a}$ is unique and radial,i.e. $v(x) = v_{rad}(|x|)\frac{x}{|x|}$.

Theorem 5.3 shows that when $a = 0$ the global minimizer of E inherits the one dimensional radial profile of μ. On the other hand, it would be natural to expect that when $a > 0$ the forcing term $\varepsilon a f$ induces a global minimizer v in the class $H^1_{rad}(\mathbb{R}^2, \mathbb{R}^2) = \{u \in H^1(\mathbb{R}^2, \mathbb{R}^2) : gu(x) = u(gx), \forall g \in O(2)\}$ of radial maps; this is not the case unless $\mu < 0$ when the global minimizers corresponds with the Rayleigh vortex solution introduced in Chapter 4.

7.2 General Results for Minimizers and Solutions

In this section we state general results for minimizers and solutions that are valid for any values of the parameters $\varepsilon > 0$ and $a \geq 0$.

Lemma 7.4 ***Existence of global minimizwr***
For every $\varepsilon > 0$ and $a \geq 0$, there exists $v \in H^1(\mathbb{R}^2, \mathbb{R}^2)$ such that $E(v) = \min_{H^1(\mathbb{R}^2,\mathbb{R}^2)} E$. As a consequence, v is a $\mathcal{C}^\infty$ classical solution of (5.1), and moreover $v(x) \to 0$ as $|x| \to \infty$.

---

[2] Special orthogonal group of the 2×2 orthogonal matrices of determinant 1

Proof. We first show that $\inf E(u) : u \in H^1(\mathbb{R}^2,\mathbb{R}^2) > -\infty$. To see this, we regroup the last three terms in the integral of $E(u)$. Setting $I_\delta = \{x \in \mathbb{R}^2 : \mu(x) + \delta > 0\}$, for $\delta > 0$ sufficiently small such that I_δ is bounded, we have:

$$-\frac{1}{2\varepsilon^2}\mu(x)|u|^2 + \frac{1}{8\varepsilon^2}|u|^4 < 0 \Leftrightarrow u^2 < 4\mu \Rightarrow x \in I_\delta,$$

thus

$$-\frac{1}{2\varepsilon^2}\mu(x)|u|^2 + \frac{1}{8\varepsilon^2}|u|^4 \geq -\frac{2}{\varepsilon^2}\|\mu\|^2_{L^\infty}\chi_\delta,$$

where χ_δ is the characteristic function of I_δ. On the other hand,

$$\frac{1}{8\varepsilon^2}|u|^4 - \frac{a}{\varepsilon}f(x)\cdot u \geq -\frac{8^{1/3}a^{4/3}}{\varepsilon^{2/3}}|f|^{4/3}.$$

Next, we notice that $E(u) \in \mathbb{R}$ for every $u \in H^1(\mathbb{R}^2,\mathbb{R}^2)$, thanks to the imbedding $H^1(\mathbb{R}^2) \subset L^p(\mathbb{R}^2)$, for $2 \leq p < \infty$. Now, let $m = \inf_{H^1} E > -\infty$, and let u_n be a sequence such that $E(u_n) \to m$. Repeating the previous computation, we can bound

$$\begin{aligned}\int_{\mathbb{R}^2} \frac{1}{2}|\nabla u_n|^2 + \frac{\delta}{2\varepsilon^2}|u_n|^2 &= E(u_n) + \int_{\mathbb{R}^2} \frac{1}{2\varepsilon^2}(\mu(x)+\delta)|u_n|^2 - \frac{1}{4\varepsilon^2}|u_n|^2 + \frac{a}{\varepsilon}f(x)\cdot u \\ &\leq E(u_n) + \frac{2}{\varepsilon^2}(\|\mu\|_{L^\infty}+\delta)^2|I_\delta| + \frac{8^{1/3}a^{4/3}}{\varepsilon^{2/3}}|f|^{4/3}.\end{aligned}$$

From this expression it follows that $\|u_n\|_{H^1(\mathbb{R}^2,\mathbb{R}^2)}$ is bounded. As a consequence, for a subsequence still called u_n,$u_n \rightharpoonup v$ weakly in H^1, and thanks to a diagonal argument we also have $u_n \to v$ in L^2_{loc}, and almost everywhere in $\mathbb{R}^2$. Finally, by lower semicontinuity

$$\int_{\mathbb{R}^2} |\nabla v|^2 \leq \liminf_{n\to\infty} \int_{\mathbb{R}^2} |\nabla u_n|^2,$$

and by Fatou's Lemma [64] we have:

$$\int_{\mathbb{R}^2} |v|^4 \leq \liminf_{n\to\infty} \int_{\mathbb{R}^2} |u_n|^4.$$

$$\int_{\mu\leq 0} -\frac{1}{2\varepsilon^2}\mu|v|^2 \leq \liminf_{n\to\infty} \int_{\mu\leq 0} -\frac{1}{2\varepsilon^2}\mu|u_n|^2.$$

To conclude, it is clear that

$$\int_{\mu>0} -\frac{1}{2\varepsilon^2}\mu|v|^2 = \lim_{n\to\infty} \int_{\mu>0} -\frac{1}{2\varepsilon^2}\mu|u_n|^2,$$

thus $m \leq E(v) \leq \liminf_{n\to\infty} E(u_n) = m$. Next, we check that v is bounded. This follows from the fact that exists a constant M such that for every $x \in \mathbb{R}^2$ and i $= 1, 2$ the function

$$u_{\mathrm{i}} \to -\frac{1}{2\varepsilon^2}\mu(x)|u|^2 + \frac{1}{4\varepsilon^2}|u|^4 - \frac{a}{\varepsilon}f(x)\cdot u,$$

is strictly increasing on $[M, \infty)$ (resp. strictly decreasing on $(-\infty, -M]$) independently of the other variable u_j. Thus, if we truncate a map $u = (u_1, u_2)$ by setting $\hat{u_\text{i}} = \min(M, \max(u_\text{i}, -M))$, the truncated map $\hat{u}$ has smaller energy than u. Clearly the boundedness of v implies the boundedness of Δv and ∇v. In particular, v and $|v|^4$ are uniformly continuous. As a consequence, is $|v(x_n)| > \delta > 0$ for a sequence $|x_n| \to \infty$, then we would have $|v| > \delta/2$ on a ball $B(x_n, r)$, and also $\int_{\mathbb{R}^2} |v|^4 = \infty$, which is impossible. This proves the asymptotic convergence to 0. □

Remark The existence of the global minimizer when $\mu \in L^\infty(\mathbb{R}^{\nvDash}, \mathbb{R})$ is such that $\mu(x) < 0, \forall x$ (i.e. μ doesnt change signs); follows from the above calculations since

$$-\frac{1}{2\varepsilon^2}\mu(x)|u|^2 + \frac{1}{8\varepsilon^2}|u|^4 > 0, \quad \forall x.$$

Then, the functional

$$\begin{array}{rcl} F : H^1(\mathbb{R}^2, \mathbb{R}^2) & \to & \mathbb{R} \\ u & \to & \displaystyle\int_{\mathbb{R}^2} \frac{1}{2}|\nabla u|^2 - \frac{1}{2\varepsilon^2}\mu(x)|u|^2 + \frac{1}{4\varepsilon}|u|^4 - \frac{a}{\varepsilon}f(x) \cdot u, \end{array}$$

is convex, coercive and lower semicontinuous, and the existence of the global minimizer is given by the following functional analysis theorem, since $H^1(\mathbb{R}^2, \mathbb{R}^2)$ is reflexive:

Theorem 7.5 *If $F : X \to \mathbb{R}$ is a convex, lower semicontinuous and coercive functional defined on a reflexive Banach space, the F attains minimum on X i.e. there exists $x^* \in X$ such that $F[u^*] = \inf_X F[u]$. If in addition F is strictly convex, then the minimum is unique.*

Remark In the sequel, we will always denote the global minimizer by v.

7.2.1 Uniform bounds

Lemma 7.6 *For εa belonging to a bounded interval, let $u_{\varepsilon,a}$ be a solution of (5.1) converging to 0 as $|x| \to \infty$. Then, the solutions $u_{\varepsilon,a}$ and the maps $\varepsilon \nabla u_{\varepsilon,a}$ are uniformly bounded.*

PROOF. Dropping the indexes and writing $u := u_{\varepsilon,a}$. Since $|f|, \mu$ and εa are bounded, the roots of the cubic equation in the variable u_1:

$$u_1^3 + (u_2^2 - \mu(x))u_1 - \varepsilon a f_1(x) = 0,$$

belong to a bounded interval, for all values of x, u_2, ε, a. If u_1 takes positive values, then it attains its maximun $0 \leq \max_{\mathbb{R}^2} u_1 = u_1(x_0)$, at a point $x_0 \in \mathbb{R}^2$. In view of (5.1):

$$0 \geq \varepsilon^2 \Delta u_1(x_0) = u_1^3(x_0) + (u_2^2(x_0) - \mu(x_0))u_1(x_0) - \varepsilon a f_1(x_0),$$

thus it follows that $u_1(x_0)$ is uniformly bounded above. In the same way, we prove the uniform lower bound for u_1 and for u_2. □

Lemma 7.7 *For $\varepsilon \ll 1$ and a belonging to a bounded interval, let $u_{\varepsilon,a}$ be a solution of (5.1) converging to 0 as $|x| \to \infty$. Then, there exists a constant $K > 0$ such that*

$$|u_{\varepsilon,a}| \leq K\left(\sqrt{\max\left(\mu(x), 0\right) + \varepsilon^{1/3}}\right), \quad \forall x \in \mathbb{R}^2.$$

As a consequence, if for every $\xi = \rho e^{i\theta}$, we consider the local coordinates $s = (s_1, s_2)$ in the basis $(e^{i\theta}, ie^{i\theta})$, then the rescaled maps $u^*_{\varepsilon,a} = \frac{u_{\varepsilon,a}}{(\xi + s\varepsilon^{2/3})}\varepsilon^{1/3}$ are uniformly bounded on the half-planes $[s_0, \infty) \times \mathbb{R}$, $\forall s_0 \in \mathbb{R}$.

Lemma 7.8 *Assume a is bounded and let $u_{\varepsilon,a}$ be a solution of (5.1) uniformly bounded. Then the maps $\frac{u_{\varepsilon,a}}{\varepsilon}$ and $\nabla u_{\varepsilon,a}$ are uniformly bounded on the sets $\{x : |x| \geq \rho_1\}$ for every $\rho_1 > \rho$.*

7.3 Proof Theorem 5.1

1. Suppose by contradiction that $|v| \nrightarrow \sqrt{\mu}$ uniformly on a closed set $F \subset \Omega$. Then, there exist a sequence $\varepsilon_n \to 0$ and a sequence $\{x_n\} \subset F$ such that:

$$||v_{\varepsilon_n}(x_n)| - \sqrt{\mu(x_n)}| \geq \delta, \quad \text{for some } \delta > 0. \tag{7.5}$$

   Assuming that up to a subsequence $\lim_{n\to\infty} x_n = x_0 \in F$ and considering the reescaled maps $v^*_n(s) = v_{\varepsilon_n}(x_n + \varepsilon s)$:

$$\Delta v^*(s) + \mu(x_n + \varepsilon_n s)v^*(s) - |v^*(s)|^2 v^*(s) + \varepsilon_n a f(x_n + \varepsilon_n s), \quad \forall s \in \mathbb{R}^2. \tag{7.6}$$

   In view of the Lemma 5.6 and (5.5), v^*_n and its first derivatives are uniformly bounded for $\varepsilon \ll 1$, differentianting (5.5), one also obtains the boundedness of the second derivatives of v^*_n on compact sets. Thus, by Ascoli theorem $v^*_n \to V^*$ (for a subsequence still called v^*_n) in $\mathcal{C}^2_{loc}(\mathbb{R}^2, \mathbb{R}^2)$.

   Introducing the rescaled energy

$$E^*(u^*) = \int_{\mathbb{R}^2} \left(\frac{1}{2}|\nabla u^*(s)|^2 - \frac{1}{2}\mu(x_n + \varepsilon_n s)|u^*(s)|^2 + \frac{1}{4}|u^*(s)|^4 - \varepsilon_n a f(x_n + \varepsilon_n s) \cdot u^*(s)\right) \mathrm{d}s,$$

   where $u^*(s) = u_{\varepsilon_n}(x_n + \varepsilon_n s)$. Let ξ^* be a test function with support in the compact K. We have:

$$E^*(v^*_n + \xi^*, K) \geq E^*(v^*_n, K),$$

   and at the limit:

$$G_0(V^* + \xi^*, K) \geq G_0(V^*, K),$$

   where:

$$G_0(\varphi, K) = \int_K \left[\frac{1}{2}|\nabla\varphi|^2 - \frac{1}{2}\mu(x_0)|\varphi|^2 + \frac{1}{4}|\varphi|^4\right],$$

   or equivalently $G(V^* + \xi^*, K) \geq G(V^*, K)$, where:

$$G(\varphi, K) = G_0 + \int_K \frac{(\mu(x_0))^2}{4} = \int_K \left[\frac{1}{2}|\nabla\varphi|^2 + \frac{1}{4}(|\varphi|^2 - \mu(x_0))^2\right].$$

Thus, we deduce that V^* is a bounded minimal solution of the P.D.E. associated with the above functional:

$$\Delta V^*(s) + (\mu(x_0) - |V^*(s)|^2)V^*(s) = 0. \tag{7.7}$$

Condition (5.5) excludes constant solutions. Therefore, up to orthogonal transformations: $V^*(s) = \sqrt{\mu(x_0)}\eta(\sqrt{\mu(x_0)}(s - s_0))$, where $s \in \mathbb{R}^2$ and $\eta(s)$ is the radial vortex solution to the Ginzburg-Landau equation:

$$-\Delta\eta = (1 - |\eta|^2)\eta.$$

Then, by $\mathcal{C}^1_{loc}(\mathbb{R}^2, \mathbb{R}^2)$ convergence, v_n^* has a zero in $D_n \subset \Omega$, which for $\varepsilon_n \ll 1$ contradicts the fact that $v_\varepsilon \neq 0$ on Ω.

2. For every $\xi = \rho e^{i\theta}$, we consider de local coordinates $s = (s_1, s_2)$ in the basis $(e^{i\theta}, ie^{i\theta})$ and rescale the global minimizer by setting $v^*_{\varepsilon,a}(s) = \frac{v_{\varepsilon,a}(\xi + s\varepsilon^{2/3})}{\varepsilon^{1/3}}$. Clearly $\Delta v(s) = \varepsilon\Delta(\xi + s\varepsilon^{2/3})$, thus,

   $$\Delta v^*(s) + \frac{\mu(\xi + s\varepsilon^{2/3})}{\varepsilon^{2/3}} v^*(s) - |v^*(s)|^2 v^*(s) + af(\xi + s\varepsilon^{2/3}) = 0, \qquad \forall s \in \mathbb{R}^2.$$

   Writing $\mu(\xi + h) = \mu_1 h_1 + h \cdot A(h)$, with $\mu_1 = \mu'_{rad}(\rho) < 0$, $A \in \mathcal{C}^\infty(\mathbb{R}^2.\mathbb{R}^2)$ and $A(0) = 0$, we obtain:

   $$\Delta v^*(s) + (\mu_1 s_1 + A(s\varepsilon^{2/3}) \cdot s)v^*(s) - |v^*(s)|^2 v^*(s) + af(\xi + s\varepsilon^{2/3}) = 0, \qquad \forall s \in \mathbb{R}^2. \tag{7.8}$$

   Defining the rescaled energy by:

   $$E^*(u^*) = \int_{\mathbb{R}} \left(\frac{1}{1}|\nabla u^*(s)|^2 - \frac{\mu(\xi + s\varepsilon^{2/3})}{2\varepsilon^{2/3}} u^*(s) + \frac{1}{4}|u^*|^4(s) - af(\xi + s\varepsilon^{2/3}) \cdot u^*(s) \right) \mathrm{d}s.$$

   We have that $E^*(u^*) = \frac{1}{\varepsilon^{2/3}} E(u)$. From Lemma () and (5.8), it follows that Δv^* and ∇v^* are uniformly bounded on compact sets; and by differentiating (5.8) follows the boudedness of the second derivatives of v^*. Aplying the Ascoli theorem via a diagonal argument $v^* \to V^*$ in $\mathcal{C}^2_{loc}(\mathbb{R}^2, \mathbb{R}^2)$ (up to a subsequence), where V^* is a minimal solution of the P.D.E. :

   $$\Delta V^*(s) + \mu_1 s_1 V^*(s) - |V^*|^2(s) V^*(s) + a_0 f(\xi) = 0, \forall s \in \mathbb{R}^2, \text{with } a_0 = \lim_{\varepsilon \to 0} a(\varepsilon). \tag{7.9}$$

   which is associated with the functional

   $$E^*_0(\varphi, J) = \int_J \left(\frac{1}{2}|\nabla\varphi(s)|^2 - \frac{\mu_1}{2} s_1 |\varphi|^2(s) + \frac{1}{4}|\varphi|^4(s) - a_0 f(\xi) \cdot \varphi(s) \right) \mathrm{d}s.$$

   Setting $y(s) = \frac{1}{\sqrt{2}(-\mu_1)^{1/3}} V^*\left(\frac{s}{(-\mu_1)^{1/3}}\right)$, (5.9) reduces to (5.) with $\alpha = \frac{a_0 f(\xi)}{\sqrt{2}\mu_1}$, and y is still a minimal solution of (5.)

3. For every $x_0 = r_0 e^{i\theta_0}$ fixed, with $r_0 > \rho$, we consider the local coordinates $s = (s_1, s_2)$ in the basis $(e^{i\theta_0}, ie^{i\theta_0})$, and the rescaled maps $v^*_{\varepsilon,a}(s) = \frac{v_{\varepsilon,a}(x_0+\varepsilon s)}{\varepsilon}$, satisfying:

$$\Delta v^*(s) + \mu(x_0 + \varepsilon s)v^*(s) - \varepsilon^2|v^*(s)|^2 v^*(s) + af(x_0 + \varepsilon s) = 0, \forall s \in \mathbb{R}^2.$$

By Lemma () and (5.10) the first derivatives of $v^*_{\varepsilon,a}$ are uniformly bounded on compact sets for $\varepsilon \ll 1$, and by differentiating (5.10), one can also obtain the boundedness of the second derivatives of v^* on compact sets. As a consequence, we conclude that $\lim_{\varepsilon\to 0, a\to a_0} v^*_{\varepsilon,a}(s) = V^*(s)$ in $\mathcal{C}^2_{loc}$, where $V^*(s) = -\frac{a_0}{\mu_{rad}(r_0)} f(r_0 e^{i\theta_0})$ is the unique bounded solution of

$$\Delta V^*(s) + \mu(x_0)V^*(s) + a_0 f(x_0) = 0, \forall s \in \mathbb{R}^2. \tag{7.10}$$

Indeed, consider a smooth and bounded solution $u : \mathbb{R}^2 \to \mathbb{R}^2$ of $\Delta u = \nabla W(u)$ where the potential $W : \mathbb{R}^2 \to \mathbb{R}$ is smooth and strictly convex. Then, we have $\Delta(W(u)) = |\nabla W(u)|^2 + \sum_{i=1}^2 D^2W(u)(u_{x_i}, u_{x_i}) \geq 0$, and since $W(u)$ is bounded we deduce that $W(u)$ is constant. Therefore, $u = u_0$, where $u_0 \in \mathbb{R}^2$ is such that $\nabla W(u_0) = 0$.
Finally, the uniform convergence $\lim_{\varepsilon\to 0, a\to a_0} \frac{u_{\varepsilon,a}((r_0+t\varepsilon)e^{i\theta})}{\varepsilon} = -\frac{a_0}{\mu_{rad}(r_0)} f(r_0 e^{i\theta})$ when t remains bounded and $\theta \in \mathbb{R}$ follows from the invariance of equation (5.1) under the transformation $u(x) \mapsto g^{-1}u(gx)$, $\forall g \in SO(2)$.

Remark When $\mu(x) < 0$, $\forall x$, we can use the same argument for every $x_0 = r_0 e^{i\theta_0}$ with $r_0 > 0$ and obtain formally the Rayleigh vortex solution of chapter 4.

7.4 Proof Theorem 5.3

1. Let $x_0 \in \mathbb{R}^2$ be such that $v(x_0) \neq 0$. Without loss of generality, we may assume that $v(x_0) = (v_1(x_0), 0)$ is contained in the open right half-plane $P = \{x_1 > 0\}$. Next, consider $v^* = (|v_1|, v_2)$ which is another global minimizer. Clearly, in a sufficiently small disc $D \subset P$ centred at $v(x_0)$ we have $v_1 = |v_1| > 0$, and as a consequence of the unique continuation principle, we deduce that $v = v^*$ on $\mathbb{R}^2 \Rightarrow v(\mathbb{R}^2) \subset \bar{P}$. Since the same conclusion holds for any open half-plane containing $v(x_0)$, we also obtain $v(\mathbb{R}^2) \subset \{\lambda v(x_0 : \lambda \geq 0)\}$. As a consequence, we have $v = (v_1, 0)$ with $v_1 \geq 0$ and $\varepsilon^2 \Delta v_1 + \mu v_1 - v_1^3 = 0$. By the maximum principle, it follows that $v_1 > 0$ since $v_1 \neq 0$.

   Now to prove that v_1 is radial consider the reflection with respect to the line $x_1 = 0$. We can check that $E(v, \{x_1 > 0\}) = E(v, \{x_1 < 0\})$, since otherwise by even reflection we can construct a map in H^1 with energy smaller than v. Thus, the map $v^*(x) = v(|x_1|, x_2)$ is also a minimizer, and since $v^* = v$ on $\mathbb{R}^2$. Repeating the same argument for any line of reflection, we can deduce that v_1 is radial. To complete the proof, it remains to show the uniqueness of v up to rotations. Let $v^* = (v_1^*, 0)$ be another global minimizer with $v_1^* > 0$ and $v_1^* \neq v_1$. Considering the weak formulation of (5.1):

$$\int_{\mathbb{R}^2} -\varepsilon^2 \sum_j \nabla u_j \nabla \varphi_j + \mu u \cdot \varphi - |u|^2 u \cdot \varphi + \varepsilon a f \cdot \varphi, \quad \forall \varphi \in H^1(\mathbb{R}^2, \mathbb{R}^2). \tag{7.11}$$

Evaluating in $\varphi = v$:

$$\int_{\mathbb{R}^2} -\varepsilon^2|\nabla v|^2 + \mu|v|^2 - |v|^4 = 0 \Rightarrow E(v) = -\int_{\mathbb{R}^2} \frac{1}{4\varepsilon^2}|v|^4,$$

we obtain an alternative expression of the energy that holds for every solution of (5.1) beloging to H^1. In particular, this formula implies that v_1 and v_1^* intersect for $|x| = r > 0$. However, setting:

$$w(x) = \begin{cases} v(x) & \text{for } |x| \leq r \\ v^*(x) & \text{for } |x| \geq r \end{cases}$$

we can see that w is another global minimizer, and again by the unique continuation principle, we have $w = v = v^*$.

2. We need first to establish the following three Lemmas:

Lemma 7.9 *If u is a solution of (5.1) belonging to $H^1(\mathbb{R}^2, \mathbb{R}^2)$, then for every $\varphi \in H^1(\mathbb{R}^2, \mathbb{R}^2)$, we have:*

$$E(u+\varphi) - E(u) = \int_{\mathbb{R}^2} \left(\frac{1}{2}|\nabla\varphi|^2 + \frac{(|u|^2 - \mu)}{2\varepsilon^2}|\varphi|^2 + \frac{(|\varphi|^2 + 2(u\cdot\varphi))^2}{4\varepsilon^2} \right). \qquad (7.12)$$

Proof. From the weak formulation (5.11):

$$\int_{\mathbb{R}^2} \left(\sum_{j=1,2} \nabla\varphi_j \cdot \nabla u_j \right) = \int_{\mathbb{R}^2} \left(\frac{\mu}{\varepsilon^2}\varphi\cdot u - \frac{|u|^2\varphi\cdot u}{\varepsilon^2} + \frac{a}{\varepsilon} f\cdot\varphi \right). \qquad (7.13)$$

On the other hand, we have the identity

$$\int_{\mathbb{R}^2} \left(\frac{1}{2}|\nabla\varphi + \nabla u|^2 + \frac{1}{2}|\nabla u|^2 - \sum_{j=1,2} (\nabla\varphi_j + \nabla u_j)\cdot\nabla u_j \right) = \int_{\mathbb{R}^2} \frac{1}{2}|\nabla\varphi|^2. \qquad (7.14)$$

Adding (5.13) and (5.14), we obtain

$$\int_{\mathbb{R}^2} \frac{1}{2}\left(|\nabla(\varphi+u)|^2 - |\nabla u|^2\right) = \underbrace{\int_{\mathbb{R}^2} \left(\frac{1}{2}|\nabla\varphi|^2 - \frac{\mu}{\varepsilon^2}\varphi\cdot u - \frac{|u|^2\varphi\cdot u}{\varepsilon^2} + \frac{a}{\varepsilon} f\cdot\varphi \right)}_{=B}, \qquad (7.15)$$

and thus

$$\begin{aligned} E(u+\varphi) - E(u) &= B + \int_{\mathbb{R}^2} \left(-\frac{\mu}{2\varepsilon^2}(|u+\varphi|^2 - |u|^2) + \frac{1}{4\varepsilon^2}(|u+\varphi|^4 - |u|^4) - \frac{a}{\varepsilon} f\cdot\varphi \right) \\ &= \int_{\mathbb{R}^2} \left(\frac{1}{2}|\nabla\varphi|^2 + \frac{(|u|^2-\mu)}{2\varepsilon^2}|\varphi|^2 + \frac{(|\varphi|^2 + 2(u\cdot\varphi))^2}{4\varepsilon^2} \right). \end{aligned}$$

□

Lemma 7.10 *For every $a > 0$, let $\mu_a : \mathbb{R}^2 \to \mathbb{R}$ be a measurable function satisfying $\mu_a \leq \mu$, and $\lim_{a\to\infty} \mu_a = -\infty$ a.e, then given $\varepsilon > 0$ there exists $A > 0$ such that for every $a > A$:*

$$\int_{\mathbb{R}^2} \mu_a |\varphi|^2 < \varepsilon^2 \int_{\mathbb{R}^2} |\nabla\varphi|^2, \qquad \forall\varphi \in H^1(\mathbb{R}^2, \mathbb{R}^2), \varphi \neq 0. \tag{7.16}$$

Proof. By homegeneity, it is suffiecient to prove for $\|\varphi\|_{H^1} = 1$. Suppose by contradiction that (5.16) does not hold. Then, there exist a constant $C_0 > 0$, a sequence $a_n \to \infty$, and a sequence $\varphi_n \in H^1(\mathbb{R}^2, \mathbb{R}^2)$, with $\|\varphi\|_{H^1} = 1$, such that:

$$\int_{\mathbb{R}^2} \mu_{a_n} |\varphi_n|^2 \geq C_0 \int_{\mathbb{R}^2} |\nabla\varphi_n|^2. \tag{7.17}$$

Since $\|\varphi_n\|_{H^1}$ is bounded, we can extract a subsequence, still called φ_n, such that, $\varphi_n \rightharpoonup \Phi$ weakly in H^1, and $\varphi_n \to \Phi$ in L^2_{loc}. Writing

$$C_0 \int_{\mathbb{R}^2} |\nabla\varphi_n|^2 \leq \int_{\mathbb{R}^2} \mu_{a_n} |\varphi_n|^2 \leq \int_{I_\delta} \max{(\mu_{a_n}, 0)} |\varphi_n|^2,$$

where $I_\delta = \{x \in \mathbb{R}^2 : \mu(x) > -\delta\}$ and $\delta > 0$ is small, we see that:

$$\lim_{n\to\infty} \int_{\mathbb{R}^2} |\nabla\varphi_n^2| = 0.$$

This implies by lower semicontinuity that $\int_{\mathbb{R}^2} |\nabla\Phi|^2 \leq \liminf \int_{\mathbb{R}^2} |\nabla\varphi_n|^2 = 0$, hence $\Phi = 0$. In addition, we have $\lim_{n\to\infty} \int_{\mathbb{R}^2} |\varphi_n^2| = 1$, $\lim_{n\to\infty} \int_{I_\delta} |\varphi_n^2| = 0$, and $\lim_{n\to\infty} \int_{\mathbb{R}^2 \setminus I_\delta} |\varphi_n^2| = 1$. As a consequence

$$\int_{\mathbb{R}^2} \mu_{a_n} |\varphi_n|^2 \leq \|\mu\|_{L^\infty} \int_{I_\delta} |\varphi_n|^2 - \delta \int_{\mathbb{R}^2 \setminus I_\delta} |\varphi_n|^2,$$

and taking the limit we find that $\int_{\mathbb{R}^2} \mu_{a_n} |\varphi_n|^2 \leq -\frac{\delta}{2}$, for n big enough, which contradicts (5.17) □

Lemma 7.11 *For $\varepsilon > 0$ and $x_0 \in \mathbb{R}^2$ fixed, the global minimizer satisfy*

$$\lim_{a\to\infty} a^{-1/3} v_{\varepsilon,a}(x_0 + a^{-1/3}s) = \frac{\varepsilon^{1/3} f(x_0)}{|f(x_0)|^{2/3}}. \tag{7.18}$$

in the $\mathcal{C}^2_{loc}(\mathbb{R}^2, \mathbb{R}^2)$

Proof. Considering the rescaled map $v^*(s) = a^{-1/3} v(x_0 + a^{-1/3}s)$, satisfying:

$$\varepsilon^2 \Delta v^*(s) + a^{-2/3} \mu(x_0 + a^{-1/3}s) v^*(s) - |v^*|^2(s) v^*(s) + \varepsilon f(x_0 + a^{-1/3}s) = 0, \forall s \in \mathbb{R}^2$$

Repeating the arguments used in the proof of Lemaa, when ε is fixed and $\frac{1}{a}$ remains bounded, the maps $v^*_{\varepsilon,a}$ are uniformly bounded up to second derivatives. Therefore, proceeding as before, it is possible to deduce the convergence of v^* as $a \to \infty$ to the unique bounded solution of:

$$\varepsilon^2 \Delta V^*(s) - |V^*(s)| V^*(s) + \varepsilon f(x_0) = 0, \forall s \in \mathbb{R}^2,$$

which is the constant $V^* = \frac{\varepsilon^{1/3} f(x_0)}{|f(x_0)|^{2/3}}$. □

Now, to prove the second part of Theorem 5.3 let $\varepsilon > 0$ be fixed and let $\mu_a = \mu - |v|^2$, where $v = v_{\varepsilon,a}$ is a global minimizer. By the previous lemma, we know that for every $x \neq 0$, $\mu_a(x)$ converges pointwise to $-\infty$, as $a \to \infty$. Thus, by Lemma 5.10, there exists $A > 0$, such that for every $a > A$ we have

$$\int_{\mathbb{R}^2} \left(\frac{1}{2}|\nabla\varphi|^2 + \frac{(|v|^2 - \mu)}{2\varepsilon^2}|\varphi|^2 \right) > 0, \qquad \forall\varphi \in H^1(\mathbb{R}^2, \mathbb{R}^2), \varphi \neq 0.$$

and also by Lemma 5.9 $E(v + \varphi) > E(v)$. In particular, it follows that when $a > A$, the global minimizer is unique and radial, since $v = g^{-1}vg$, $\forall g \in O(2)$

Summarizing the previous results in 2 cases, we have:

- For $\mu \in L^\infty(\mathbb{R}^2, \mathbb{R})$, $\mu'_{rad} < 0$ in $(0, \infty)$, and $\mu_{rad}(\rho) = 0$ for a unique $\rho > 0$:
  When $a = 0$ the global minimizer is radially symmetric and unique and its symmetry is instantly broken as $a > 0$ and then restored for sufficiently large values of a. Symmetry breaking is associated with the presence of a new type of topological defect, namely the *shadow vortex* discussed in Chapter 3. This symmetry breaking scenario is a rigorous confirmation of experimental and numerical results obtained by Barboza and Clerc. []
- For $\mu \in L^\infty(\mathbb{R}^2, \mathbb{R})$, $\mu_{rad}(r) < 0, \forall r$:
  When $a = 0$ the global minimizer is the identically null function $v = 0$, and when $a > 0$ and $\lim_{\varepsilon\to 0} a(\varepsilon) = a_0$ the global minimizer is radially symmetric and coincides with the *Rayleigh vortex solution* discussed in Chapter 4.

Conclusion

The results obtained in this thesis describes analytically the origin of the vortex lattices by means of the **Rayleigh vortex** solution below the Frédericksz transition. When the system is above the molecular reorientation transition, the Rayleigh vortex does not account for the observed vortices. However, the position and configuration of the vortex lattices are qualitatively described by the lattices of the Rayleigh vortices. The amplitude equations describe qualitatively and quantitatively the dynamics near the instability point. However, these equations quantatively describe the dynamics away from the bifurcation point []. Hence, the results and findings of this work are valid far from the Fréedericksz transition.

At the onset of the Fréedericksz transition, depending on the light intensity, the vortices positioned at the center of the light beam can undergo instabilities and move to dark areas (the area outside the illuminated region). These new topological defects known as *shadow vortices* [] are characterized by having an exponentially small height. Experimentally they are detected indirectly. The lattice created by these and the induced vortices is a problem currently in progress.

By using an appropriate magnetic field arrangement in a nematic LC with homeotropic geometry, we experimentally demonstrated a controlled vortex induction, which is, at the same time, low cost, positionally stable and that allows direct observation of the induced vortices. This suggests possible practical advantages in the experimental development of optical devices.

Bibliography

[1] L.M. Pismen. *Vortices in nonlinear fields.* Oxford Science Publications, New York, 1999.

[2] S. Chandrasekhar. *Liquid Crystals.* Cambridge University Press, 2 edition, 1992.

[3] A. Rapini. Umbilics : static properties and shear-induced displacements. *Journal de Physique*, 34:629–633, 1973.

[4] M. S. Soskin and M. V. Vasnetsov. Chapter 4 Singular optics. *Progess in Optics*, 42:219–276, 2001.

[5] Y. S. Desyatnikov, A. S. Kivshar and L Torner. Optical Vortices and Vortex Solitons. *Progess in Optics*, 47:291, 2005.

[6] L. Allen, M. W. Beijersbergen, R. J. C. Spreeuw, and J. P. Woerdman. Orbital angular momentum of light and the transformation of laguerre-gaussian laser modes. *Phys. Rev. A*, 45:8185–8189, Jun 1992.

[7] D. G. Grier. A revolution in optical manipulation. *Nature*, 424:810, 2003.

[8] Vladlen G. Shvedov, Andrei V. Rode, Yana V. Izdebskaya, Anton S. Desyatnikov, Wieslaw Krolikowski, and Yuri S. Kivshar. Giant optical manipulation. *Phys. Rev. Lett.*, 105:118103, Sep 2010.

[9] H. H. Arnaut and G. A. Barbosa. Orbital and intrinsic angular momentum of single photons and entangled pairs of photons generated by parametric down-conversion. *Phys. Rev. Lett.*, 85:286–289, Jul 2000.

[10] F. Tamburini, G. Anzolin, G. Umbriaco, A. Bianchini, and C. Barbieri. Overcoming the rayleigh criterion limit with optical vortices. *Phys. Rev. Lett.*, 97:163903, Oct 2006.

[11] Peng Chen, Shi-Jun Ge, Ling-Ling Ma, Wei Hu, Vladimir Chigrinov, and Yan-Qing Lu. Generation of equal-energy orbital angular momentum beams via photopatterned liquid crystals. *Phys. Rev. Applied*, 5:044009, Apr 2016.

[12] I. M. Fazal N. Ahmed Y. Yan H. Huang Y. Ren Y. Yue S. Dolinar M. Tur . Wang, J.-Y. Yang and A. E. Willner. Terabit free-space data transmission employing orbital angular momentum multiplexing. *Nature Photon*, 6:488, 2012.

[13] R. Barboza, U. Bortolozzo, G. Assanto, E. Vidal-Henriquez, M. G. Clerc, and S. Residori. Harnessing optical vortex lattices in nematic liquid crystals. *Phys. Rev. Lett.*, 111:093902, Aug 2013.

[14] R. Barboza, U. Bortolozzo, G. Assanto, E. Vidal-Henriquez, M. G. Clerc, and S. Residori. Vortex induction via anisotropy stabilized light-matter interaction. *Phys. Rev. Lett.*, 109:143901, Oct 2012.

[15] R. Barboza, U. Bortolozzo, M. G. Clerc, S. Residori, and E. Vidal-Henriquez. Optical vortex induction via light-matter interaction in liquid-crystal media. *Adv. Opt. Photon.*, 7(3):635–683, Sep 2015.

[16] D. J. Thouless. Long-range order in one-dimensional ising systems. *Phys. Rev.*, 187:732–733, Nov 1969.

[17] V. L. Berezinsky. Destruction of long range order in one-dimensional and two-dimensional systems having a continuous symmetry group. I. Classical systems. *Sov. Phys. JETP*, 32:493–500, 1971. [Zh. Eksp. Teor. Fiz.59,907(1971)].

[18] Scientific Background on the Nobel Prize in Physics 2016 Topological phase transitions and topological phases of matter. `https://www.nobelprize.org/uploads/2018/06/advanced-physicsprize2016-1.pdf`.

[19] N. D. Mermin. The topological theory of defects in ordered media. *Rev. Mod. Phys.*, 51:591–648, Jul 1979.

[20] Jan Wehr, Armand Niederberger, Laurent Sanchez-Palencia, and Maciej Lewenstein. Disorder versus the mermin-wagner-hohenberg effect: From classical spin systems to ultracold atomic gases. *Phys. Rev. B*, 74, 05 2006.

[21] L.D Landau and E.M. Lifshitz. *Statistical Physics.(Course of Theoretical Physics, Volume 5).* Pergamon Press, Oxford, 1959.

[22] D. J. Bishop and J. D. Reppy. Study of the superfluid transition in two-dimensional ^{4}He films. *Phys. Rev. Lett.*, 40:1727–1730, Jun 1978.

[23] K. Epstein, A. M. Goldman, and A. M. Kadin. Vortex-antivortex pair dissociation in two-dimensional superconductors. *Phys. Rev. Lett.*, 47:534–537, Aug 1981.

[24] D. J. Resnick, J. C. Garland, J. T. Boyd, S. Shoemaker, and R. S. Newrock. Kosterlitz-thouless transition in proximity-coupled superconducting arrays. *Phys. Rev. Lett.*, 47:1542–1545, Nov 1981.

[25] Z. S. Sacks, D. Rozas, and G. A. Swartzlander. Holographic formation of optical-vortex filaments. *J. Opt. Soc. Am. B*, 15(8):2226–2234, Aug 1998.

[26] M.W. Beijersbergen, L. Allen, H.E.L.O. van der Veen, and J.P. Woerdman. Astigmatic laser mode converters and transfer of orbital angular momentum. *Optics Communications*, 96(1):123 – 132, 1993.

[27] S Residori. Patterns, fronts and structures in a liquid-crystal-light-valve with optical feedback. *Physics Reports-review Section of Physics Letters - PHYS REP-REV SECT PHYS LETT*, 416:201–272, 09 2005.

[28] P.G De Gennes and J. Prost. *The Physics of Liquid Crystals.* Clarendon Press, Oxford, 1993.

[29] Denis Andrienko. Introduction to liquid crystals. *Journal of Molecular Liquids*, 267:520 – 541, 2018. Special Issue Dedicated to the Memory of Professor Y. Reznikov.

[30] D.V. Anosov and V.I. Arnold. *Dynamical Systems: Bifurcation theory and catastrophe theory.* Encyclopaedia of mathematical sciences. Springer-Verlag, 1994.

[31] S. Wiggins. *Introduction to Applied Nonlinear Dynamical Systems and Chaos.* Texts in Applied Mathematics. Springer New York, 2003.

[32] Yuri Kuznetsov. *Elements of applied bifurcation theory.* Springer Science & Business Media, 2013.

[33] H. Poincaré. Sur l'équilibre d'une masse fluide animée d'un mouvement de rotation. *Acta Math.*, 7:259–380, 1885.

[34] Edgar Knobloch and Kurt Wiesenfeld. Bifurcations in fluctuating systems: The center-manifold approach. *Journal of Statistical Physics*, 33:611–637, 12 1983.

[35] Tanmay Vachaspati. *Kinks and Domain Walls: An Introduction to Classical and Quantum Solitons.* Cambridge University Press, 2006.

[36] Hermann Riecke. Ginzburg-landau equation coupled to a concentration field in binary-mixture convection. *Physica D: Nonlinear Phenomena*, 61(1):253 – 259, 1992.

[37] Amandine Aftalion. *Vortices in Bose-Einstein Condensates.* Birkhauser Boston, 2006.

[38] H. Bethuel, F. Brezis and F. Helein. *Ginzburg-Landau Vortices.* Modern Birkhauser Classics, 2017.

[39] Yu N Ovchinnikov and I M Sigal. The ginzburg-landau equation III. vortex dynamics. *Nonlinearity*, 11(5):1277–1294, sep 1998.

[40] E. Sandier and S. Serfaty. *Vortices in the Magnetic Ginzburg-Landau Model.* Progress in Nonlinear Differential Equations and Their Applications. Birkhauser Basel, 2007.

[41] Rose-Marie Hervé and Michel Hervé. Etude qualitative des solutions reelles d'une equation differentielle liee a l'equation de ginzburg-landau. In *Annales de l'Institut Henri Poincare (C) Non Linear Analysis*, volume 11, pages 427–440. Elsevier, 1994.

[42] Yuri N Ovchinnikov and Israel M Sigal. Ginzburg-landau equation. i. static vortices. *Partial differential equations and their applications (Toronto, ON, 1995)*, 12:199–220, 1997.

[43] P Mironescu. Local minimizers for the ginzburg-landau equation are radially symmetric. *COMPTES RENDUS DE L ACADEMIE DES SCIENCES SERIE I-MATHEMATIQUE*, 323(6):593–598, 1996.

[44] Marcel G. Clerc, Estefania Vidal-Henriquez, Juan Diego Dávila, and Michał Kowalczyk. Symmetry breaking of nematic umbilical defects through an amplitude equation. *Physical review. E, Statistical, nonlinear, and soft matter physics*, 901:012507, 2014.

[45] V. Fréedericksz and V. Zolina. Forces causing the orientation of an anisotropic liquid. *Trans. Faraday Soc.*, 29:919–930, 1933.

[46] R. Monaco, J. Mygind, M. Aaroe, R. J. Rivers, and V. P. Koshelets. Zurek-kibble mechanism for the spontaneous vortex formation in $\mathrm{Nb}-\mathrm{Al}/\mathrm{al}_{\mathrm{ox}}/\mathrm{Nb}$ josephson tunnel junctions: New theory and experiment. *Phys. Rev. Lett.*, 96:180604, May 2006.

[47] Raouf Barboza, Umberto Bortolozzo, Gaetano Assanto, Estefania Vidal-Henriquez, Marcel G. Clerc, and S. Residori. Harnessing optical vortex lattices in nematic liquid crystals. *Physical review letters*, 111 9:093902, 2013.

[48] E. Vidal Henríquez. Phase singularity dynamics in out of equilibrium anisotropic systems. Master's thesis, Universidad de Chile - Facultad de Ciencias Físicas y Matemáticas, 2015. Disponible en http://repositorio.uchile.cl/handle/2250/132990.

[49] R. Barboza, U. Bortolozzo, M. G. Clerc, S. Residori, and E. Vidal-Henriquez. Light matter interaction induces a single positive vortex with swirling arms. *Philosophical Transactions of the Royal Society A: Mathematical, Physical and Engineering Sciences*, 372(2027):20140019, 2014.

[50] Sedlyarov Igor and Lev Tsimring. Theory of self-assembly of microtubules and motors. *Physical review. E, Statistical, nonlinear, and soft matter physics*, 74:031915, 10 2006.

[51] Lord Rayleigh O.M. F.R.S. Xxxi. on the problem of random vibrations, and of random flights in one, two, or three dimensions. *The London, Edinburgh, and Dublin Philosophical Magazine and Journal of Science*, 37(220):321–347, 1919.

[52] I.C. Khoo. *Liquid Crystals.* Wiley Series in Pure and Applied Optics. Wiley, 2007.

[53] Raouf Barboza, Umberto Bortolozzo, Marcel Clerc, J. Davila, Michal Kowalczyk, S. Residori, and E. Vidal-Henriquez. Light-matter interaction induces a shadow vortex. *Physical Review E*, 93, 05 2016.

[54] Marcel G. Clerc, Michał Kowalczyk, and Panayotis Smyrnelis. Symmetry breaking and restoration in the ginzburg–landau model of nematic liquid crystals. *Journal of Nonlinear Science*, 28(3):1079–1107, Jun 2018.

[55] Marcel G. Clerc, Juan Diego Dávila, Michał Kowalczyk, Panayotis Smyrnelis, and Estefania Vidal-Henriquez. Theory of light-matter interaction in nematic liquid crystals and the second painlevé equation. *Calculus of Variations and Partial Differential Equations*, 56:1–22, 2016.

[56] S Drell. Variational approach to strong couplings field theory-i. phiˆ 4 theory. Technical report, SLAC National Accelerator Lab., Menlo Park, CA (United States), 2018.

[57] J. E. Macías, M. G. Clerc, C. Falcón, and M. A. García-Ñustes. Spatially modulated kinks in shallow granular layers. *Phys. Rev. E*, 88:020201, Aug 2013.

[58] P. Pieranski, B. Yang, L. J. Burtz, A. Camu, and F. Simonetti. Generation of umbilics by magnets and flows. *Liquid Crystals*, 40(12):1593–1608, 2013.

[59] Ivar Fredholm. Sur une classe d'équations fonctionnelles. *Acta Math.*, 27:365–390, 1903.

[60] K. W. Schwarz. Three-dimensional vortex dynamics in superfluid ^{4}He: Line-line and line-boundary interactions. *Phys. Rev. B*, 31:5782–5804, May 1985.

[61] S. Rica and E. Tirapegui. Interaction of defects in two-dimensional systems. *Phys. Rev. Lett.*, 64:878–881, Feb 1990.

[62] L. M. Pismen and J. D. Rodriguez. Mobility of singularities in the dissipative ginzburg-landau equation. *Phys. Rev. A*, 42:2471–2474, Aug 1990.

[63] L. Kramer, E. Bodenschatz, and W. Pesch. Interaction and dynamics of defects in anisotropic pattern-forming systems. *Phys. Rev. Lett.*, 64:2588–2588, May 1990.

[64] H. Brezis. *Functional Analysis, Sobolev Spaces and Partial Differential Equations*. Universitext. Springer New York, 2010.

[65] B.Y. Rubinstein and L.M. Pismen. Vortex motion in the spatially inhomogenous conservative ginzburg-landau model. *Physica D: Nonlinear Phenomena*, 78(1):1 – 10, 1994.

[66] Igor S. Aranson and Lorenz Kramer. The world of the complex ginzburg-landau equation. *Rev. Mod. Phys.*, 74:99–143, Feb 2002.

Appendix A

On the origin of the optical vortex lattices in a nematic liquid crystal light valve

Publication Details

- Title: On the origin of the optical vortex lattices in nematic liquid crystal light valve
- Author: E. Calisto, M.G. Clerc, M. Kowalczyk, and P. Smyrnelis
- Submitted to Optic Letters
- DOI: https://doi.org/10.1364/OL.44.002947

Optics Letters

On the origin of the optical vortex lattices in a nematic liquid crystal light valve

ENRIQUE CALISTO,[1,2] MARCEL G. CLERC,[2,*] MICHAŁ KOWALCZYK,[1] AND PANAYOTIS SMYRNELIS[3]

[1] *Departamento de Física and Millennium Institute for Research in Optics, Facultad de Ciencias Físicas y Matemáticas, Universidad de Chile, Casilla 487-3, Santiago, Chile*
[2] *Departamento de Ingeniería Matemática and CMM, Universidad de Chile, Casilla 170 Correo 3, Santiago, Chile*
[3] *Institute of Mathematics, Polish Academy of Sciences, 00-656 Warsaw, Poland*
**Corresponding author: marcel@dfi.uchile.cl*

Received 29 January 2019; revised 7 May 2019; accepted 9 May 2019; posted 13 May 2019 (Doc. ID 359005); published 3 June 2019

Optical vortices and lattices of these are attracting the attention of the scientific community because of their applications in various fields of optical processing, communications, enhanced imaging systems, and bio-inspired devices. Programmable optical vortices lattices with arbitrary distributions have been achieved using illuminated liquid crystals with photosensitive walls. Using an amplitude equation that describes these optical valves close to the Freédericksz transition allows us to characterize analytically the vortices and the lattices they form. The numerical simulations of the amplitude equation, analytical solutions, and experimental observations show good agreement.

https://doi.org/10.1364/OL.44.002947

Optical vortices are point phase dislocations; that is, they are singular points where the electromagnetic field goes to zero and around which the phase distribution forms an N-armed spiral, with N being the topological charge [1–3]. In the last decade, optical vortices have attracted attention for their diverse photonic applications [4], ranging from the interchange of angular momentum between light and matter [5], optical tweezers [6–8], quantum computation [9], enhancement of astronomical images [10], the generation of optical beams by micro/nano patterned in liquid crystals [11–16], and data transmission [17]. In all these applications, optical vortex lattices are always involved and required, because they contain multiple optical vortices that supply information, flexibility, and manipulation [17–19]. Indeed, the generation, detection, and manipulation of optical vortex lattices are of fundamental relevance in the research described and in future optical applications. The realization of programable lattices of optical vortices with arbitrary distribution in space was demonstrated by exploiting reorientational nonlinearities in the nematic liquid crystal layer of a light valve [20]. The vortex arrangements were determined qualitatively on the basis of consistent topological rules governing light-induced matter defects of both signs. When a liquid crystal light valve is illuminated by a Gaussian beam, a vortex in the molecular orientation (umbilic defect) is induced [21,22]. The umbilical defects are topological charges ±1.

In this Letter, we establish analytically the origin of the vortex lattices observed in illuminated liquid crystal layers with photosensitive walls. Using a topologically driven Ginzburg–Landau equation that describes illuminated liquid crystal light valves close to the Fréedericksz transition, we model the vortices and the lattices they form. Figure 1 shows typical experimental, numerical, and analytical vortex lattices of an illuminated liquid crystal light valve. The numerical simulations of the amplitude equation, analytical solutions, and experimental observations show good agreement.

The liquid crystal light valve is composed of a thin nematic liquid crystal film sandwiched between a glass and a photoconductive plate. The liquid crystal light valve is filled with a nematic mixture exhibiting negative dielectric anisotropy. The transparent interfaces are treated in order to provide a homeotropic alignment of the liquid crystals, that is, close to the walls, the liquid crystal molecules are perpendicular to the confining layers, one of which is the photoconductive slab. The director $\vec{n}(z, x, y, t)$ accounts for the orientational organization of the molecules, where z and $\{x, y\}$, respectively, are the longitudinal and transverse coordinates. Owing to the photoconductive substrate and transparent electrodes, when the liquid crystal light valve is illuminated, the effective voltages $V(z, x, y)$ drop across the liquid crystal layer which acquires a profile proportional to the light intensity $I(x, y)$ on the liquid crystal layer, $V(z, x, y) = z/d[V_0 + \alpha I(x, y)]$ [21]. Where V_0 is the voltage applied to the liquid crystal light valve, d and α are the thickness of the valve and the phenomenological dimensional parameter, respectively, that describe the linear response of the photoconductor.

The elongated molecules of the liquid crystal start to reorient as a result of the torque exerted by the induced electric field and tend to align perpendicularly to it. The homeotropic state, $\vec{n} = \hat{z}$, undergoes an stationary instability for a critical voltage. Indeed, this molecular reorientation instability corresponds to the Fréedericksz transition [23]. Close to this transition, one can use the following ansatz for the amplitude of the critical spatial mode $\vec{n} \approx [u(x, y, t)\sin(\pi z/d), v(x, y, t)\sin(\pi z/d), 1 - (u^2 + v^2)\sin^2(\pi z/d)/2]$. Substituting it in the director

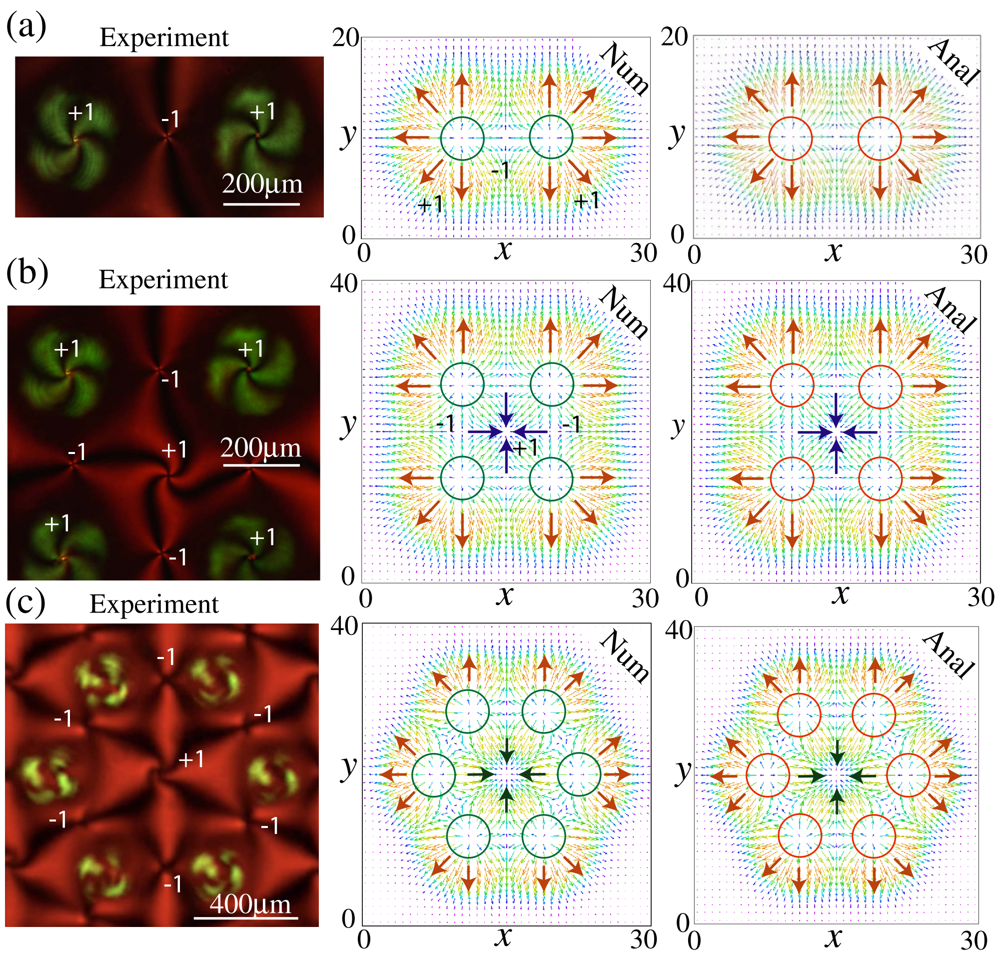

Fig. 1. Optical vortex lattices in nematic liquid crystals. The left panels correspond to snapshots of vortex lattices obtained in an illuminated nematic liquid crystal light valve with (a) two, (b) four, and (c) six light beams (courtesy of R. Barboza). The ±1 account for the respective topological charges. The intermediate panels correspond to the numerical simulations of the topological driven Ginzburg–Landau Eq. (1) with $\mu = -3$, $a = 1$, $\delta = 0$, and $b = 0.1$, forced, respectively with (a) two, (b) four, and (c) six Gaussians beams. The right panels correspond to analytical vortex lattices obtained using formula $A = -4b\nabla_{r_\perp}\langle V\rangle/\alpha$ with (a) two, (b) four, and (c) six Gaussians beams. The circles account for the waist of the respective Gaussian beams.

equation—which contains the effects of elasticity and electromagnetic couplings—integrating in z coordinate over the sample thickness and, considering the complex amplitude $A \equiv (u + iv)$, after straightforward calculations, one obtains the topologically driven Ginzburg–Landau equation [20,21]

$$\gamma\partial_t A = \mu A - aA|A|^2 + \nabla_\perp^2 A + \delta\partial_{\eta\eta}\bar{A} + bI' e^{i\theta}, \qquad (1)$$

where $\mu(r) \equiv -K_3(\pi/d)^2 - \epsilon_a(V_0 + \alpha I)^2/d^2$ is the bifurcation parameter; $a \equiv -[K_3(\pi/d)^2/4 + 3\epsilon_a(V_0 + \alpha I)^2/4d^2] > 0$ is the nonlinear response; $b \equiv 2\epsilon_a d\alpha V_0/\pi$, $\partial_\eta \equiv \partial_x + i\partial_y$, and $\delta \equiv (K_1 - K_2)/(K_1 + K_2)$ stand for the anisotropy elasticity of the system; θ is the amplitude phase; $I' \equiv \sqrt{(\partial_x I)^2 + (\partial_y I)^2}$; γ is the rotational viscosity; and $\{K_1, K_2, K_3\}$ are the elastic anisotropy constants of the liquid crystal.

The numerical simulations of the amplitude Eq. (1) with a forcing term consisting of a superposition of Gaussians equivalent to illuminating the optical valve with several light beams give vortex lattices as a stable equilibrium. The middle panels of Fig. 1 show the typical lattices. Circles account for the waist of the Gaussian forcing. When the liquid crystal light valve is forced with a single beam of sufficiently intense light, it always induces a vortex of positive charge at the center of the beam [22]. This result is easily understood as a consequence of the voltage induced by a single ray being an electric field with a positively charged vortex [21]. Figure 1 shows the vortices induced by a green laser. Illuminating the sample with a red laser, we analyze other areas of response of the optical valve. In the case of two light beams, the positive charges must be accompanied by negative charges, since the total topological charge must be conserved. To characterize analytically the origin of these vortices we assume $\mu < 0$ (i.e., we are below the Fréedericksz transition) and consider a single ray of light with intensity $I = I_0 e^{-r_\perp^2/w^2}$, where I_0 and w, respectively, are the strength and waist of the light beam, and $r_\perp = \sqrt{x^2 + y^2}$ is the radial coordinate with its origin in the center of the beam. When $w \gg 1$, Eq. (1) has the following approximate stationary solution:

$$A_R(r_\perp, \phi) = -\frac{bI'(x,y)}{\mu}e^{i\phi} = \frac{2bI_0}{w^2\mu}r_\perp e^{-r_\perp^2/w^2}e^{i\phi}, \qquad (2)$$

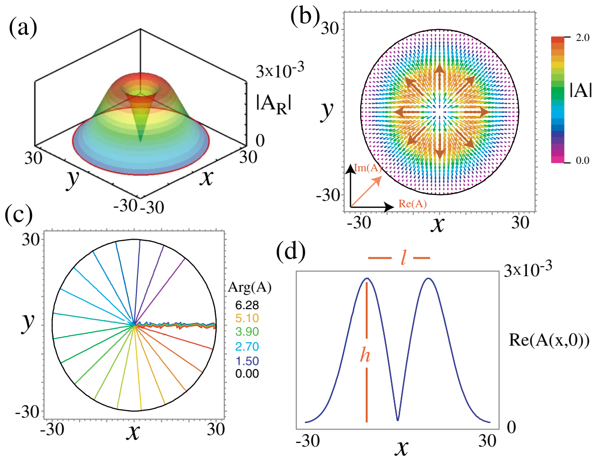

Fig. 2. Rayleigh vortex of the topologically driven Ginzburg–Landau equation (1) with $\mu = -3$, $a = 1$, $\delta = 0$, $b = 1$, $I_0 = 0.01$, and $w = 30$. (a) Surface plot of the Rayleigh vortex, Eq. (2). (b) Vector representation of the vortex solution. The colors show the magnitude of the amplitude $|A|$. (c) Counter-plot of the phase of amplitude A, $\arg(A) = \mathrm{Im}(A)/\mathrm{Re}(A)$. (d) Rayleigh vortex profile; h and l account for the height and width of the core of the vortex, respectively.

where ϕ is the angular coordinate with its origin in the center of the Gaussian. It can be checked that the error of this approximate solution is of the order $O(\frac{1}{w^6})$; in other words, both the nonlinear term and the Laplacian are negligible in this limit. Since $A_R(r_\perp,\phi)$ grows linearly around the origin and decays as a Gaussian, we have called this solution a *Rayleigh vortex*. Figure 2 show the surface plot, vectorial representation, and phase of the Rayleigh vortex. The maximum value h that the vortex reaches corresponds to vortex height, $h = 2bI_0/\mu w\sqrt{2e}$, and the width of the vortex core is $l = w/\sqrt{2}$. Figure 3 shows a comparison between the numerical solutions of the topologically driven Ginzburg–Landau equation (1) and the approximate solution (2). From this figure, we infer that for the light beam of the big waist, the Rayleigh vortex is is a very good approximation of the topologically driven Ginzburg–Landau vortex. For light beam waists of the order one, the effect of the Laplacian and the nonlinear term begins to play a role, and the Rayleigh solution ceases to be dominant. Experimentally, the standard width used for the waist of the light beam (250 μm) is 50 times larger than the length associated with the elastic constant (5 μm), that is, in our dimensionless units $w = 50$. Then, below the Fréedericksz transition, the Rayleigh vortex describes the umbilical defects.

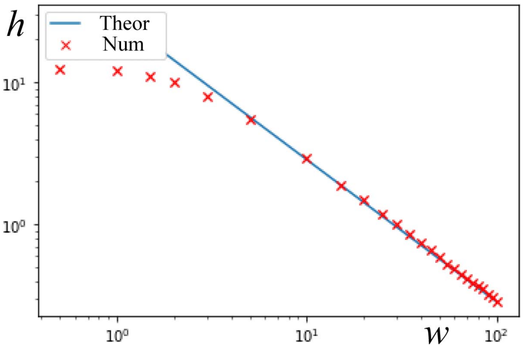

Fig. 3. Log-log plot of the height of the vortex as a function of beam waist w. The heights obtained by numerical simulation of the topologically forced Ginzburg–Landau Eq. (1) (crosses) with $\mu = -3$, $a = 1$, $\delta = 0$, $b = 1$, and $I_0 = 0.01$ are compared with $h = 2bI_0/\mu w\sqrt{2e}$ (continuous line).

To explain the origin of Rayleigh vortex, we note that the liquid crystal light valve is a thin film and, thus, one should consider averaged quantities. The voltage averaged over the thickness $\langle V(r_\perp)\rangle$ takes the form

$$\langle V(r_\perp)\rangle = \frac{1}{d}\int_0^d V(z,r_\perp)\mathrm{d}z = \frac{V_0+\alpha I(r_\perp)}{2}. \qquad (3)$$

Likewise, calculating the electric field averaged in the vertical direction, we obtain $\langle E(r_\perp,\phi)\rangle = -\nabla_{r_\perp}\langle V\rangle = \alpha I_0(r_\perp/2w^2)e^{-r_\perp^2/w^2}e^{i\phi}$, where the electric vector is represented in complex variable notation. Therefore, the Rayleigh vortex is proportional to the averaged electric field or, equivalently the gradient of the averaged potential $A_R(r_\perp,\phi) = 4b\langle E\rangle/\alpha = -4b\nabla_{r_\perp}\langle V\rangle/\alpha$.

Generalizing the previous analysis, one can consider two light beams illuminating the optical light valve in different positions (r_1 and r_2). The averaged potential $\langle V(r_\perp)\rangle = (V_0 + \alpha I(x,y,r_1) + \alpha I(x,y,r_2))/2$, where $I(x,y,r_i)$ is a Gaussian beam centered at r_i, corresponds to a surface with two mounds. Since the equilibrium amplitude is the gradient of the averaged potential, we identify maxima or minima of the potential with positively charged vortices and the saddle points with vortices of negative charge. Figure 4 illustrates this in the case of two Gaussian beams. Note that a negative vortex is located between the positive vortices. By decreasing the

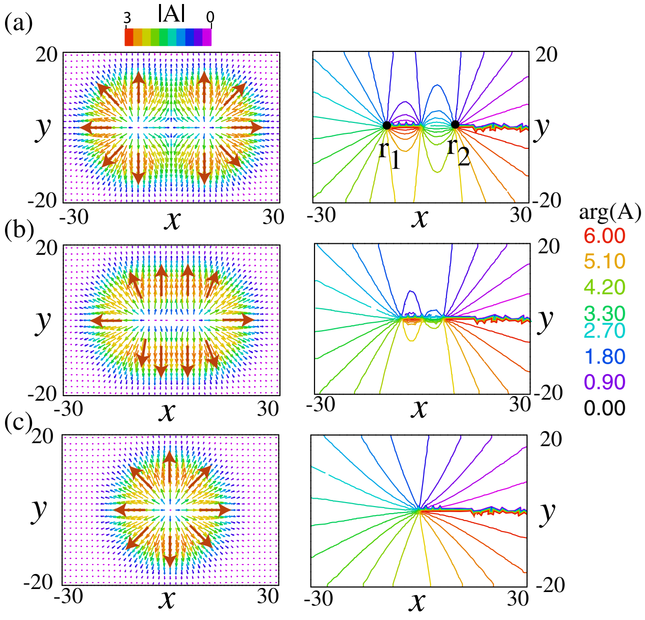

Fig. 4. Analytical vortices induced by two Gaussians. The total topological charge is $N = 1$. The complex amplitude A was obtained using formula $A = -4b\nabla_{r_\perp}\langle V\rangle/\alpha$. The left panels correspond to the vector representation of the complex amplitude. The colors account for the magnitude of the amplitude. The contour plot of the phase of the amplitude is shown on the left panel. (a), (b), and (c) correspond to Gaussians with different distances.

distance between the centers of the Gaussians, the charges approach each other [see Fig. 4(b)]. When this distance is of the order of the beam waist, the vortices merge, leaving a single vortex of positive charge [see Fig. 4(c)]. Based on the same strategy, one can build configurations with more Gaussian beams using the formula $A = -4b\nabla_{r_\perp}\langle V\rangle/\alpha$. Figure 1 (right panels) shows vortex lattices obtained by superposing two, four, and six equally spaced Gaussian beams. An excellent agreement is observed with the vortex lattices obtained by numerical simulations of the topologically driven Ginzburg–Landau equation (1). Likewise, there is excellent agreement with the experimental observations. However, due to the anisotropic effects that are not accounted for in the Rayleigh vortex approximation, the experimental positive vortices exhibit swirling arms [24]. Note that in the case of four light beams, the averaged potential has four saddle points on the sides of the square formed by the maxima and a minimum on the intersection of the diagonals. This explains why in the experiment a swirling vortex is induced on the diagonal between the topologically forced vortices [see the left panels of Figs. 1(b) and 1(c)].

In conclusion, we have been able to establish analytically the origin of the vortex lattices observed in illuminated liquid crystal layers with photosensitive walls below the Fréedericksz transition. The numerical simulations of the amplitude equation, analytical solutions, and experimental observations show good agreement. When the system is above the molecular reorientation transition, the elastic couplings (taken into account in (1) by the Laplacian and the second-order differential operator describing anisotropic spatial variations with $\delta \neq 0$) determine the vortex core size, which is now of the order of few microns. In this regime, the Rayleigh vortex does not account for the observed vortices. However, the position and configuration of the vortex lattices are qualitatively described by the lattices of the Rayleigh vortices. The amplitude equations describe qualitatively and quantitatively the dynamics near the instability point. However, these equations qualitatively describe the dynamics away from the bifurcation point [2,25]. Hence, analytically presented findings are valid far from the Fréedericksz transition.

At the onset of the Fréedericksz transition, depending on the light intensity, the vortices positioned in the center of the light beam can undergo instabilities and move to dark areas (the area outside the illuminated region). These new topological defects known as the *shadow vortices* [26] are characterized by having an exponentially small height. Experimentally they are detected indirectly. The lattice created by these and the induced vortices is a problem currently in progress.

Funding. Millennium Institute for Research in Optics; Fondecyt (1130126, 1170164, 1180903, 3160055); CONICYT Becas Magister Nacional 2017 (22171924); Fondo Basal CMM-Chile (AFB170001); Narodowe Centrum Nauki (NCN) (2017/26/E/ST1/00817).

Acknowledgment. The authors thank R. Barboza, C. Castillo, V. Zambra, and M. Ferre for fruitful discussions. E. Calisto acknowledges the financial support of CONICYT through Becas Magister Nacional 2017. M. Kowalczyk was partially supported by Chilean research grants Fondecyt and Fondo Basal CMM-Chile. P. Smyrnelis was partially supported by Fondo Basal CMM-Chile, Fondecyt postdoctoral, and the National Science Centre, Poland.

REFERENCES

1. J. F. Nye and M. V. Berry, Proc. R. Soc. London A **336**, 165 (1974).
2. L. M. Pismen, *Vortices in Nonlinear Fields* (Oxford Science, 1999).
3. M. S. Soskin and M. V. Vasnetov, *Progress in Optics*, E. Wolf, ed. (Elsevier, 2001), Vol. **42**, p. 219.
4. A. S. Desyatnikov, Y. S. Kivshar, and L. Torner, *Progress in Optics*, E. Wolf, ed. (Elsevier, 2005), Vol. **47**, p. 291.
5. L. Allen, M. W. Beijersbergen, R. J. C. Spreeuw, and J. P. Woerdman, Phys. Rev. A **45**, 8185 (1992).
6. D. G. Grier, Nature **424**, 810 (2003).
7. V. G. Shvedov, A. V. Rode, Y. V. Izdebskaya, A. S. Desyatnikov, W. Krolikowski, and Y. S. Kivshar, Phys. Rev. Lett. **105**, 118103 (2010).
8. M. Padgett and R. Bowman, Nat. Photonics **5**, 343 (2011).
9. H. H. Arnaut and G. A. Barbosa, Phys. Rev. Lett. **85**, 286 (2000).
10. F. Tamburini, G. Anzolin, G. Umbriaco, A. Bianchini, and C. Barbieri, Phys. Rev. Lett. **97**, 163903 (2006).
11. Z. G. Zheng, C. L. Yuan, W. Hu, H. K. Bisoyi, M. J. Tang, Z. Liu, P. Z. Sun, W. Q. Yang, X. Q. Wang, D. Shen, Y. Li, F. Ye, Y. Q. Lu, G. Li, and Q. Li, Adv. Mater. **29**, 1703165 (2017).
12. P. Chen, L. L. Ma, W. Duan, J. Chen, S. J. Ge, Z. H. Zhu, M. J. Tang, R. Xu, W. Gao, T. Li, W. Hu, and Y. Q. Lu, Adv. Mater. **30**, 1705865 (2018).
13. B. Y. Wei, W. Hu, Y. Ming, F. Xu, S. Rubin, J. G. Wang, V. Chigrinov, and Y. Q. Lu, Adv. Mater. **26**, 1590 (2013).
14. B. Y. Wei, S. Liu, P. Chen, S. X. Qi, Y. Zhang, W. Hu, Y. Q. Lu, and J. L. Zhao, Appl. Phys. Lett. **112**, 121101 (2018).
15. P. Chen, S. J. Ge, L. L. Ma, W. Hu, V. Chigrinov, and Y. Q. Lu, Phys. Rev. Appl. **5**, 044009 (2016).
16. P. Chen, S. J. Ge, W. Duan, B. Y. Wei, G. X. Cui, W. Hu, and Y. Q. Lu, ACS Photonics **4**, 1333 (2017).
17. J. Wang, J.-Y. Yang, I. M. Fazal, N. Ahmed, Y. Yan, H. Huang, Y. Ren, Y. Yue, S. Dolinar, M. Tur, and A. E. Willner, Nat. Photonics **6**, 488 (2012).
18. T. Lei, M. Zhang, Y. R. Li, P. Jia, G. N. Liu, X. G. Xu, Z. H. Li, C. J. Min, J. Lin, C. Y. Yu, H. B. Niu, and X. C. Yuan, Light Sci. Appl. **4**, e257 (2015).
19. L. Stoyanov, G. Maleshkov, M. Zhekova, I. Stefanov, D. N. Neshev, G. G. Paulus, and A. Dreischuh, J. Opt. Soc. Am. B **35**, 402 (2018).
20. R. Barboza, U. Bortolozzo, G. Assanto, E. Vidal-Henriquez, M. G. Clerc, and S. Residori, Phys. Rev. Lett. **111**, 093902 (2013).
21. R. Barboza, U. Bortolozzo, M. G. Clerc, S. Residori, and E. Vidal-Henriquez, Adv. Opt. Photonics **7**, 635 (2015).
22. R. Barboza, U. Bortolozzo, G. Assanto, E. Vidal-Henriquez, M. G. Clerc, and S. Residori, Phys. Rev. Lett. **109**, 143901 (2012).
23. V. Freedericksz and V. Zolina, Trans. Faraday Soc. **29**, 919 (1927).
24. R. Barboza, U. Bortolozzo, S. Residori, M. G. Clerc, and E. Vidal-Henriquez, Philos. Trans. R. Soc. A. **372**, 20140019 (2014).
25. M. C. Cross and P. C. Hohenberg, Rev. Mod. Phys. **65**, 851 (1993).
26. R. Barboza, U. Bortolozzo, M. G. Clerc, J. D. Davila, M. Kowalczyk, S. Residori, and E. Vidal-Henriquez, Phys. Rev. E **93**, 050201 (2016).